Estimation of Systematic Uncertainties for Precise Neutron Lifetime Measurement

中性子寿命測定のための系統誤差の評価

Dep. of Physics, the Univ. of Tokyo

Naoki Nagakura (Yamashita Lab.)

February 3, 2016

Abstract

A free neutron decays into a proton, an electron, and an anti-neutrino through the beta-decay process. The decay lifetime of a neutron (τ_n) is a basic parameter in the weak interaction. For example, τ_n is one of the input parameters for the Big Bang Nucleosynthesis (BBN), which predicts light element synthesis in the early universe. Moreover, τ_n is also used to derive the $V_{\rm ud}$ parameter in the CKM (Cabbibo-Kobayashi-Maskawa) matrix.

There are currently in general two methods to measure τ_n. One is to measure the number of decayed protons using the Penning trap method. The other is to store neutrons in a chamber and count the number of remaining neutrons after certain period of time. However, the measured values of τ_n are significantly different (8.4 s, corresponding to 3.8σ) between the two methods. As a result, predicted values of the BBN, such as light element abundance in the early universe, have large uncertainties originating from this discrepancy, and it threatens the validity of Big Bang Nucleosynthesis. In addition, the discrepancy hinders the precise derivation of $V_{\rm ud}$ using neutrons, which is the most important parameter for the unitary test of the CKM matrix. In order to resolve this problem, we perform an experiment to measure τ_n using a completely new method.

The experiment is carried out at the polarized beam branch of beamline five, Material and Life-science Facilities (MLF), Japan Proton Accelerator Research Complex (J-PARC). We use pulsed neutron beams for the first time in the neutron lifetime experiment, and it is expected to significantly reduce the background caused by a neutron. We developed a Time Projection Chamber (TPC) with little environmental background as a beta-decay detector. Furthermore, the divice called the Spin Flip Chopper (SFC) forms a neutron beam into bunches, the length of which is about half of the TPC length. It enables us to detect beta-decay electrons with a 4π solid angle acceptance and achieve good signal-to-noise ratio.

The data acquisition started at J-PARC in 2014, and we already acquired data giving a statistical uncertainty of O(10) $\rm s$ on τ_n so far. The operation power of MLF will increase from current $500\ \rm kW$ to $1\ \rm MW$ within a few years. At $1\ \rm MW$ operation, it is estimated that about 40 days are required as the measurement period in order to achieve 1 s precision. Thus the statistical uncertainty will no longer be a severe problem in the future. This signifies the importance to reduce the systematic uncertainties in this experiment.

This thesis focuses on the evaluation of two systematic uncertainties in order to measure τ_n to $1\ \rm s$ precision. First, the effect with respect to the background caused by ^{17}O atoms is discussed. The existence of the background in the TPC is also shown. Next, the uncertainty originating from the separation of two signal events (beta-decay and $^3\mathrm{He}(n,\ p)^3\mathrm{H}$) is discussed. A parameter used for the separation is newly proposed to reduce the uncertainty. Since the uncertainty is estimated using

the Monte Carlo simulation, an implementation of several physical processes into the simulation is also described in detail.

Contents

List of Figures

List of Tables

Chapter 1

Introduction

In this chapter, we explain the research background and purpose of the experiment on the neutron lifetime.

1.1 Motivation

It is well known that a free neutron decays into a proton, an electron, and an anti-neutrino through the beta-decay process. The decay lifetime (τ_n), which is 880.3 ± 1.1 s according to the Particle Data Group 2015 [1], is a fundamental physical parameter in the weak interaction. This parameter is important for both the Big Bang Nucleosynthesis and the unitarity test of the Cabibbo Kobayashi Maskawa (CKM) matrix.

1.1.1 Big Bang Nucleosynthesis

The universe began to expand after the Big Bang approximately 1.38×10^{10} years ago, and various types of nuclei were generated. Light elements, such as He and Li, are thought to be generated in the early universe. The Big Bang Nucleosynthesis (BBN) is currently the most reliable theoretical model to predict how the light element abundance evolved during this period. The processes predicted by the BBN is explained below.

After the Big Bang, the temperature of the universe gradually decreased with time. At around $t \sim 10^{-6}$ s, where t represents the elapsed time after the Big Bang, the temperature of the universe was too cool for quarks to remain stable as single particles. Thus they formed bound states with each other, e.g. protons and neutrons. The numbers of protons and neutrons were almost same at that time because the neutrons and protons keep a state of equilibrium by the following processes in Eq.(1.1), (1.2), and (1.3)

$$n + e^+ \longleftrightarrow p + \overline{\nu}_e \ , \tag{1.1}$$

$$n + \nu_e \longleftrightarrow p + e^- \ , \tag{1.2}$$

$$n \longleftrightarrow p + e^- + \overline{\nu}_e \ . \tag{1.3}$$

Around $t \sim 1$ s, the energy of nucleons cooled down and the equilibrium of above processes could not be maintained any more. At this stage, the number of protons (p) and neutrons (n) became fixed (freeze-out) according to the temperature at that time ($T_{\rm fr} \sim 0.7$ MeV) and mass difference ($\Delta m \equiv m_n - m_p = 1.293$ MeV)

$$\frac{n}{p} \sim \exp\left(-\frac{\Delta m}{k_B T_{\rm fr}}\right) \sim \frac{1}{6} \ . \tag{1.4}$$

Immediately after the "freeze-out", the deuterons, each formed from a proton and a neutron, could not keep stable because the energy of a photon exceeded the binding energy of deuterons and therefore the deuterons decomposed. At around $t \sim 100$ s, the light element synthesis began mainly through the following processes (Figure 1.1)

$$\begin{aligned}
p + n &\rightarrow \mathrm{D} + \gamma \ , && (1.5)\\
\mathrm{D} + p &\rightarrow {}^3\mathrm{He} + \gamma \ , && (1.6)\\
\mathrm{D} + \mathrm{D} &\rightarrow {}^3\mathrm{He} + n \ , && (1.7)\\
\mathrm{D} + n &\rightarrow {}^3\mathrm{H} + \gamma \ , && (1.8)\\
\mathrm{D} + \mathrm{D} &\rightarrow {}^3\mathrm{H} + p \ , && (1.9)\\
{}^3\mathrm{He} + n &\rightarrow {}^4\mathrm{He} + \gamma \ , && (1.10)\\
{}^3\mathrm{He} + \mathrm{D} &\rightarrow {}^4\mathrm{He} + p \ , && (1.11)\\
{}^3\mathrm{H} + p &\rightarrow {}^4\mathrm{He} + \gamma \ , && (1.12)\\
{}^3\mathrm{H} + \mathrm{D} &\rightarrow {}^4\mathrm{He} + n \ . && (1.13)
\end{aligned}$$

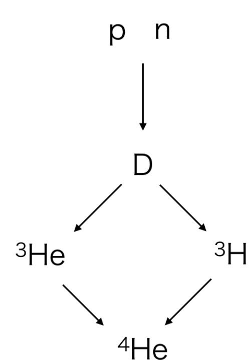

Figure 1.1: Main processes of the light element synthesis.

In order to predict the actual abundance of light elements using the BBN model, the ratio of the number of baryons to photons (η) is needed as an input parameter. Assuming $\eta = (6.23 \pm 0.17) \times 10^{-10}$ measured by Wikinson Microwave Anisotropy Probe (WMAP) [2], the abundance can be predicted as shown in Figure 1.2 [3]. The validity of the BBN model is well proved by the fact that the observed abundance of light elements matches well with the predicted one.

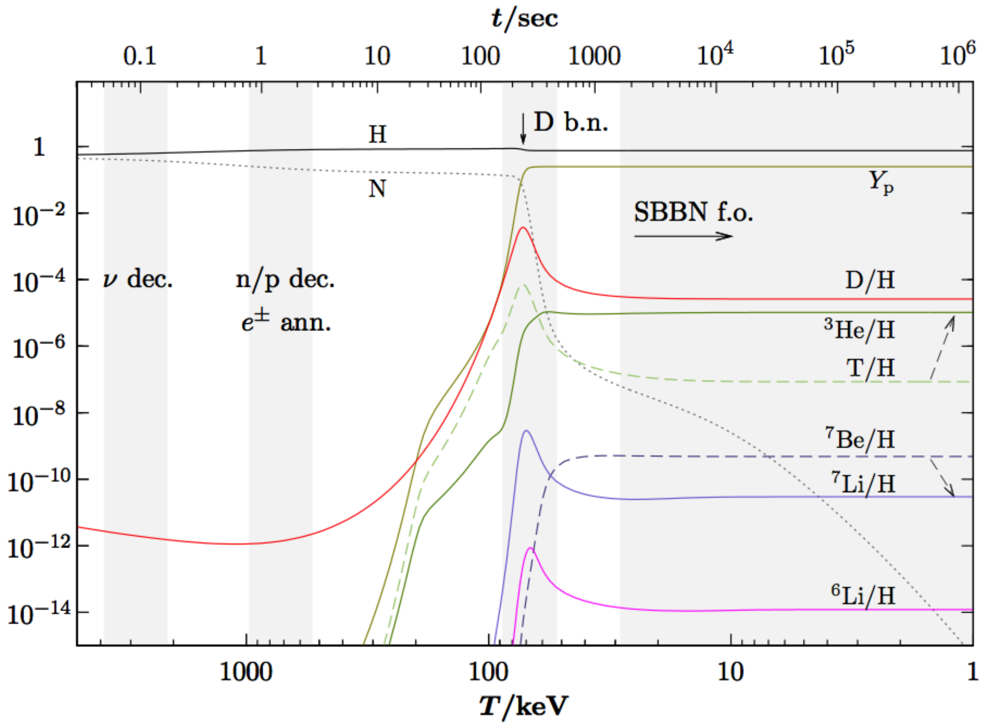

Figure 1.2: Nuclear abundance time evolution by the BBN [3]. The number of neutrons (N) decreases with time because of the beta-decay process.

Until light elements were synthesized, some of the neutrons were converted into protons through the beta-decay process, which reduced the total number of neutrons at the beginning of the nucleosynthesis. Because the number remains invariant during the synthesis, it has a big influence on the following synthetic processes. Assuming the currently known τ_n (~ 880 s [1]), the ratio of the number of neutrons to that of protons (n/p) decreased from $1/6$ to $1/7$ due to beta-decay. Since the ratio directly affects the predicted abundance of light elements, τ_n should be precisely determined.

1.1.2 CKM unitarity

In the Standard Model, the eigenstate of weak interaction is different from that of quark mass. The conversion matrix of the eigenstate is defined as the Cabibbo-Kobayashi-Maskawa (CKM) quark-mixing matrix

$$V_{\rm CKM} = \begin{pmatrix} V_{\rm ud} & V_{\rm us} & V_{\rm ub} \\ V_{\rm cd} & V_{\rm cs} & V_{\rm cb} \\ V_{\rm bd} & V_{\rm bs} & V_{\rm ub} \end{pmatrix} \quad . \tag{1.14}$$

The concrete value of each matrix element is not predicted by the Standard Model. The currently measured values are listed in Eq. (1.15) [1].

$$V_{\rm CKM} = \begin{pmatrix} 0.97427 \pm 0.00014 & 0.22536 \pm 0.00061 & 0.00355 \pm 0.00015 \\ 0.22522 \pm 0.00061 & 0.97343 \pm 0.00015 & 0.0414 \pm 0.0012 \\ 0.00886^{+0.00033}_{-0.00032} & 0.0405^{+0.0011}_{-0.0012} & 0.99914 \pm 0.00005 \end{pmatrix} \quad . \tag{1.15}$$

According to the Standard Model, one of the characteristics of the CKM matrix is that it must be unitary. This constraint comes from the fact that the number of quark generations is exactly three because the unitary constraint collapses if there exits more than three generations. Thus the test of the CKM matrix unitarity is a prove for new physics. There are several constraints which the CKM matrix must satisfy in order to be unitary. The currently most accurate test is carried out using the first generation elements

$$|V_{\rm ud}|^2 + |V_{\rm us}|^2 + |V_{\rm ub}|^2 = 1 \ . \tag{1.16}$$

Substituting the measured values (Eq. (1.15)) into Eq. (1.16), the current constraint at the first generation is confirmed within uncertainties as

$$|V_{\rm ud}|^2 + |V_{\rm us}|^2 + |V_{\rm ub}|^2 = 0.9999 \pm 0.0006 \ . \tag{1.17}$$

Since the $V_{\rm ud}$ element is much larger than the others in Eq. (1.16), the current uncertainty of Eq. (1.17) mainly originates from that of $V_{\rm ud}$. Thus it is extremely important to improve the precision of $V_{\rm ud}$ in order to test the CKM unitarity with high precision.

The $V_{\rm ud}$ parameter is currently determined using $0^+ \rightarrow 0^+$ superallowed nuclear beta-decays; the average of the result is $|V_{\rm ud}| = 0.97417 \pm 0.00021$ [4]. Several nuclei were used to evaluate the parameter, and the results are currently consistent within uncertainties [5]. However, the precision is limited because of the uncertainties associated with the nuclear structure. It is unlikely that the uncertainties will be reduced significantly in the future.

On the other hand, for the measurement of the $|V_{\rm ud}|$ parameter, the method using a free neutron is currently attracting an attention. This is because recent improvement of techniques for controlling neutrons. The $|V_{\rm ud}|$ value can be determined using τ_n as [1]

$$|V_{\rm ud}|^2 = \frac{4908.7 \pm 1.9}{\tau_n[{\rm s}](1+3\lambda)} \ , \tag{1.18}$$

where λ is the ratio of axial-vector to vector couplings. This method currently gives a result of $|V_{\rm ud}| = 0.9754 \pm 0.0014$ [4], whose precision is much poorer than the result produced using nuclear beta-decay. This precision is mainly limited by the experimental uncertainties. Since a neutron has much lower theoretical uncertainties than nuclei, it will be a good material to determine the $V_{\rm ud}$ parameter in the future if the experimental precision improves. This signifies the importance to improve the precision of τ_n measurement.

1.2 Previous lifetime experiments

The neutron lifetime was measured mainly by following three different methods, the proton counting method, the neutron counting method, and the electron counting method. The proton method stores the decayed protons in the volume and counts the number of accumulated protons at the detector. The neutron method stores ultra cold neutrons in the chamber and counts the remaining neutrons after a certain period of time. The electron method counts the number of electrons originating from beta-decay. In this section, the overviews and results of these experiments are introduced.

1.2.1 Proton counting method

ILL, NIST, and Sussex University jointly conducted a neutron lifetime measurement using the proton counting method. The experimental setup is shown in Figure 1.3. Here, neutron beams enter the decay volume, and protons originating from beta-decay are stored in the volume using the Penning trap method during the neutron irradiation. As the maximum energy of protons from beta-decay is $751\ \mathrm{eV}$, a voltage of $800\ \mathrm{V}$ was applied to the volume to store all protons. After the neutron irradiation, the protons were guided towards the proton detector and the number of accumulated protons inside the volume was counted all at once. A $^6\mathrm{Li}$ plate was set at the downstream of the decay volume as a neutron flux monitor. When a neutron beam passed through the plate, several neutrons caused a $^6\mathrm{Li}(\mathrm{n},\alpha)^3\mathrm{H}$ process, and the α or the $^3\mathrm{H}$ was detected by the surrounding four detectors. The number of the events was used to derive the total number of neutrons which passed through the decay volume.

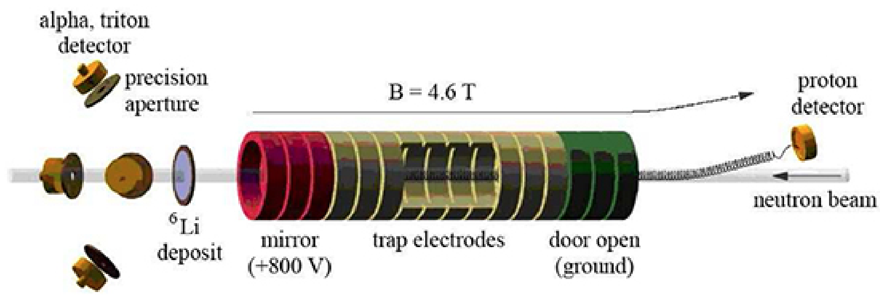

Figure 1.3: The experimental setup of the proton counting method [6].

The number of detected proton events (N_p) represents the number beta-decay events in the decay volume, and it is expressed as

$$N_\mathrm{p} = \varepsilon_\mathrm{p} F \frac{L_\mathrm{decay}}{v\tau_n} \quad , \tag{1.19}$$

where ε_p is the detection efficiency of the proton detector, F is the total number of neutrons which passed the decay volume, L_decay is the length of the decay volume, and v is the neutron velocity. The number of detected $^6\mathrm{Li}(\mathrm{n},\alpha)^3\mathrm{H}$ events (N_n) is expressed as

$$N_n = \varepsilon_n F \rho_\mathrm{Li} \sigma L_\mathrm{Li} \quad , \tag{1.20}$$

where ε_n is the detection efficiency of the $^6\mathrm{Li}(\mathrm{n},\alpha)^3\mathrm{H}$ events, ρ_Li is the $^6\mathrm{Li}$ density, σ is a cross section of $^6\mathrm{Li}(\mathrm{n},\alpha)^3\mathrm{H}$, L_Li is the length of the $^6\mathrm{Li}$ plate. From Eq. (1.19) and (1.20), τ_n is expressed using the ratio of these two kinds of events as

$$\tau_n = \frac{1}{\rho\sigma v} \frac{\left(\dfrac{N_n}{\varepsilon_n}\right)}{\left(\dfrac{N_p}{\varepsilon_p}\right)} \frac{L_\mathrm{decay}}{L_\mathrm{Li}} \quad . \tag{1.21}$$

The most precise result using this method, published in 2013 [7], was $\tau_n = 887.7 \pm 1.2_{\rm stat} \pm 1.9_{\rm syst}$ s. The advantage of this method is the low-background environment for beta-decay. No background caused by the neutron beam is detected in the proton detector because the number of protons is counted all at once after the neutron irradiation. The challenges of this experiment mainly come from the neutron flux because it is difficult to measure the absolute density and thickness of the flux monitor.

1.2.2 Neutron counting method

The neutron counting method stores neutrons in the chamber and counts the number of remaining neutrons after a certain period of time. Ultra Cold Neutrons (UCNs) are used for this type of method. The velocity of a UCN is extremely low ($v \lesssim 10$ m/s) and its de Brogile wavelength is long ($\lambda > 500$ Å) compared to the typical atomic interval (~ 1 Å). These give a UCN the unique property of being totally reflected by several material such as nickel because it feels a uniform potential from the material. Using this property, it is possible to store UCNs in a vacuum chamber.

A group in the St. Petersburg Nuclear Physics Institute (PNPI) used this method to measure τ_n. Figure 1.4 shows the schematic view of the experiment. UCNs are stored in the chamber for a whine whose inner wall was well polished. The number of remaining UCNs in the chamber decreases due to beta-decay. In addition, several UCNs are lost when they interact with the wall of the chamber. The UCN loss process can therefore be divided into two process, beta-decay (τ_n) and wall interaction ($\tau_{\rm wall}$). The remaining UCNs were guided to the UCN detector at which the number of remaining neutrons was counted. τ_n can be evaluated by counting the remaining neutrons after two different storage time (t_1 and t_2) as

$$\tau_n = \left[\frac{\log\left(\frac{N_1}{N_2}\right)}{t_2 - t_1} - \frac{1}{\tau_{\rm wall}} \right]^{-1} , \tag{1.22}$$

where N_i represents the number of remaining neutrons after storage time of t_i.

The most precise result of this experiment was $878.5 \pm 0.7_{\rm stat} \pm 0.3_{\rm syst}$ s [8]. This experiment achieved the most precise measurement in all kinds of experiments so far. The advantage of this method is a small correction for τ_n compared to other methods. The disadvantage is the difficulty in estimating the neutron interactions with the chamber wall accurately.

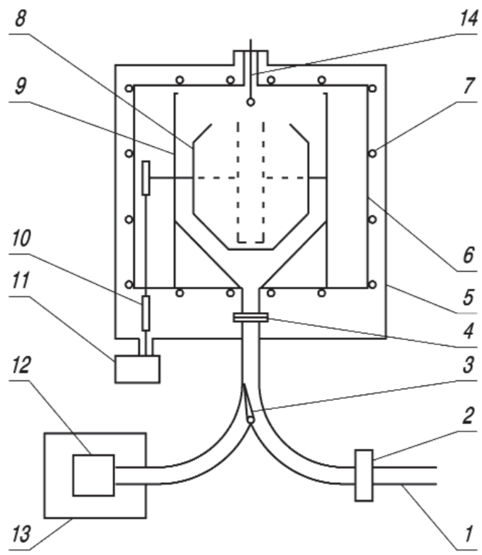

Figure 1.4: The experimental setup of the neutron counting method [8]. 1:neutron guide, 2:UCN inlet valve, 3:flapping valve, 4:connection unit, 5:first vacuum chamber, 6:second vacuum chamber, 7:cooling coil, 8:UCN storage trap, 9:cryostat, 10:rotating mechanics, 11:stepping motor, 12:UCN detector, 13:detector shielding, 14:evaporator.

1.2.3 Electron counting method

A previous measurement using the electron counting method was conducted by R. Kossakowski et al. in 1989 [9]. The measurement used a mixture of $89\ \mathrm{kPa}$ He, $7\ \mathrm{kPa}$ CO_2, and a little $^3\mathrm{He}$ gas in a Time Projection Chamber. Here, the total numbers of the incident neutrons and the beta-decay events are measured by the detector simultaneously. The total number of incident neutrons can be derived by counting the number of $^3\mathrm{He}(n,\ p)^3\mathrm{H}$ events. As for the beta-decay events, the proton energy is too low ($E_p < 751\ \mathrm{eV}$) to be detected in the detector, hence the decayed electrons are detected and used to estimate the number of beta-decay. Assuming that the cross section of $^3\mathrm{He}(n,\ p)^3\mathrm{H}$ is in inverse proportional to the neutron velocity, τ_n is expressed using the number of electron events (N_β) and $^3\mathrm{He}(n,\ p)^3\mathrm{H}$ events ($N_{^3\mathrm{He}}$) as

$$\tau_n = \frac{1}{\rho v_0 \sigma_0} \frac{N_{^3\mathrm{He}}}{N_\beta} \ , \tag{1.23}$$

where ρ is the $^3\mathrm{He}$ density in the Time Projection Chamber, $v_0 = 2200\ \mathrm{m/s}$, and σ_0 is the $^3\mathrm{He}(n,\ p)^3\mathrm{H}$ cross section for a $2200\ \mathrm{m/s}$ neutron. The advantage of this method is that the numbers of both incident neutrons and the beta-decay events can be detected simultaneously in the Time Projection Chamber. Thus several uncertainties related to the detector compensate each other. The difficulty of this experiment is that there is lot of background with respect to beta-decay, such as a prompt γ-ray or radioactivation caused by neutron irradiation.

The schematic setup of the previous experiment by R. Kossakowski is shown in Figure 1.5. The group used a rotating drum as a neutron chopper and a graphite crystal as a monochrometer. The rotating drum, the velocity of which was about 3300 turn/min, was used to form a neutron bunch. The monochrometer was used in order to form the neutron bunch with constant velocity ($837\ \mathrm{m/s}$). These devices give the period in which the neutron bunch is completely inside the Time Projection Chamber. This enabled them a 4π solid angle acceptance for the beta-decay event. Moreover, it also provided little-background environment because no neutrons interacted with the wall of the Time Projection Chamber during this period.

The group accumulated the data for 34 hours and after analysis the result was $878 \pm 27_{\mathrm{stat}} \pm 14_{\mathrm{syst}}\ \mathrm{s}$. Since the uncertainty is much larger than the others, this result is not used for the currently accepted average value of τ_n. There are mainly two reasons for this large uncertainty. The first is the low statistics due to the fact that only neutrons whose velocity was $837\ \mathrm{m/s}$ could be selectively injected to the detector. The neutron transportation efficiency was only 4.4% and the beta-decay event rate in the detector was $0.1\ \mathrm{cps}$. The second reason was the background originating from the radioactivation of the Time Projection Chamber and surrounding devices, whose rate was extremely high ($\sim 80\ \mathrm{cps}$) compared to that of the beta-decay events, which resulted in the bad signal to noise ratio.

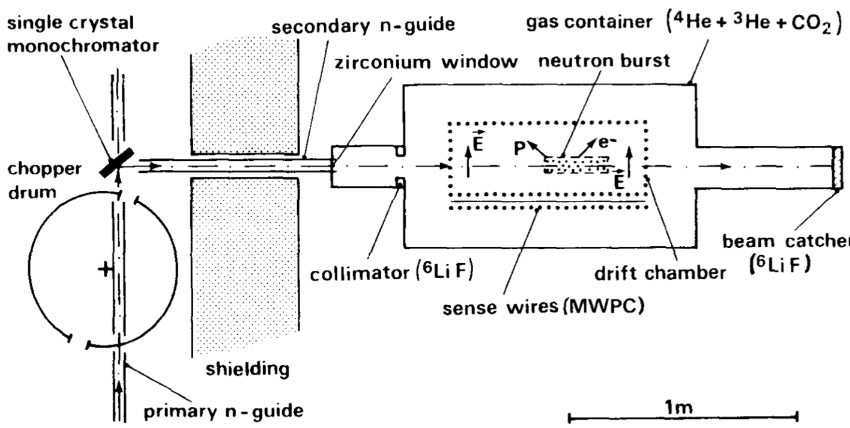

Figure 1.5: The experimental setup of the electron counting method [9].

1.3 Present status of the neutron lifetime

There are roughly three types of methods to measure τ_n as mentioned in Section 1.2. Figure 1.6 shows the result used for calculating the currently accepted average values [1], which do not include the result produced by the electron counting method. The average result produced by the proton counting method is 888.0 ± 2.2 s, whereas that of the neutron counting method is 879.6 ± 0.8 s. There exists a difference of $8.4\ \mathrm{s}$ (or 3.8σ) between the two methods. This difference is a significant problem because τ_n is a crucial parameter for both the BBN model and the element of the CKM matrix (see Section 1.1). Therefore, resolving this problem of the discrepancy is one of the matters requiring immediate attention in particle physics.

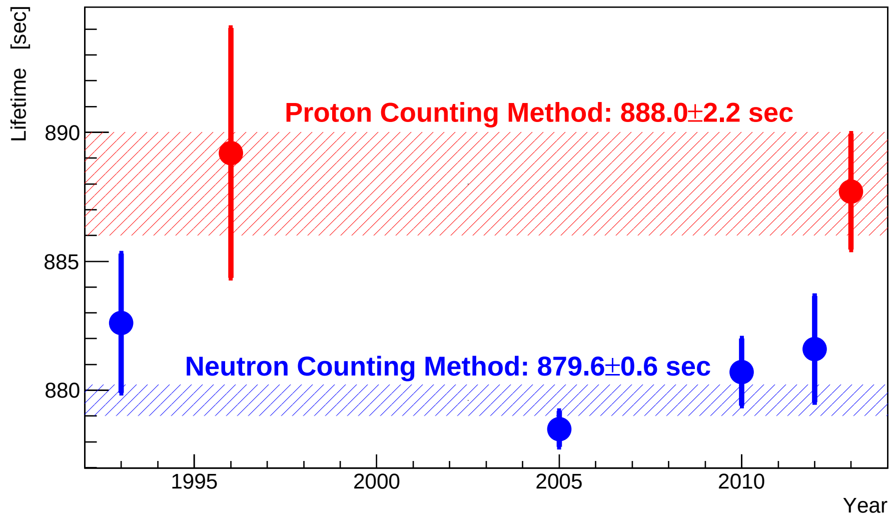

Figure 1.6: Results of the neutron lifetime parameter [1]. The red and blue points represent the result of the proton counting method and the neutron counting method, respectively. There exists a 8.4 s (3.8σ) difference between the two methods.

1.4 The experiment in this thesis

1.4.1 Purpose and characteristics

The purpose of the experiment in this thesis is to measure the neutron lifetime (τ_n) to 1 s precision using the electron counting method (see Section 1.2.3). The previous result produced using this method has an uncertainty of about 30 s as mentioned in Section 1.2.3. We will improve the precision of measurement using several unique devices. The characteristics of this experiment are listed below.

- Pulsed neutrons produced by an accelerator
  In order to improve the statistical uncertainty, we use pulsed neutron beams produced in the accelerator at J-PARC (Japan Proton Accelerator Research Complex). The pulsed neutron beam improves the transportation efficiency of neutrons compared to that of the previous electron counting experiment. Moreover, the energy of every neutron can be derived based on the TOF (Time Of Flight) of the neutron.

- Bunch formation by the Spin Flip Chopper
  We developed the Spin Flip Chopper (SFC) in order to form neutron bunches by controlling neutron polarization. The length of each bunch is adjusted to be about half of the detector length. Therefore, the period during which the bunch is completely inside the detector can be defined. It enables the detection of electrons from beta-decay with a 4π solid angle acceptance. The SFC also contributes to improving the signal-to-noise ratio in the detector.

- Development of the low-background detector
  We developed a low-background Time Projection Chamber as the detector in this experiment. It is made of Poly-Ethel-Ethel-Ketone, which is evaluated to have little environmental background [10]. The detector is surrounded by Pb shield and cosmic ray veto counters, which also contribute to reduces the environmental background.

Our final purpose is to measure τ_n to $1\ \mathrm{s}$ precision. From the view point of statistical uncertainty, it is estimated that about 30 days are required in order to achieve the precision at the MLF design operation power of $1\ \mathrm{MW}$ (see Figure 1.7). Since the statistical uncertainty will not be a severe problem in the future, the reduction of systematic uncertainties is considerably important in this experiment.

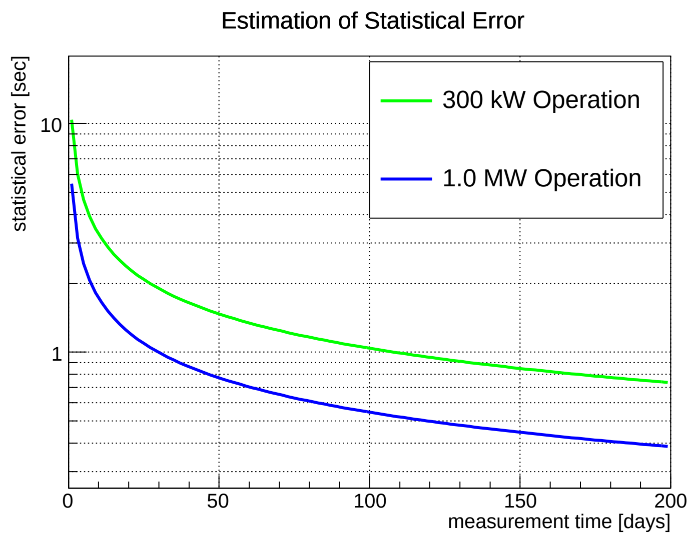

Figure 1.7: Estimated statistical uncertainties for τ_n as a function of the measurement period assuming the accelerator operation power is $300\ \mathrm{kW}$ and $1\ \mathrm{MW}$. About 30 days are required in order to achieve $1\ \mathrm{s}$ precision at the MLF design operation ($1\ \mathrm{MW}$).

1.4.2 Method

The neutron lifetime is the reciprocal of the decay rate for a free neutron. The number of beta-decay events in the detector (N_β) is expressed using τ_n as

$$N_\beta = F\left[1 - \exp\left(-\frac{t}{\tau_n}\right)\right] , \tag{1.24}$$

$$\sim F\frac{t}{\tau_n} , \tag{1.25}$$

where t is the period during which a neutron bunch exits in the detector, and F is the total number of neutrons which passed through the detector. On the other hand, the number of ${}^3\mathrm{He}(n,\ p){}^3\mathrm{H}$

events ($N_{^3\mathrm{He}}$) is given by

$$
\begin{aligned}
N_{^3\mathrm{He}} &= F\left[1-\exp(-\rho\sigma v t)\right] \ , \qquad (1.26)\\
&\sim F\rho\sigma v t \ , \qquad (1.27)
\end{aligned}
$$

where ρ is the $^3\mathrm{He}$ density in the detector, σ is the cross section of $^3\mathrm{He}(n,\ p)^3\mathrm{H}$, and v is the neutron velocity. In the end, τ_n is expressed as the ratio of these two kinds of events,

$$
\tau_n = \frac{1}{\rho\sigma v}\frac{\left(\dfrac{N_{^3\mathrm{He}}}{\varepsilon_{^3\mathrm{He}}}\right)}{\left(\dfrac{N_\beta}{\varepsilon_\beta}\right)} \ , \qquad (1.28)
$$

where $\varepsilon_{^3\mathrm{He}}$ and ε_β represent the efficiencies of beta-decay and $^3\mathrm{He}(n,\ p)^3\mathrm{H}$, respectively. Assuming that the cross section for $^3\mathrm{He}(n,\ p)^3\mathrm{H}$ is inversely proportional to the neutron velocity, which is known to be approximately true [11], τ_n can be expressed as

$$
\tau_n = \frac{1}{\rho\sigma_0 v_0}\frac{\left(\dfrac{N_{^3\mathrm{He}}}{\varepsilon_{^3\mathrm{He}}}\right)}{\left(\dfrac{N_\beta}{\varepsilon_\beta}\right)} \ , \qquad (1.29)
$$

where $\sigma_0 = 5333 \pm 7\ \mathrm{barn}$ [12] is the cross section of $^3\mathrm{He}(n,\ p)^3\mathrm{H}$ for a $2200\ \mathrm{m/s}$ neutron and $v_0 = 2200\ \mathrm{m/s}$. The velocity dependence in Eq. (1.28) is canceled out. Since both $N_{^3\mathrm{He}}$ and N_β are required to derive τ_n, the "signal events" refer to both the beta-decay and $^3\mathrm{He}(n,\ p)^3\mathrm{H}$ events in this experiment. ρ is calculated based on the $^3\mathrm{He}$ gas pressure in the TPC.

Chapter 2

Experimental Setup

The experiment in this thesis uses the electron counting method to measure the neutron lifetime as described in Section 1.4. The experiment uses one of the most intense pulsed neutron beams which can be obtained from J-PARC (Japan Proton Accelerator Research Complex). In addition, the Spin Flip Chopper (SFC) and a Time Projection Chamber (TPC) were developed for this experiment. The flow of a neutron beam in the beamline is shown in Figure 2.1. A polarized neutron beam at J-PARC first enters the SFC. In the SFC, the neutron beam is formed into five bunches per pulse, the size of which is about half of the TPC length. The neutron bunches enter the TPC, where both the beta-decay and the $^3\mathrm{He}(n,\ p)^3\mathrm{H}$ events are detected.

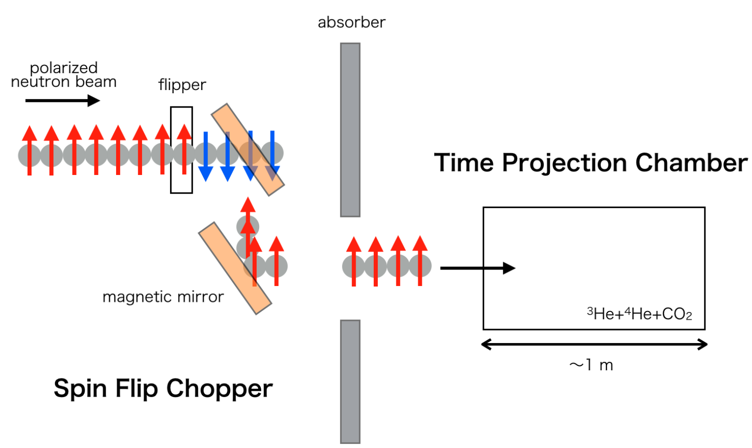

Figure 2.1: Flow of a neutron beam in this experiment.

2.1 Facilities

The experiment is conducted at the polarized beam branch at beamline five (BL05), Material and Lifescience Facilities (MLF), Japan Proton Accelerator Research Complex (J-PARC) in Tokai Village, Ibaraki Prefecture. This section describes these facilities.

2.1.1 J-PARC

Japan Proton Accelerator Research Complex (J-PARC) is the proton accelerators and related complex facilities in Tokai Village, Ibaraki Prefecture. It is managed jointly by Japan Atomic Energy Agency (JAEA) and High Energy Accelerator Research Organization (KEK). The characteristic of J-PARC is that various kinds of secondary beams can be produced, such as neutron, muon, and neutrino beams. A wide range of research, not only for physics but also for biology, chemistry, medical application, and industrial usage is actively conducted at J-PARC.

A bird's-eye view of J-PARC facilities is shown in Figure 2.2. Here, proton accelerators are composed of three parts, Linac, Rapid Cycle Synchrotron, and Main Ring. A proton beam is accelerated up to $400\ \mathrm{MeV}$ in Linac, $3\ \mathrm{GeV}$ in Rapid Cycle Synchrotron, and $30\ \mathrm{GeV}$ in Main Ring. The protons accelerated up to $3\ \mathrm{GeV}$ are used for generating the neutron and muon beams, and the $30\ \mathrm{GeV}$ protons are used for generating the neutrino beam.

Figure 2.2: Bird's-eye view of the J-PARC facilities [13].

2.1.2 MLF

Material and Lifescience Facilities (MLF) is one of the facilities at J-PARC where high intensity pulsed beams of neutrons can be obtained. $3\ \mathrm{GeV}$ protons from Rapid Cycle Synchrotron enter an Hg target at MLF and produce pulsed neutron beams using nuclear spallation reaction. These neutrons are decelerated to about $10\ \mathrm{meV}$ at a moderator surrounding the target in order to make use of the optical properties of a low-energy neutron. The Decelerated neutron beam is transported to 23 neutron beamlines. MLF upgraded operation power from 300 kW to 500 kW in 2015, and they are going to achieve the design power of $1\ \mathrm{MW}$ within a few years.

2.1.3 BL05

Among the 23 neutron beamlines at MLF, beamline five (BL05) is specialized for precise measurements of physical parameters using neutrons. The name is Neutron Optics and fundamental Physics (NOP) beamline. The neutron lifetime measurement in this thesis is conducted at BL05. Various kinds of neutron experiments in addition to the lifetime experiment are performed at this beamline.

Figure 2.3 shows a schematic view of BL05. There are three beam branches at BL05: the non-polarized, polarized, and low-divergence beam branches. The basic parameters of each branch are listed in Table 2.1 [14]. The experiment in this thesis is conducted at the polarized beam branch because we use polarized neutrons to form bunches to be described in Section 2.2.1.

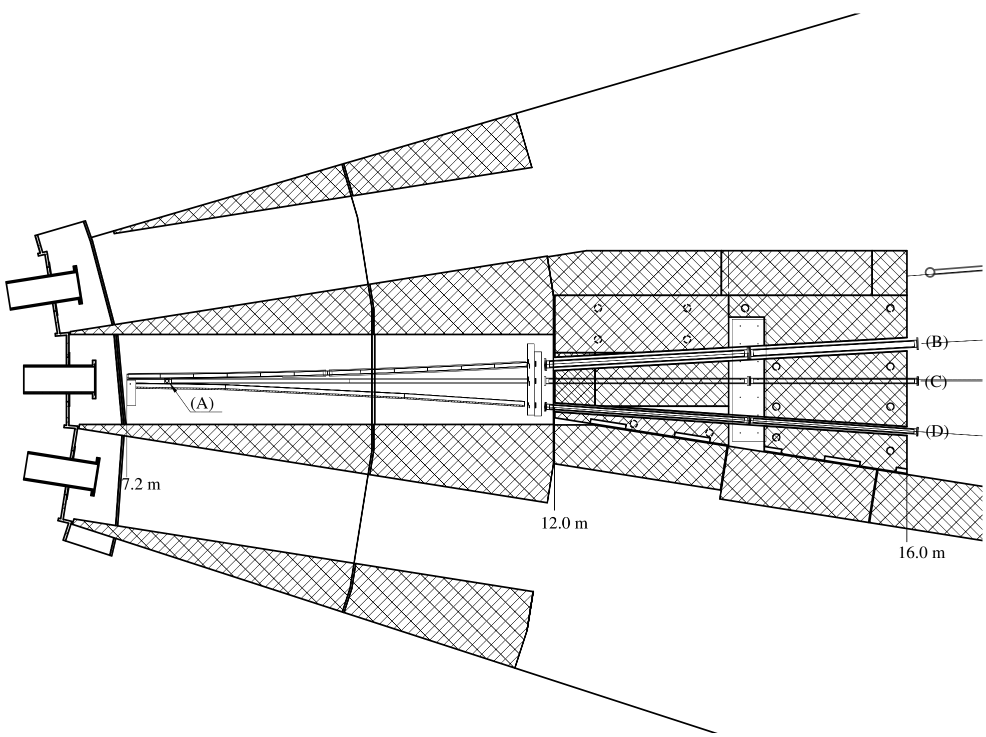

Figure 2.3: Schematic view of the BL05 [10]: (A) upstream of the beam bender, (B) exit of the polarized beam branch, (C) exit of the non-polarized beam branch, (D) exit of the low-divergence beam branch.

Table 2.1: The characteristics of the three beam branches in the BL05 at the design power ($1\ \mathrm{MW}$) [14].

branch	beam size (ver.× hor.[mm])	beam flux $[\mathrm{cm}^{-2}\mathrm{s}^{-1}]$	divergence (ver.×hor.[mrad])	luminance $(\mathrm{cm}^{-2}\mathrm{str}^{-1}\mathrm{s}^{-1})$	polarization ratio
non-polarized	50× 40	$(3.8 \pm 0.3) \times 10^{8}$	m=2	—	—
polariszed	120× 60	$(4.0 \pm 0.3) \times 10^{7}$	23 × 9.4	$(1.8 \pm 0.1) \times 10^{11}$	0.94 - 0.96
low-divergence	80× 40	$(5.4 \pm 0.5) \times 10^{4}$	0.23×0.23	$(1.0 \pm 0.1) \times 10^{12}$	—

2.2 Setup of the experiment at BL05

This section focuses on the specific setup of this experiment at BL05. The schematic view of the overall setup is shown in Figure 2.4.

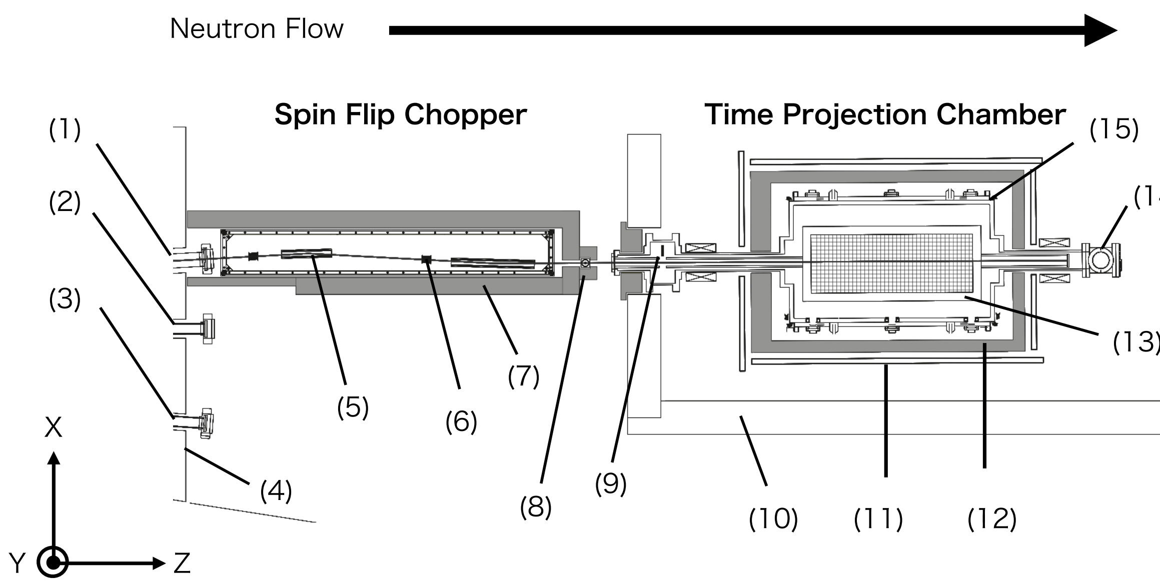

Figure 2.4: Schematic view of the polarized beam branch at BL05 [10]: (1) polarized beam branch, (2) non-polarized beam branch, (3) low-divergence beam branch, (4) Pb shield, (5) magnetic mirror, (6) flipper, (7) Pb shield, (8) flux monitor, (9) LiF shutter, (10) Fe shield, (11) cosmic veto counter, (12) Pb shield, (13) Time Projection Chamber, (14) beam dump, (15) vacuum chamber.

2.2.1 Spin Flip Chopper

We developed an optical device called the Spin Flip Chopper (SFC) for this experiment. It can selectively allow a neutron to penetrate it depending on polarization of the neutron. A continuous neutron beam can therefore be formed into bunches of arbitrary length by the SFC. A schematic view of the SFC is shown in Figure 2.5. It is composed of two polarization flippers and three magnetic mirrors, and the overall structure is surrounded by boron shields. A magnetic field of $1\ \mathrm{mT}$ is applied uniformly in the SFC along the y-axis to maintain the neutron polarization.

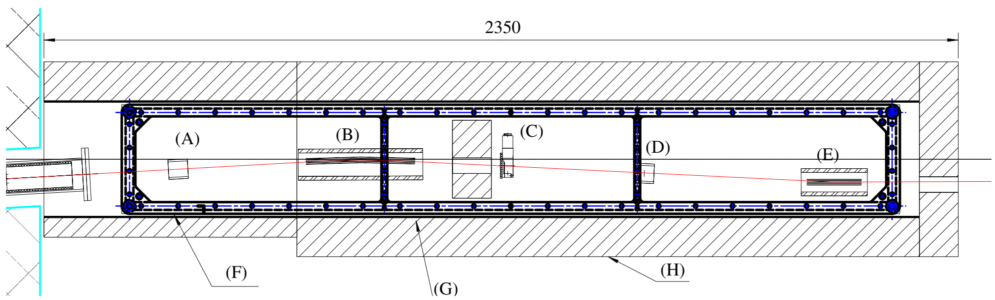

Figure 2.5: Overall structure of the SFC [10]. (A):1st flipper, (B):1st and 2nd mirrors, (C):LiF absorber, (D):2nd flipper, (E):3rd mirror, (F):guide coil (G):B_4C absorber, (H):Pb shield.

The polarization flipper is made of a solenoid coil as shown in Figure 2.6. An alternating current flowing through the coil produces an alternating magnetic field vertically with respect to the polarization direction. The polarization inversion probability for a neutron at the guide magnetic field of B_z and alternating magnetic field of B_y is expressed as

$$P = \frac{B_z^2}{B_z^2 + \left(B_y - \frac{\hbar\omega}{2|\mu_n|}\right)^2} \sin^2\left[\frac{|\mu_n|}{\hbar}\sqrt{B_z^2 + \left(B_y - \frac{\hbar\omega}{2|\mu_n|}\right)^2}\, t\right] \quad , \tag{2.1}$$

where μ_n represents the neutron magnetic moment and ω represents the frequency of alternating magnetic field [15]. Assuming $B_y \gg B_z$, the inversion probability becomes 1 when $B_y = \frac{\hbar\omega}{\mu_n}$ and $B_z t = (n + \frac{1}{2})\pi$. At this resonance condition, the neutron polarization can be reversed by the flipper.

A magnetic mirror has multilayer structure of a ferromagnetic substance (Fe) and a non-ferromagnetic substance ($\mathrm{SiGe_3}$). A photo of the set of magnetic mirrors is shown in Figure 2.7. Since the magnetic field is applied in the mirrors, the potential felt by a neutron in the ferromagnetic substance changes depending on the direction of the polarization. This allows that only the neutron polarized to a certain direction can be reflected by the mirror.

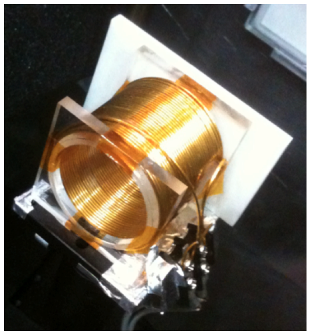

Figure 2.6: Flipper [10].

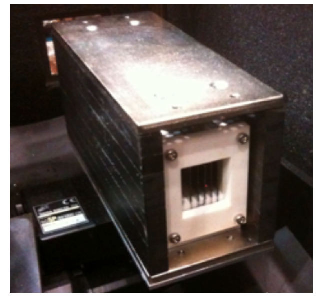

Figure 2.7: Set of magnetic mirrors [10].

If there is no current flowing through the flipper (OFF mode), the incident neutron maintains its polarization and is reflected by the mirrors, which allows it to be transported to downstream. On the other hand, if there is an alternating current flowing through the flipper (ON mode), the neutron polarization is reversed and the neutron is not reflected by the mirror. The neutron penetrates through the mirror, and is absorbed in the absorber in the end. Therefore, we can form the neutron bunches of arbitrary length by adjusting the switching frequency of the two mode. The frequency is adjusted so that the length of every neutron bunch is about the half of the TPC length (5 bunch mode in Figure 2.8).

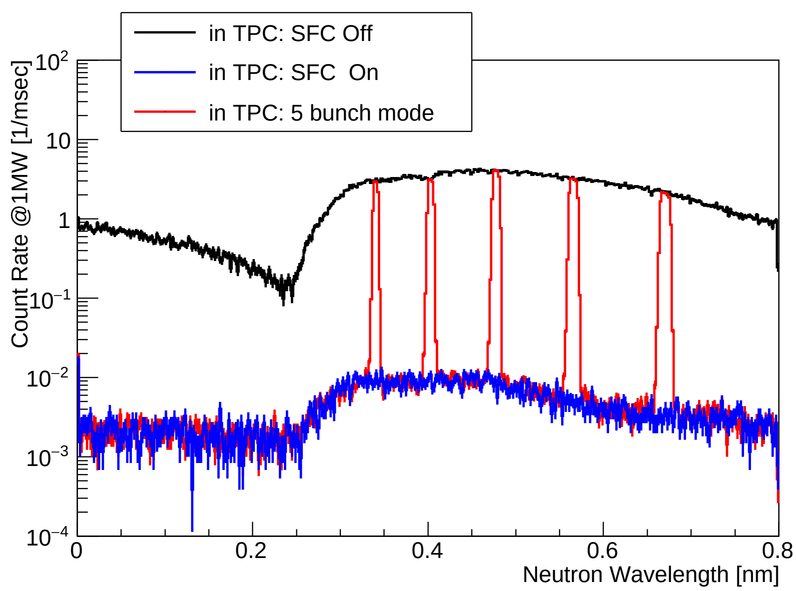

Figure 2.8: Neutron wavelength distribution for several types of SFC operation [14]. The distribution was acquired by a Time Projection Chamber.

2.2.2 Time Projection Chamber

Figure 2.9 shows a photo of the TPC developed for this experiment [16]. It is inside a vacuum chamber, where $^3\mathrm{He}$ $(100\ \mathrm{mPa})$, $^4\mathrm{He}$ $(85\ \mathrm{kPa})$, and CO_2 $(15\ \mathrm{kPa})$ gases are enclosed during the measurement. There is a Multi Wire Proportional Chamber (MWPC) region in the upper part of the TPC. Aluminum sheets are stretched above the MWPC so that the electrons off the electric field of drifting do not accumulate on the TPC wall. There is a cathode copper plate at the bottom of the TPC to which a voltage of $-9000\ \mathrm{V}$ is applied to form an electric field of about $300\ \mathrm{V/cm}$ inside the TPC. The wires to which a negative high voltages is applied are winded around the TPC wall in order to form the uniform electric field in the TPC.

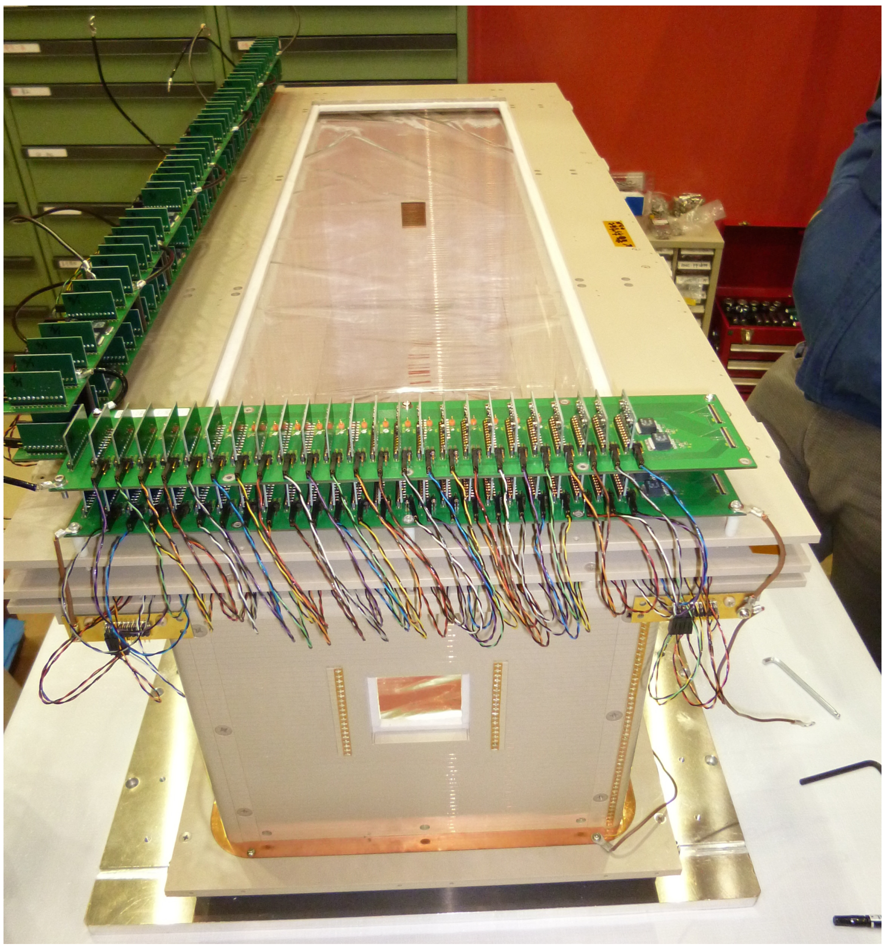

Figure 2.9: Time Projection Chamber in this experiment [16].

When a charged particle passes through the TPC, it ionizes gas molecules and produces electrons. Because an electric field is applied to the sensitive area, the electrons produced from the ionization drift towards the MWPC. The number of electrons increases rapidly around the wire due to avalanche multiplication. The electrons drifted to the wire are detected as a current at each wire. Since the wires of the MWPC are stretched two-dimensionally, the passage of a charged particle can be reconstructed two-dimensionally based on the current at wires. The length of the track perpendicular to the wire plane can be derived by the difference in rise time among the wires. In this way, the passage of the charged particle in the TPC can be reconstructed three-dimensionally.

The MWPC is composed of a multi-layer wire in two dimensions. The geometrical structure of the MWPC is shown in Figure 2.10. There are 24 anode wires, 24 field wires, and 324 cathode wires in the MWPC. A voltage of $1720\ \mathrm{V}$ is applied to the anode wires in order to cause avalanche multiplication, whereas field and cathode wires are grounded. The anode and field wires are arranged alternately in the same plane, whereas the cathode wires are stretched above and below the layer of anode and field wires. The anode and field wires are orthogonal to the cathode wires. Four cathode wires are integrated and read out as one channel. The interval between wires is $6\ \mathrm{mm}$.

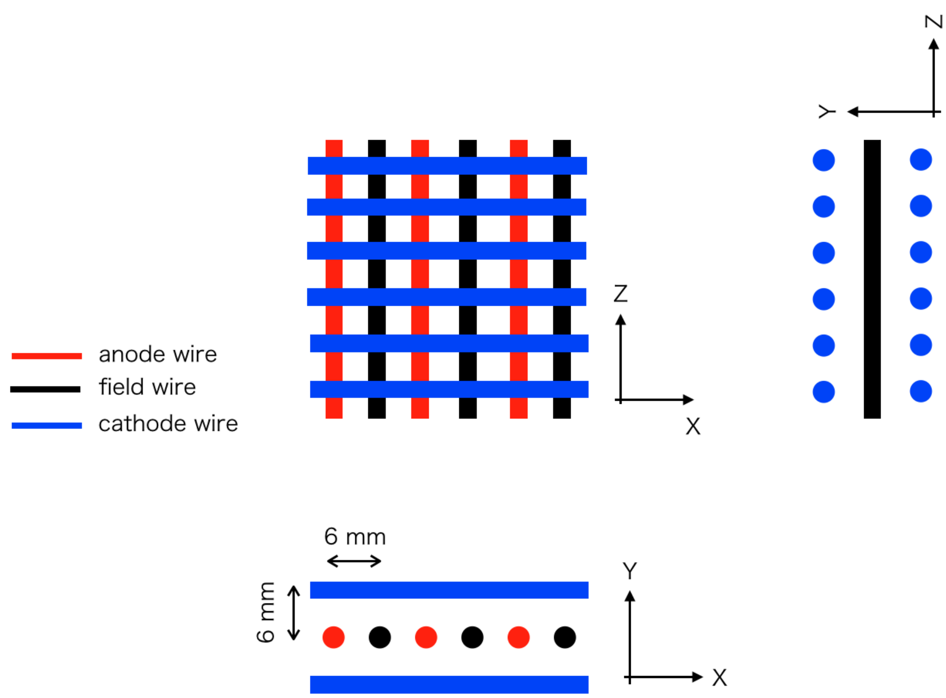

Figure 2.10: Geometrical structure of wires in the TPC.

The TPC developed for this experiment has two unique features [16]. First, the TPC wall is made of Poly Ethel Ethel Ketone, which realizes a low-environmental background because it contains considerably few radioactive substances. Another feature is that the inside wall of the TPC is almost completely covered with a $5\ \mathrm{mm}$ thick plate containing $^{6}\mathrm{LiF}$ in order to absorb scattered neutrons. The plate prevents a scattered neutron from producing γ ray background when it interacts with the wall of the TPC. Although the plate changes the structure of the electric field in the TPC, It is estimated that the distortion of the electric field has a negligible impact on the current analysis.

Table 2.2: Basic parameters of the TPC [16].

size	300 mm $\times$ 300 mm $\times$ 960 mm
anode wire (24 ch)	ϕ20 μm, 1720 V
field wire (24 ch)	ϕ50 μm, 0 V
cathode wire (40 ch$\times$ 2)	ϕ50 μm, 0 V
electric field	300 V/cm (vertical direction)
drift velocity	1.0 μ/s
multiplication factor	5×10^4
basic gas composition	^{4}He (85 kPa), CO_2 (15 kPa), ^{3}He (100 mPa)

The energy resolution of the TPC is evaluated by the absorption event of 5.9 keV ^{55}Fe X-ray. Figure 2.11 shows the energy distribution of the Fe X-ray absorption events. The horizontal axis parameter ASUM (defined in Section 3.1) represents the reconstructed total energy in the anode wires. The left and right distribution is acquired in Fe(up) and Fe(down) mode, respectively. The reconstructed energy of the Fe(down) events decreases due to the large attenuation of the number of drifting electrons. The energy resolution of the TPC (σ/mean) is derived as approximately 10%. Since the $^3\mathrm{He}(n,\ p)^3\mathrm{H}$ process has a large localized deposit energy in the TPC, the multiplication factor for ionized electrons decreases due to the space charge effect. This results in the deterioration of the energy resolution for the $^3\mathrm{He}(n,\ p)^3\mathrm{H}$ events. The quantitative understanding of the effect is to be discussed in Section 5.2.3.

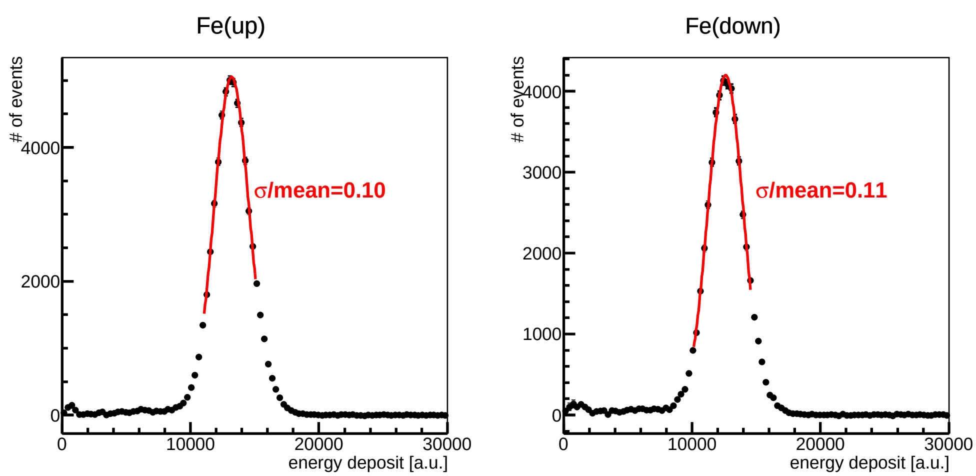

Figure 2.11: Detected Energy for Fe X-ray events in Fe(up) mode (left) and Fe(down) mode (right).

The trigger efficiency of each anode wire is derived using cosmic rays which passed through the TPC. The derived efficiencies for cosmic rays exceed 98% on average as show in Figure 2.12. It is not clear why the wires near the wall have lower efficiencies than the wires at the center.

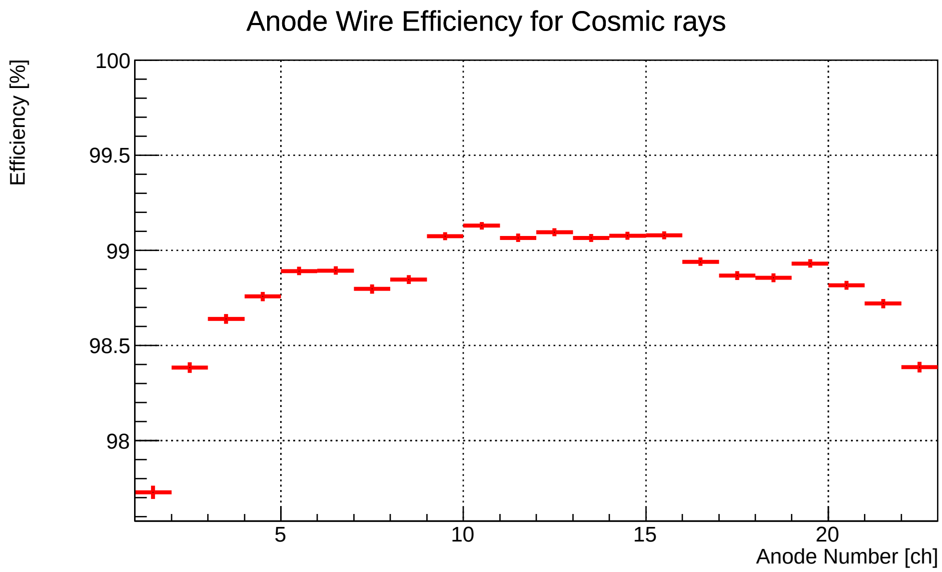

Figure 2.12: Derived efficiency of every anode wire.

2.2.3 Preamplifier

Every wire in the MWPC is connected to a separate charge-sensitive preamplifier in order to amplify the current induced at the wire. Figures 2.13 and 2.14 show a photo and the electric circuit [10] of the preamplifier. The induced current is integrated with 0.5 μs shaping time. We use two kinds of preamplifiers with different gains (high-gain preamplifier and low-gain preamplifier) for this experiment. The difference is the resistivity of R0 and R1. For high-gain preamplifier, R0= ∞ (not connected) and R1=0 Ω, which allows all current to flow towards the operational amplifier. For low-gain preamplifier, R0=300 Ω and R1=1 kΩ, which allows about 1/4 of the total current to flow towards the operational amplifier.

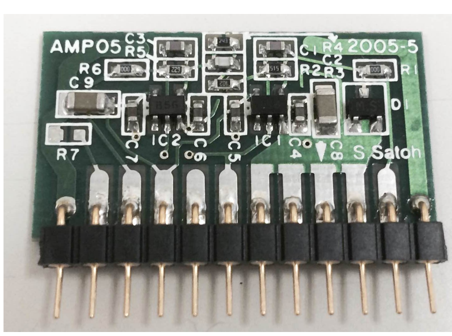

Figure 2.13: Photo of the preamplifier.

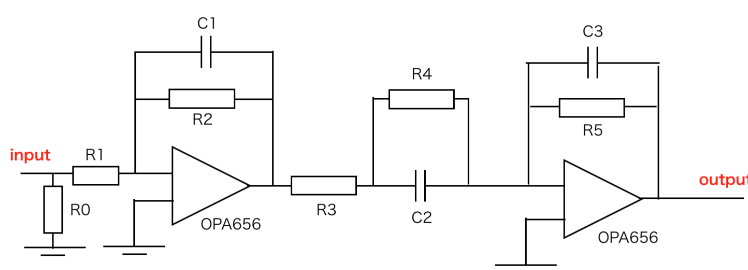

Figure 2.14: Electric circuit of the preamplifier [10]. R0= ∞ (not connected) and R1=0 Ω for a high-gain amplifier, and R0=300 Ω and R1=1 kΩ for a low-gain amplifier

For the gain measurement, a 1 pF capacitor was connected to just upstream of the preamplifier and a rectangular wave from a pulse generator was input to the capacitor. The rectangular wave whose pulse height is $1\ \mathrm{V}$ corresponds to $1\ \mathrm{pC}$ charge flow for the preamplifier. Figure 2.15 shows the input and output waveforms of the preamplifier. By measuring the output pulse height using an oscilloscope, the gain of the preamplifier can be acquired. Table 2.3 represents the measured pulse heights of output waveforms. The parameter V_{pp} represents the pulse height of the input rectangular wave. From these measurements, the gain is evaluated to $1.3\ \mathrm{V/pC}$ for a high-gain preamplifier and $0.23\ \mathrm{V/pC}$ for a low-gain preamplifier.

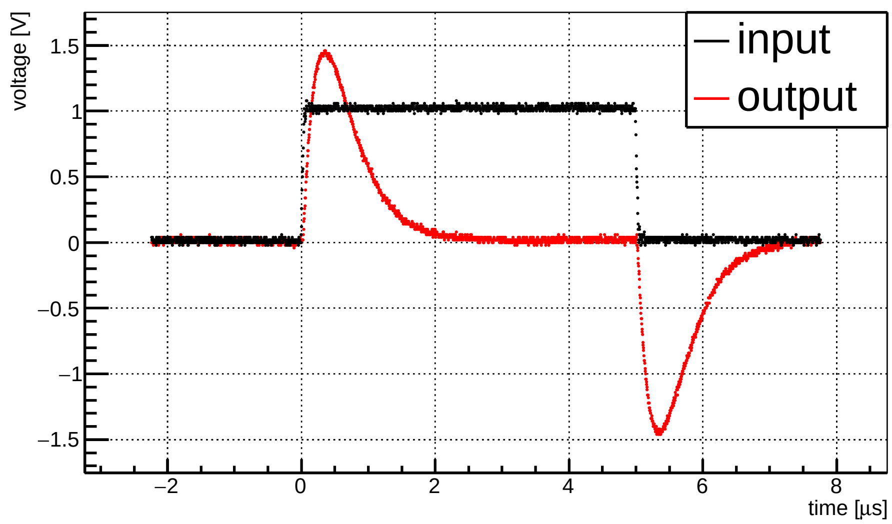

Figure 2.15: Input and output waveforms of the preamplifier. The pulse height of the output waveform was measured.

Table 2.3: Measured pulse heights of output waveform for high-gain and low-gain preamplifiers.

type	number	$V_{pp} = 1.0\ \mathrm{V}$ (Q=1.0 pC)	$V_{pp} = 0.5\ \mathrm{V}$ (Q=0.5 pC)	$V_{pp} = 0.25\ \mathrm{V}$ (Q=0.25 pC)
high gain	1	$1330\ \mathrm{mV}$	$652\ \mathrm{mV}$	$316\ \mathrm{mV}$
	2	$1340\ \mathrm{mV}$	$660\ \mathrm{mV}$	$318\ \mathrm{mV}$
	3	$1360\ \mathrm{mV}$	$672\ \mathrm{mV}$	$328\ \mathrm{mV}$
	average gain	$1.34\ \mathrm{V/pC}$	$1.32\ \mathrm{V/pC}$	$1.28\ \mathrm{V/pC}$
low gain	1	$228\ \mathrm{mV}$	$113\ \mathrm{mV}$	$55.2\ \mathrm{mV}$
	2	$232\ \mathrm{mV}$	$114\ \mathrm{mV}$	$56.8\ \mathrm{mV}$
	3	$228\ \mathrm{mV}$	$110\ \mathrm{mV}$	$57.2\ \mathrm{mV}$
	average gain	$0.23\ \mathrm{V/pC}$	$0.22\ \mathrm{V/pC}$	$0.23\ \mathrm{V/pC}$

2.2.4 Pb shields

Radioactive isotopes such as $^{40}\mathrm{K}$ and $^{208}\mathrm{Tl}$ exist in a rock or an air around us. A γ ray produced from these isotopes causes Compton scattering and produces an electron in the TPC, which is one of the backgrounds for beta-decay. In order to reduce the γ ray flux in the TPC, the vacuum chamber which contains the TPC is surrounded by a Pb shield as shown in Figure 2.16. The Pb shield is 10 cm thick on the front side, and 5 cm thick on the other sides, which are relatively thicker than the attenuation length of 1.6 cm for a γ ray of 1 MeV (see Figure 2.17). The hermeticity of the Pb shield is 99%, and 1% loss is due to the beam path. It is reported that the total γ ray flux decreased to 2% with this shield under operational condition [16].

Figure 2.16: Pb shields surrounding the TPC [10].

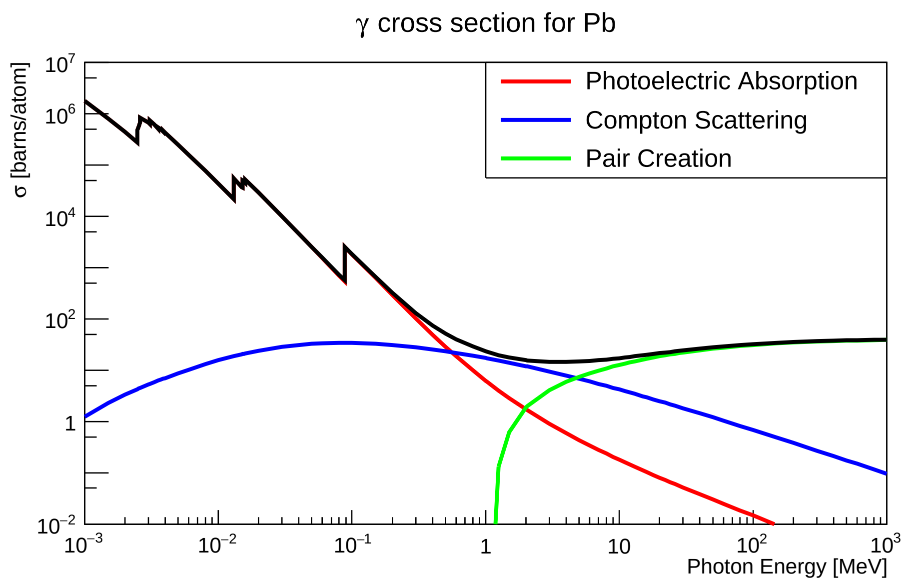

Figure 2.17: γ ray interaction cross section with Pb [17].

2.2.5 Cosmic rays veto counter

A cosmic ray muon which passes through the Pb shield causes ionization process in the TPC. The count rate of cosmic rays in the TPC with Pb shields is evaluated to be as much as 100 cps. Consequently, it is essential to distinguish and remove cosmic ray events. For this purpose, we cover the Pb shields with 14 veto counters as shown in Figure 2.18. Each veto counter is composed of a plastic scintillator and a photomultiplier. There are wavelength shifters in the scintillator in order to transmit the scintillator light efficiently to the photomultiplier. Every side of the TPC wall except the bottom side is covered with two sets of veto counters. If the two sets of veto counters detect an event simultaneously, the trigger for DAQ is forced to be inactivated after 70 μs. The detection efficiency of this setup of veto counters is evaluated to be 96% [16].

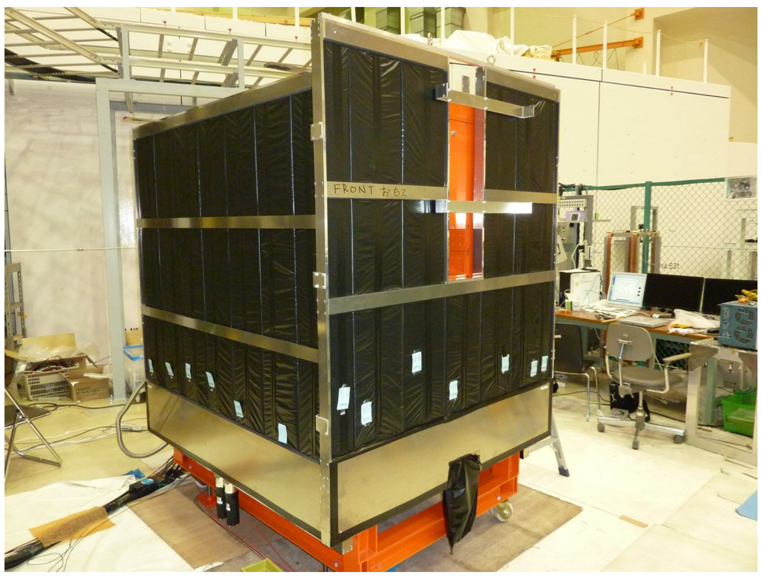

Figure 2.18: Cosmic ray veto counters surrounding the TPC [10].

2.2.6 Flux monitor

There is a neutron flux monitor just upstream of the neutron shutter as shown in Figure 2.4(8). Figure 2.19 shows a photo of the flux monitor. It is a proportional chamber filled with an admixture of He, Ar, and CH_4 gases. The pulse height distribution is always acquired during the measurement, which is used for correcting the flux fluctuation during the measurement (see Section 3.5.3). The window is made of $2\ \mathrm{mm}$ thick aluminum to reduce the scattering probability of neutrons. Its detection efficiency is about 10^{-4} for a $2200\ \mathrm{m/s}$ neutron. Its efficiency fluctuation due to temperature variation is evaluated to be within 0.1% [18].

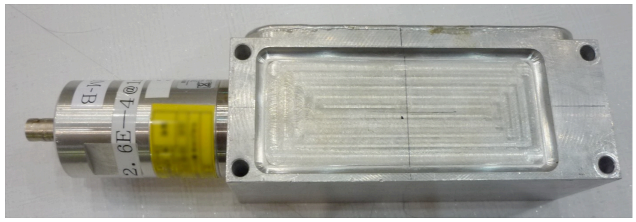

Figure 2.19: Photo of the flux monitor set upstream of the TPC [18].

The typical pulse height distribution of the flux monitor is shown in Figure 2.20. The lowest energy peak seems to come from the $^3\mathrm{He}(n,\ p)^3\mathrm{H}$ events. Several high-energy peaks originate from the absorption events of ^{10}B, which is expected to be adhered to the inner wall of the flux monitor. The number of events whose pulse height exceed 66.4% of the lowest peak is used for the analysis to be described in Section 3.5.3.

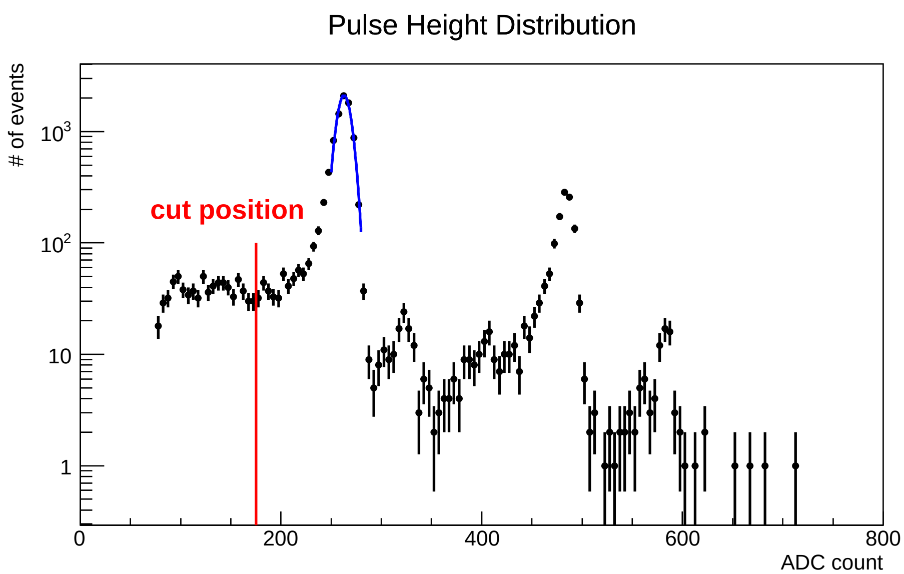

Figure 2.20: Pulse height distribution acquired the flux monitor. The cut position for the $^3\mathrm{He}(n,\ p)^3\mathrm{H}$ process is determined as the 66.4% of the first peak position.

2.2.7 Thermometer

The temperature variation in the TPC is monitored continuously by eight thermometers during the measurement. Each of them is a platinum temperature measuring resistor (Pt100), which measures the resistivity of the platinum using a four-terminal method. The temperature variation during one cycle of gas filling is shown in Figure 2.21. The temperature in the TPC rises with time because the preamplifiers connected to wires produce heat during the TPC operation. Furthermore, the thermometers near the amplifiers (CH6, CH7, and CH8) show higher temperature than the others.

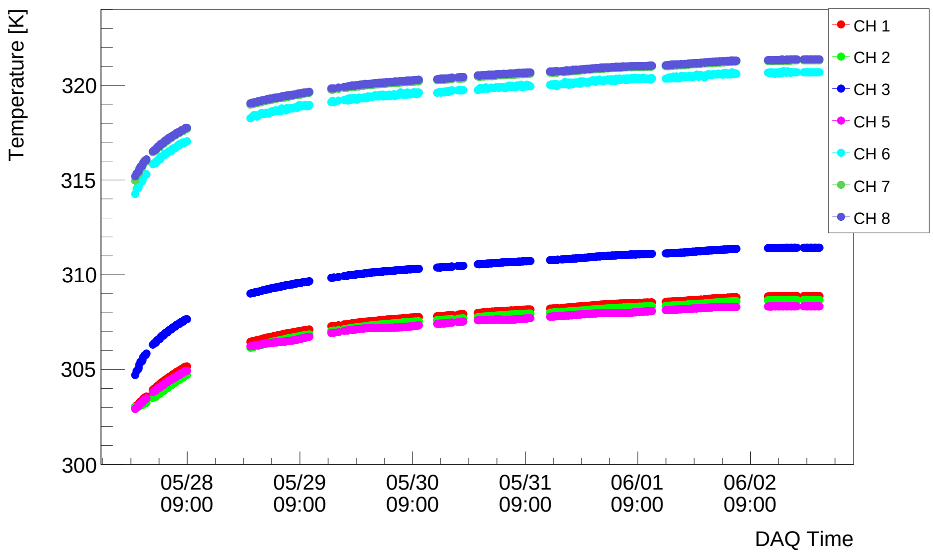

Figure 2.21: Temperature variation during the TPC operation. The temperature increases with time because of the heat produced by preamplifiers.

2.2.8 DAQ electrical circuit

Figure 2.22 shows the electrical circuit used in this experiment. If any pulse height of anode wires exceeds a threshold level (~ 15 mV), a trigger signal is sent to a DAQ system and the voltage of all wires are digitized in every 100 ns for 100 μs. The trigger timing is adjusted to be 30 μs in the acquisition time as shown in Figure 2.23. A signal detected by the veto counters veto the trigger for about 70 μs. On the other hand, the signal become a DAQ trigger in the cosmic ray mode (see Section 3.3). We use a COmmon Pipelined Platform for Electronics Readout (COPPER) system for DAQ, which was developed at KEK [19]. We use four COPPER boards in this experiment, and on every board are mounted four daughter cards called Front-end INstrumentation Entities for Sub-detector Specific electronics (FINESS). The pulse height of all wires and the timing of DAQ trigger are digitized and recorded by Flash ADC and TDC, respectively. The full scale of the ADC is 4000 ch, corresponding to a voltage of 2 V. Besides waveforms, the temperature, the pressure, the high voltages applied to the electrodes, and pulse heights of veto counters are also recorded during the measurement.

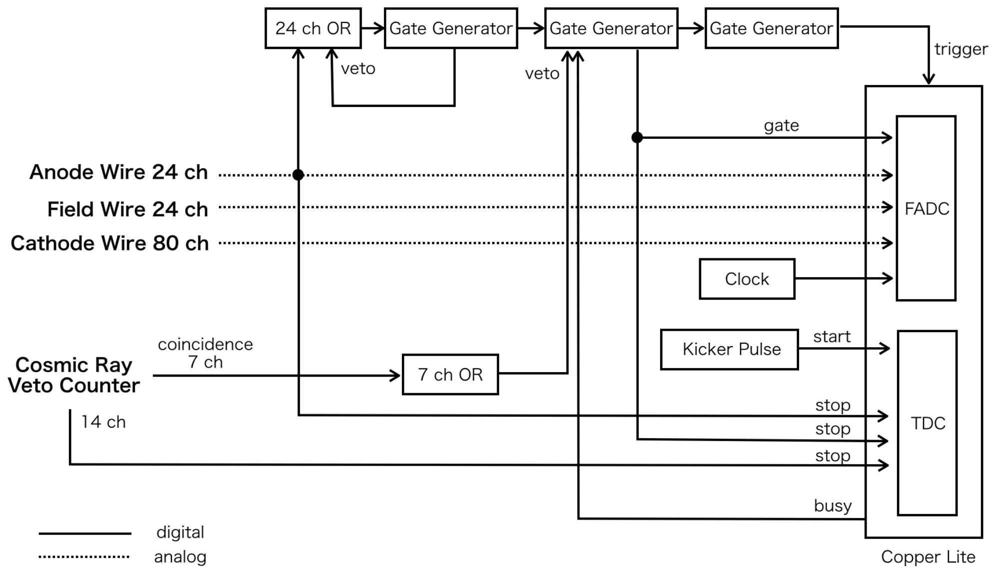

Figure 2.22: A DAQ electric circuit [16].

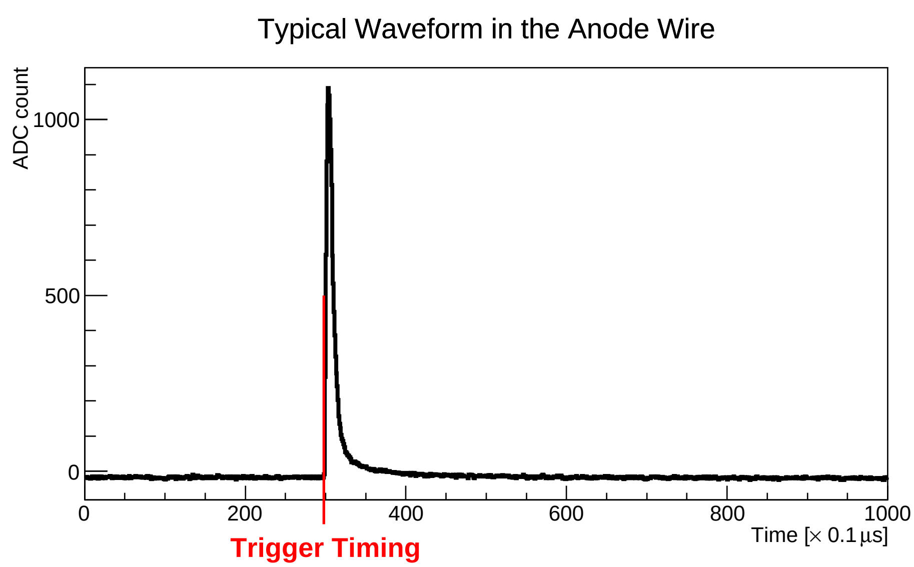

Figure 2.23: Typical waveform of the anode wire. The trigger timing is adjusted to be 30 μs.

2.2.9 System for gas mixture

The ^{3}He, ^{4}He, and CO_2 gases are enclosed in a vacuum chamber during the measurement. We introduce the gas into the chamber using a system as shown in Figure 2.24. Cylinders for the ^{4}He and CO_2 gases are connected to the V1 and V2 bulbs respectively, whereas the ^{3}He gas is stored in the I6 container. Regarding the ^{4}He and CO_2 gases, we adjust the pressure in the TPC based on the reading of a pressure gauge, Mensor CPG2500. In contrast, the ^{3}He gas introduced to the TPC is only $\sim 100\,\mathrm{mPa}$, which is too low to be measured directly in the pressure gauge. Thus the $^{3}\mathrm{He}$ gas pressure in the TPC is determined using a volume expansion method. In this method, the pressure of the $^{3}\mathrm{He}$ gas before expanding to the TPC (the $^{3}\mathrm{He}$ gas is stored in the Im region in Figure 2.24) is measured with high precision because the pressure is comparatively high. The $^{3}\mathrm{He}$ gas pressure expanded to the TPC can be derived using the Boyle-Charle's law.

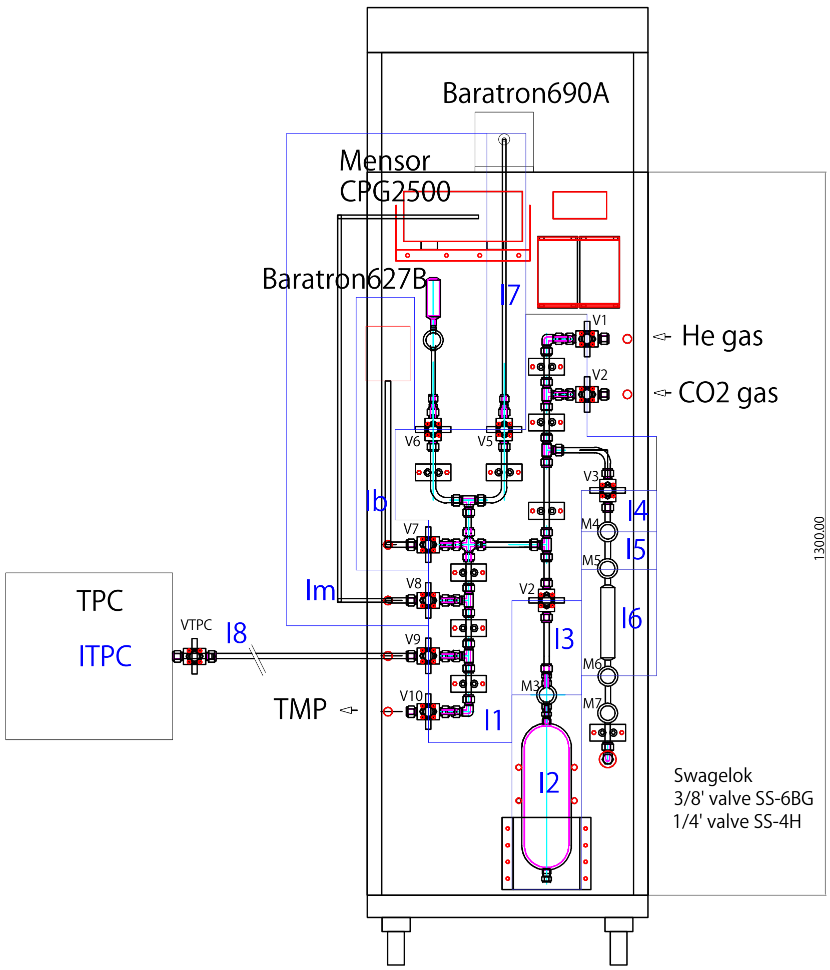

Figure 2.24: System for Gas Mixture.

Chapter 3

Introduction of Analysis

In this chapter, the basic parameters, the data selection methods, acquired data set for analysis, expected background, and calibration methods are described.

3.1 Parameter definition

3.1.1 Parameters for the acquired waveform

When any pulse height of anode wires exceeds the discriminator threshold, waveforms of all wires are recorded for 100 μs. The parameters defined for the waveforms are shown in Table 3.1 and Figure 3.1.

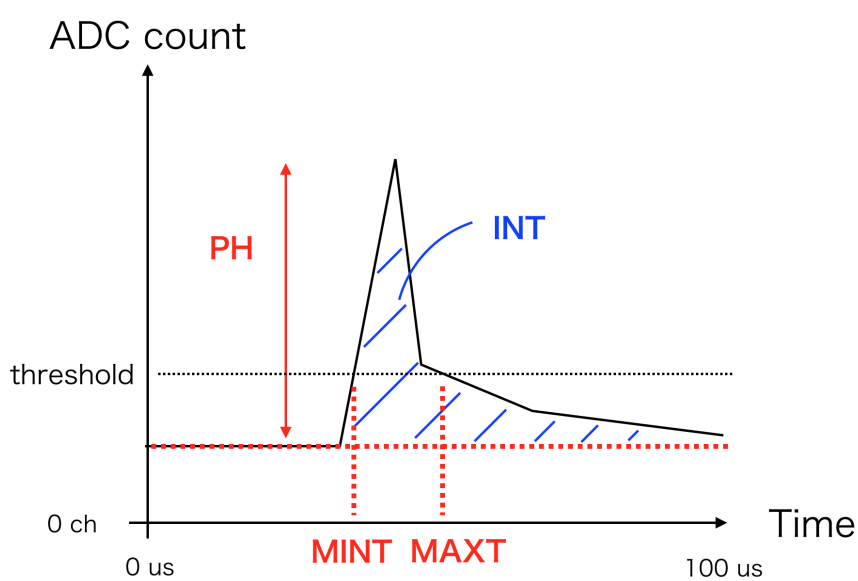

Figure 3.1: Parameters definition for the waveform.

Table 3.1: Parameters definition for the waveform.

parameter	original name	definition
PH	pulse height	the difference of a maximum ADC count and a pedestal value for the waveform
INT	integral	waveform integral based on the pedestal position
MINT	minimum time	a minimum time at which the waveform exceeds a threshold ($\sim$ 30 ch above the pedestal)
MAXT	maximum time	a maximum time at which the waveform exceeds a threshold ($\sim$ 30 ch above the pedestal)
HIT	hit	hit bit judgment parameter. 1 is assigned if PH-PED $\geq$ 30 ch

There are four kinds of wires in this experiment as mentioned in Section 2.2.2; there are anode wires (A), field wires (F), high-gain cathode wires (CH), and low-gain cathode wires (CL). The wire name and wire number are attached to each parameter as a prefix and suffix, respectively. For example, the PH value for the third anode wire is denoted as APH[2]. Note that the wire number starts at 0. The PH and INT parameters are calibrated based on the Fe X-ray data as described in Section 3.6).

3.1.2 Event parameters

Based on the above definitions, the following parameters are defined for every event.

$$
\begin{aligned}
\mathrm{PH\_MAX} &= \mathrm{Max}\{\mathrm{PH}[i]\}, \\
\mathrm{SUM} &= \sum_{\mathrm{HIT}[i]=1} \mathrm{INT}[i], \\
\mathrm{NUM} &= \sum_{\mathrm{HIT}[i]=1} 1, \\
\mathrm{DTIME} &= \mathrm{Max}\{\mathrm{MINT}[i]\} - \mathrm{Min}\{\mathrm{MINT}[i]\}, \\
\mathrm{CE} &= \frac{\sum_{\mathrm{HIT}[i]=1} \mathrm{INT}[i] \times i}{\sum_{\mathrm{HIT}[i]=1} \mathrm{INT}[i]}, \\
\mathrm{MINPOS} &= \mathrm{Min}\{i|\mathrm{HIT}[i] = 1\}, \\
\mathrm{MAXPOS} &= \mathrm{Max}\{i|\mathrm{HIT}[i] = 1\}. \\
\mathrm{DC} &= \mathrm{Min}\{|\mathrm{MINPOS} - 12|, |\mathrm{MAXPOS} - 12|\}(definedonlyforanodewires), \\
\mathrm{RANGE} &= \sqrt{(\mathrm{ANUM} \times \mathrm{APITCH})^2 + (\mathrm{CHNUM} \times \mathrm{CPITCH})^2 + (\mathrm{ADTIME} \times v_{\mathrm{drift}})}.
\end{aligned}
$$

The parameters APITCH (=12 mm) and CPITCH (=24 mm) represent the intervals of anode and cathode wires, respectively. The parameter v_{drift} (~ 1 cm/μs) is the drift velocity for an ionized electron in the TPC (see Section 3.6.2). Qualitative definitions of these parameters for a event are shown in Table 3.2 and Figure 3.2.

Table 3.2: Qualitative definitions of the parameters for a event used in the analysis.

parameter	original name	
PH_MAX	pulse height maximum	qualitative index representing how localized the ionization process is
SUM	summation of the deposit energy	total energy deposit in the TPC
NUM	number of wires	total number of wires whose pulse heights exceed the threshold
DTIME	difference of drifting time	maximum difference of the rising time among all wires
CE	energy weighted center position	weighted average of the position based on the energy deposit
MINPOS	minimum position	minimum number of wires whose pulse heights exceed the threshold
MAXPOS	maximum position	maximum number of wires whose pulse heights exceed the threshold
DC	distance from the center	distance between the endpoints of the track and the center of the TPC
RANGE	range	three-dimensional length of the track

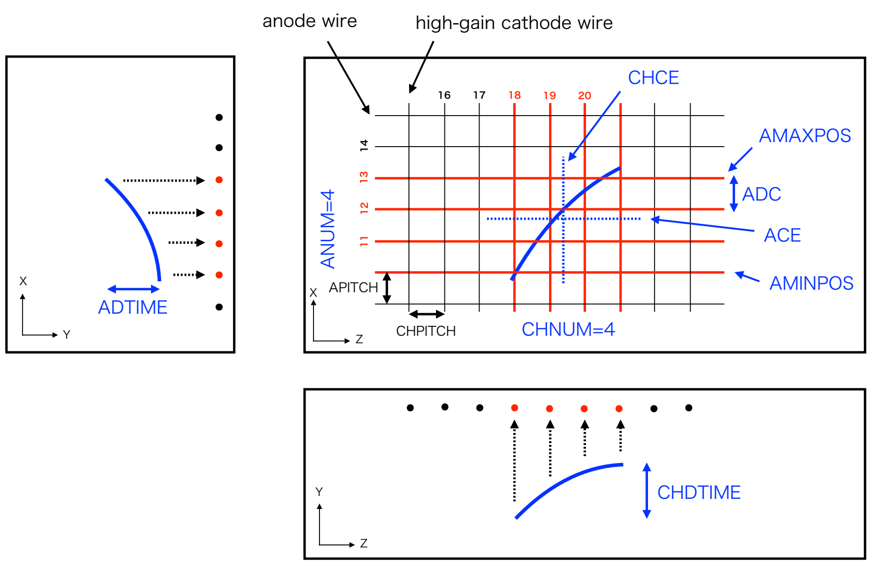

Figure 3.2: Qualitative definitions of the parameters for a event used in the analysis.

3.2 Fiducial and sideband time

In this experiment, a neutron bunch, whose length is about half of the TPC length, is formed by the Spin Flip Chopper (SFC) as mentioned in Section 2.2.1. The position of the neutron bunch can be estimated using the position of $^3\mathrm{He}(n,\ p)^3\mathrm{H}$ events in the TPC. Figure 3.3 shows the position and Time Of Flight (TOF) distribution of $^3\mathrm{He}(n,\ p)^3\mathrm{H}$ events in the TPC. The z-axis origin corresponds to the center of the TPC, and the region of $-48\ \mathrm{cm} < z < 48\ \mathrm{cm}$ corresponds to the TPC region. We can see five bunches made by the SFC move towards the z-axis positive direction.

3.2.1 Fiducial time

As every neutron in a bunch has almost the same velocity, the bunch maintains its size during the flight. We set -40 cm $< z <$ 40 cm as the effective region in the TPC. We can define the time during which a neutron bunch is completely inside the region. This time is called a "fiducial time" in this thesis. The number of neutron events is counted only in the fiducial time. The method to decide the fiducial time is explicitly shown in Figure 3.4. The starting time corresponds to the time that the bunch tail reaches $z = -40$ cm. Similarly, the completion time corresponds to the time that the bunch head reaches $z = +40$ cm. The overall fiducial time is determined as the sum of the following five regions.

$$17.22 \text{ ms} \leq \text{TOF} \leq 17.48 \text{ ms} \tag{3.1}$$
$$20.39 \text{ ms} \leq \text{TOF} \leq 20.69 \text{ ms} \tag{3.2}$$
$$24.16 \text{ ms} \leq \text{TOF} \leq 24.52 \text{ ms} \tag{3.3}$$
$$28.63 \text{ ms} \leq \text{TOF} \leq 29.05 \text{ ms} \tag{3.4}$$
$$33.91 \text{ ms} \leq \text{TOF} \leq 34.41 \text{ ms} \tag{3.5}$$

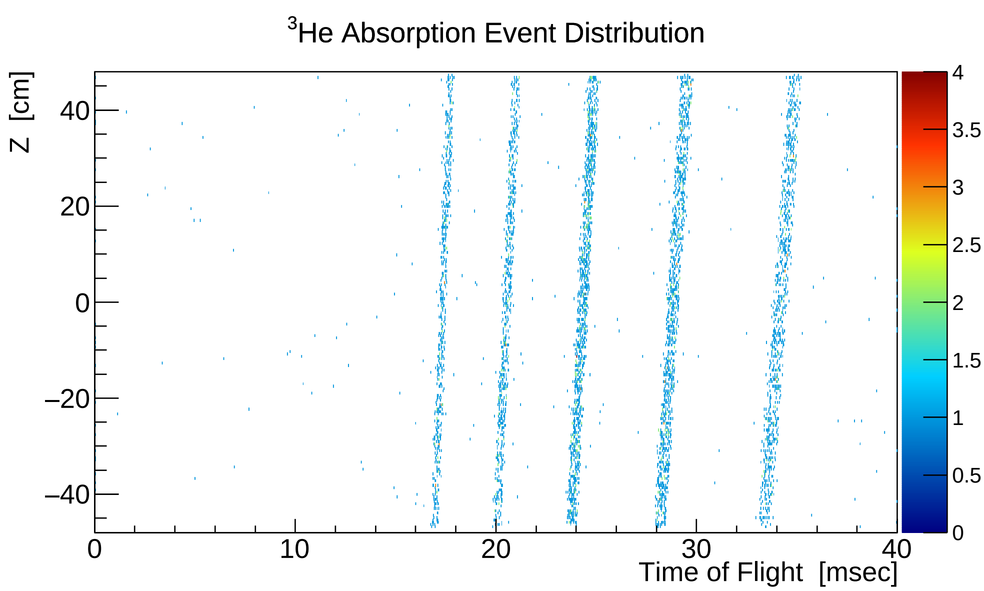

Figure 3.3: Correlation between TOF and z position in the TPC for the $^3\text{He}(n,\ p)^3\text{H}$ events.

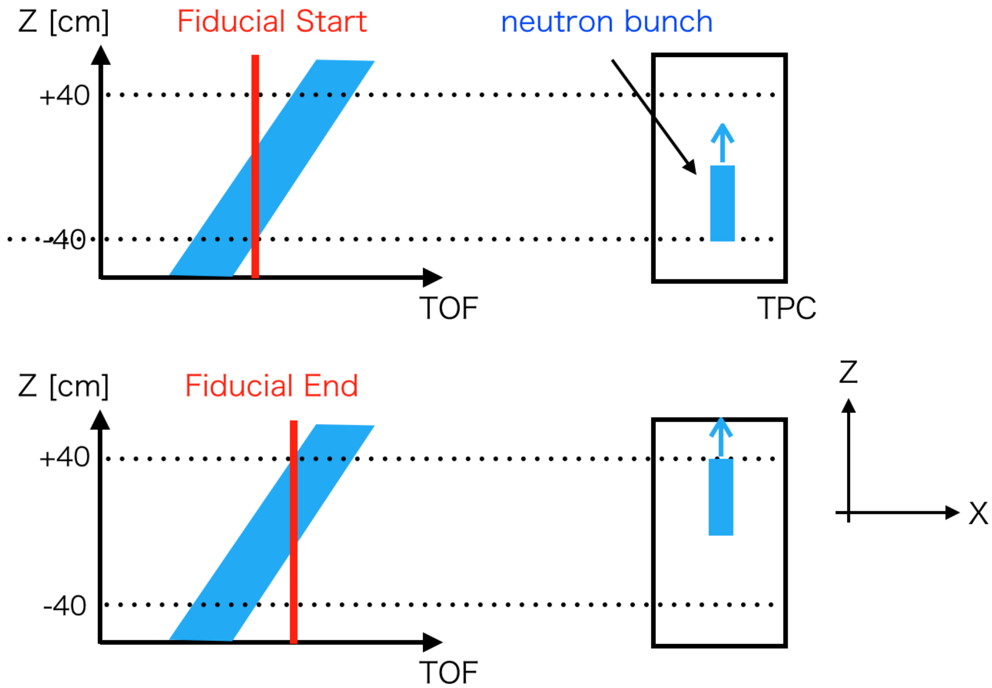

Figure 3.4: Definition of the fiducial time. A neutron bunch is completely inside the region of -40 cm $\leq z \leq 40$ cm during the fiducial time.

3.2.2 Sideband time

In order to estimate the background, it is necessary to analyze the data where no neutron event exists. It is called a "sideband time" in this thesis. This time is defined as $4\ \mathrm{ms} \leq \mathrm{TOF} \leq 10\ \mathrm{ms}$, during which no neutron bunch exists in the TPC as shown in Figure 3.3. A TOF 4 ms region is excluded from the sideband time because a lot of background events associated with the nuclear spallation are estimated to exist in the TPC at around TOF=0 ms.

3.3 Data set for analysis

3.3.1 Data cycle

We acquired several sets of data for calibration and the background analysis. Table 3.3 gives a data cycle used for the analysis in this experiment. It takes about one hour to take a cycle of data. The low gain mode is not included in the data cycle, and several sets of the data are acquired every one or two days.

Table 3.3: Data cycle acquired by the TPC.

mode	shutter status	time [s]	purpose
passing	open	1000	count the number of N_β and $N_{^3\mathrm{He}}$ events
dumping	close	1000	for background measurement
Fe(up)	close	300	for energy calibration
Fe(down)	close	300	same above
cosmic ray	close	100	for the calibration of drift velocity
low gain	open	1000	derive the nitrogen pressure as an outgassing

- passing mode and dumping mode
  In the passing mode, a neutron bunch made by the SFC enters the TPC and both the beta-decay and $^3\mathrm{He}(n,\ p)^3\mathrm{H}$ events are detected in the TPC. In the dumping mode, the neutron bunch is absorbed in the neutron shutter which is set at just upstream of the TPC (Figure 2.4 (9)). The number of several background events can be estimated by the data in the dumping mode (see Section 3.5).

- Fe mode
  A ^{55}Fe source is attached to the side of the TPC. $^{55}\mathrm{Fe}$ undergoes beta-decay and produces ^{55}Mn with a half life of 2.7 years. The ^{55}Mn nucleus sometimes absorbs an electron and produces an X-ray of $5.9\ \mathrm{keV}$ or $6.4\ \mathrm{keV}$ at the same time. Electrons produced by photoabsorption process of the X-ray are detected in the TPC, and the event is used for energy calibration of the TPC. Since the electron produced by photoabsorption process has an extremely short track ($\sim\ 2\ \mathrm{mm}$), it can be regarded as a point-like event. The Fe source is connected to a rotation stage, and it can be set at $75\ \mathrm{mm}$ (Fe(up) mode) and $225\ \mathrm{mm}$ (Fe(down) mode) below the MWPC (see Figure 3.5).

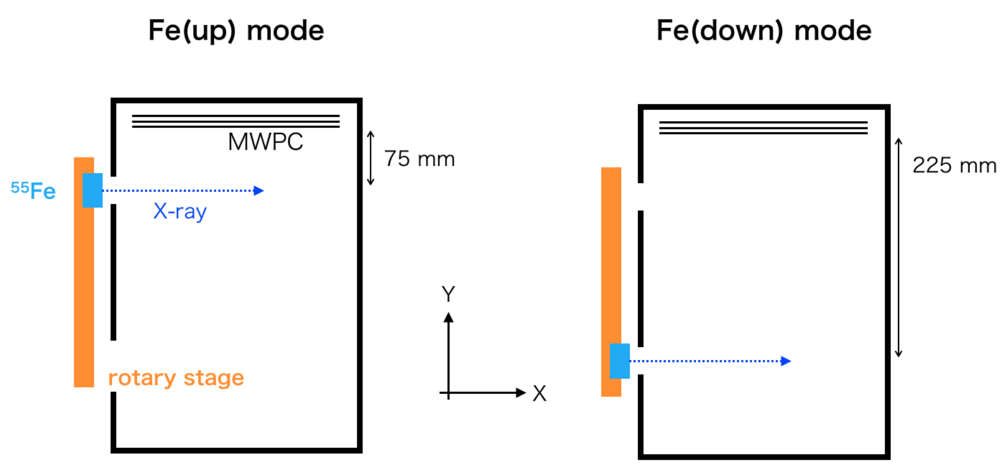

Figure 3.5: Position of the ^{55}Fe X-ray source: $75\ \mathrm{mm}$ drifting for the Fe(up) mode (left), and $225\ \mathrm{mm}$ drifting for the Fe(down) mode (right).

- cosmic ray mode
  The drift velocity in the TPC can be evaluated by the cosmic ray events, and the result is used to calibrate the drift velocity for every gas (see Section 3.6.2). The DAQ trigger in the cosmic ray mode requires the event detection in both the TPC and the surrounding veto counters. The event rate of cosmic ray events is approximately $60\ \mathrm{cps}$ in the TPC.

3.3.2 Analysed data in this thesis

The introduced gas in the TPC needs to be replaced about once a weak because the number of the $^{14}\mathrm{N}(n,\ p)^{14}\mathrm{C}$ events increases with time due to the outgassing of the nitrogen gas. The gas condition is managed by the number assigned for every gas filling. Table 3.4 defines the gas composition used for the analysis in this thesis.

Table 3.4: Gas compositions used for analysis in this thesis.

gas number	gas condition	period	^{3}He pres.	^{4}He pres.	CO_2 pres.
42	basic	2014/5/27 - 2014/6/3	$100.5\ \mathrm{mPa}$	$84.1\ \mathrm{kPa}$	$14.9\ \mathrm{kPa}$
47	low pressure	2014/6/22 - 2014/6/26	$135.9\ \mathrm{mPa}$	$42.5\ \mathrm{kPa}$	$7.5\ \mathrm{kPa}$
49	low ^{3}He	2014/11/18 - 2014/11/21	$7.72\ \mathrm{mPa}$	$84.1\ \mathrm{kPa}$	$15.1\ \mathrm{kPa}$

3.4 Event identification

3.4.1 Event display

An two-dimensional event display can be created based on the waveforms in the MWPC. The following four figures show the typical event displays for several kinds of events. The color shows the detected energy at the position, which corresponds to the place where an ionization process occurred in the TPC.

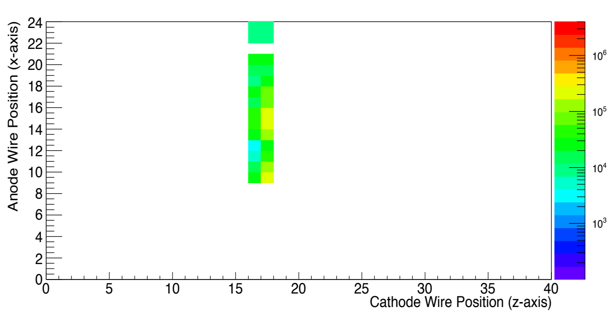

Figure 3.6: Beta-decay event.

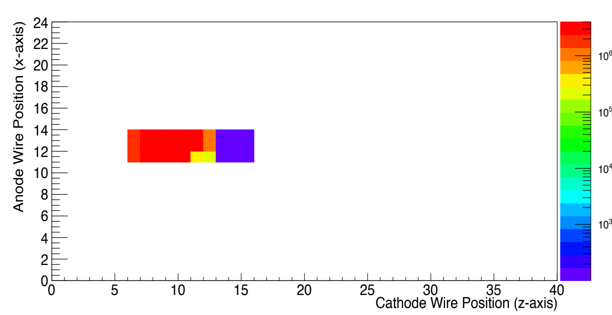

Figure 3.7: $^3\mathrm{He}(n,\ p)^3\mathrm{H}$ event.

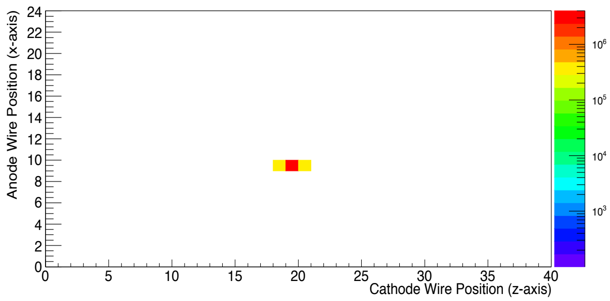

Figure 3.8: Fe X-ray absorption event.

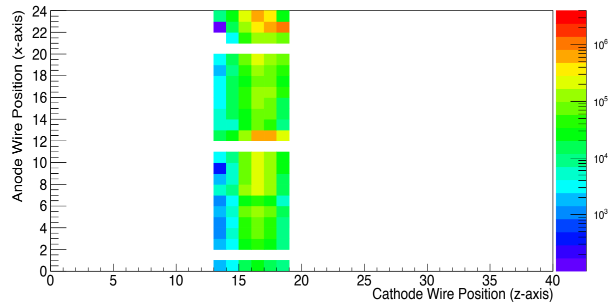

Figure 3.9: Cosmic ray event.

Both A beta-decay event and a $^3\mathrm{He}(n,\ p)^3\mathrm{H}$ event originate from the beam axis (corresponding to anode 11) because they are caused by an incident neutron. An electron from the beta-decay process (Q value is $782\ \mathrm{keV}$) usually passes through the TPC wall. Ions from the $^3\mathrm{He}(n,\ p)^3\mathrm{H}$ process locally loses their energy ($764\ \mathrm{keV}$) and have short tracks. A Fe X-ray event has an extremely short track, and the deposit energy corresponds to $5.9\ \mathrm{keV}$. A cosmic ray muon proceeds straight through the TPC, hence it resembles a straight line in the event display.

3.4.2 Cut condition

The cut conditions to extract the beta-decay and $^3\mathrm{He}(n,\ p)^3\mathrm{H}$ events are defined in Tables 3.5 and 3.6. Cut conditions specialized for extracting Fe events and cosmic rays events are listed in Tables 3.8 and 3.7 respectively.

Table 3.5: Definitions of the cut condition used for the beta-decay and the $^3\mathrm{He}(n,\ p)^3\mathrm{H}$ events.

name	condition
BasicCut	AMINT_MIN $<\ 250\ \mathrm{ch}$ and 0 $<$ ACE $<$ 23 and 0 $<$ CHCE $<$ 39
DriftCut	ADTIME $<\ 170\ \mathrm{ch}$
DCCut	ADC<4
AntiPointlikeCut	ASUM $>\ 5\ \mathrm{keV}$ or RANGE $>\ 100\ \mathrm{mm}$
LowFPHCut	FPH_MAX $<\ 25\ \mathrm{keV}$
HighFPHCut	FPH_MAX $>\ 25\ \mathrm{keV}$

Table 3.6: Cut conditions for the beta-decay and the $^3\mathrm{He}(n,\ p)^3\mathrm{H}$ events.

name	beta-decay cut	$^3\mathrm{He}(n,\ p)^3\mathrm{H}$ cut	expected rejecting events
BasicCut	○	○	—
DriftCut	○	×	$B^{\mathrm{int}\gamma}$ and B^{scat} events
DCCut	○	×	$B^{\mathrm{int}\gamma}$ and B^{scat}
AntiPointlikeCut	○	×	B^{point}
LowFPHCut	○	×	$S_{^3\mathrm{He}}$
HighFPHCut	×	○	S_β
FiducialTimeCut	○	○	—

Table 3.7: Cut condition for cosmic rays events.

condition	purpose
FNUM = 0	exclude events with large energy deposit
3 $<$ ANUM $<$ 23 & CHNUM$<$15	require analytically useful angle
ANUM = AMAXPOS - AMINPOS + 1	require no dead wires
1 $<$ AMINPOS $<$ 22 & 1 $<$ CHMNINPOS $<$ 39	exclude the events near the TPC wall
ASUM $>$ 30000	exclude low energy events

Table 3.8: Cut condition for Fe X-ray events.

condition	purpose
ANUM $<$ 4	require the point-like event
10000 $<$ ASUM $<$ 16000	require Fe X-ray energy ($5.9\ \mathrm{keV}$)
5 $<$ ACE $<$ 18	exclude the events near the TPC wall
ANUM = AMAXPOS - AMINPOS + 1	require no dead wires

3.5 Background

3.5.1 Types of background

In this experiment, various kinds of background are expected in the TPC, with respect to the signals of $^3\mathrm{He}(n,\ p)^3\mathrm{H}$ and beta-decay. Expected backgrounds and their descriptions are listed below. The subtraction method of these backgrounds is to be explained in Section 3.5.2.

- B^{const}
  There exits constant backgrounds that have no correlation with the neutron pulse, thus they have no time structure in the TPC. For example, cosmic rays which are not excluded by the veto counters, and environmental radiation from $^{40}\mathrm{K}$ and $^{208}\mathrm{Tl}$ are included in this background. The event rate for the background is evaluated to be $1.4\ \mathrm{cps}$ in the TPC [10].

- B^{rad}
  A LiF plate covers the internal wall of the TPC in order to capture scattered neutrons as explained in Section 2.2.2. When it captures a neutron, it produces a radioactive isotope on the plate, such as $^{8}\mathrm{Li}$ or $^{20}\mathrm{F}$. Both isotopes undergo beta-decay, and the half-lives are $838\ \mathrm{ms}$ and $11.0\ \mathrm{s}$ for $^{8}\mathrm{Li}$ and $^{20}\mathrm{F}$, respectively [20]. It is much longer than the repetition rate for a neutron pulse at MLF ($40\ \mathrm{ms}$), and much shorter than the measuring cycle (O(100) s). Thus we can assume that the processes reach equilibrium during the measurement, which means they have no TOF dependence in the TPC.

- $B^{\mathrm{ext}\gamma}$
  It is well known that most nuclei emit prompt γ rays when they capture neutrons. A neutron scattered during its flight in a beam pipe or the SFC can produce γ rays when it interacts with surrounding material. The γ rays produced outside of the TPC cause Compton scattering in the TPC with a certain probability. As a result, it produces an electron in the TPC, which can be background for beta-decay. The rate of the background has a strong correlation with the neutron flux in the beamline. Consequently, the background has TOF distribution which is almost same as that of a pulsed neutron.

- $B^{\mathrm{int}\gamma}$
  $^{12}\mathrm{C}$ in the $\mathrm{CO_2}$ gas and $^{6}\mathrm{Li}$ nuclei in the LiF plate produce prompt γ rays when each of them absorb a neutron. The γ rays become background for beta-decay in the same process as $B^{\mathrm{ext}\gamma}$. The starting point of its electron track corresponds to the position where Compton scattering occurs. As the attenuation length of Compton scattering in the TPC is much longer than the TPC size, the starting point is distributed more uniformly than that of signal events.

- B^{scat}
  It is calculated that a neutron is scattered by the gas molecules in the TPC with the probability of O(1)$\%$. The beta-decay and $^{3}\mathrm{He}(n,\ p)^{3}\mathrm{H}$ processes caused by a scattered neutron are treated as background in the analysis. The background is also relatively widely distributed in the TPC as with $B^{\mathrm{int}\gamma}$.

- B^{point}
  A $^{12}\mathrm{C}$ nucleus absorbs a neutron and recoils with the kinetic energy of $1.1\ \mathrm{keV}$, which is detected in the TPC. The energy is extremely small and localized compared to that of beta-decay (Q value is $782\ \mathrm{keV}$). The time structure of this background is the same as that of a signal event. Since the $^{12}\mathrm{C}$ nucleus produces prompt γ rays at the same time, it sometimes produces $B^{\mathrm{int}\gamma}$ at the same time.

- B^{nitro}
  It is observed that nitrogen gas is released into the TPC as an outgassing, which seems to be captured by the chamber when it is exposed to the atmosphere. The nitrogen causes a $^{14}\mathrm{N}(n,\ p)^{14}\mathrm{C}$ process (Q value is $626\ \mathrm{keV}$) in the TPC, and it can be a background for $^{3}\mathrm{He}(n,\ p)^{3}\mathrm{H}$. The pressure of the nitrogen gas increases with the lapse of time, hence the event rate of this background is also expected to increase. The time structure of this event is the same as that of a $^{3}\mathrm{He}(n,\ p)^{3}\mathrm{H}$ event, hence it cannot be subtracted by the TOF analysis.

- B^{oxy}
  It is expected that there are ^{17}O atoms in the TPC, which undergo $^{17}\mathrm{O}(n,\ \alpha)^{14}$C processes (Q value is $1818\ \mathrm{keV}$) in the TPC. This process is also a background for the $^{3}\mathrm{He}(n,\ p)^{3}\mathrm{H}$. The time structure of this events is the same as that of a $^{3}\mathrm{He}(n,\ p)^{3}\mathrm{H}$ events. The number of this background can be calculated based on the CO_2 pressure if we assume the natural isotropic abundance.

3.5.2 Background subtraction processes

It is expected that various kinds of background events exist in the TPC as described in below section. In order to derive the neutron lifetime from the acquired data, it is imperative to separate these background events from the signal events. Figure 3.10 shows the overall flow to subtract the expected background events listed in Section 3.5.1.

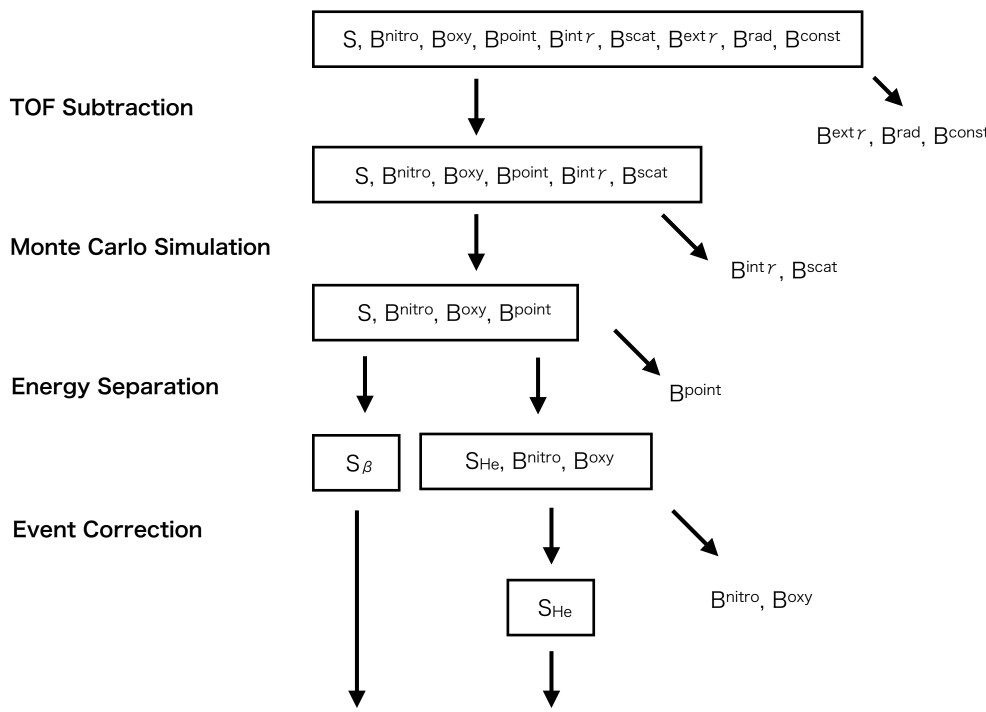

Figure 3.10: Overall flow of background subtraction.

- TOF subtraction
  The TOF subtraction method uses data acquired in both the passing and dumping mode (see Secion 3.3). The difference of the two data indicates the event number of background, and we can subtract $B^{\mathrm{ext}\gamma}$, B^{rad}, and B^{const} using this method. The detailed procedure is discussed in the next subsection.

- Monte Carlo simulation
  The subtraction of $B^{\mathrm{int}\gamma}$ and B^{scat} are conducted by the Monte Carlo simulation. The absolute number of these kinds of events can be determined based on the cross sections of these processes.

- Energy separation
  The remaining events after the previous subtraction are separated based on the energy loss process in the TPC. They are classified as point-like events (B^{point}), localized-deposit events ($S_{^3\mathrm{He}}$, B^{nitro}, and B^{oxy}), or others (S_β). The separation of B^{point} are conducted by the AntiPointLikeCut defined in Table 3.5. The separation of the other two kinds of events is discussed in Section 5.2.

- Event correction
  The TPC does not have the energy resolution to separate B^{nitro}, B^{oxy}, and $S_{^3\mathrm{He}}$ because the multiplication factor decreases due to space charge effect. Thus the numbers of these backgrounds are needed to be corrected in the end. The correction amount for B^{oxy} is discussed in Section 5.1. The correction of B^{nitro} is estimated using the low-gain data, and the correction amount is determined as (1.45±0.23)% for the gas 42 (defined in Section 3.3.2) by R. Sakakibara [21].

3.5.3 TOF Subtraction

The TOF subtraction method is used to separate $B^{\mathrm{ext}\gamma}$, B^{rad}, and B^{const} from the signal events. This method uses a set of data in the passing and dumping mode. Figure 3.11 represents the schematic TOF distribution of the signals and expected backgrounds listed in Section 3.5.1. The left and right figures show the distribution in the passing and dumping mode, respectively. Several backgrounds, such as $B^{\mathrm{ext}\gamma}$ and B^{const}, are not affected by the shutter condition at all, and thus the amount can be estimated using the dumping mode data. Moreover, B^{rad} can also be estimated by comparing the two data sets in the sideband time as defined in Section 3.2. The relevant calculations are explained as follows.

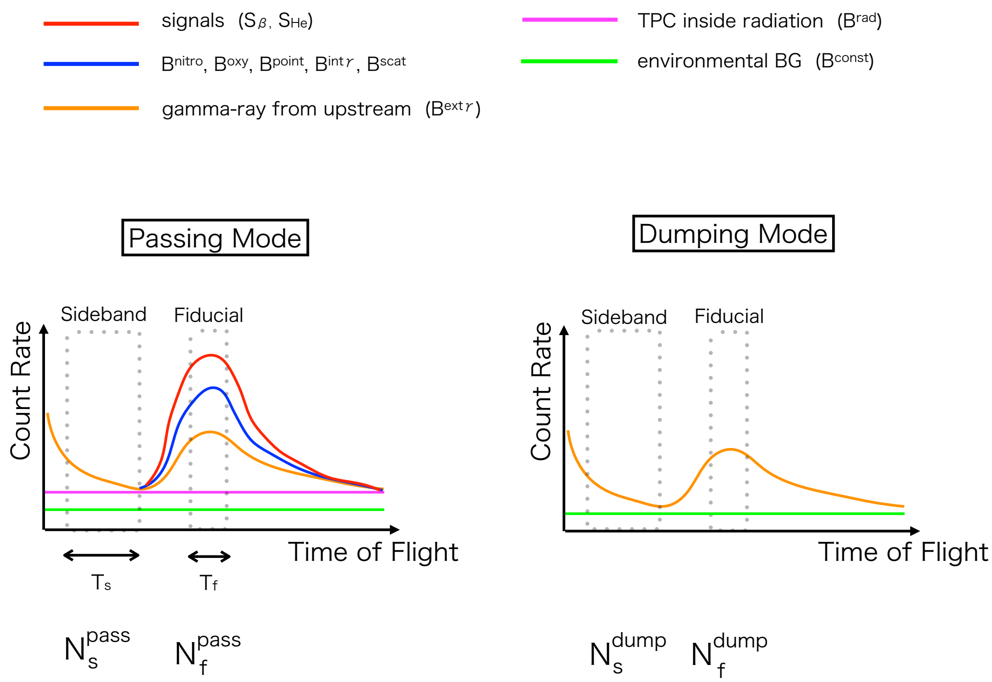

Figure 3.11: TOF distribution of signal and background in the passing mode (left) and the dumping mode (right).

Here, N_s^{pass} is the total count of the sideband time in the passing mode, whereas N_f^{pass} is in the fiducial time. $N_s^{\rm dump}$ and $N_f^{\rm dump}$ are defined similarly for data in the dumping mode. T_f and T_s represent the time width for the fiducial time and the sideband time, respectively. B^i represents the event rate of each background type i. Since the $B^{\rm ext\gamma}$ in the fiducial time does not coincide with that in the sideband time, they are expressed as $B_{\rm f}^{\rm ext\gamma}$ and $B_{\rm s}^{\rm ext\gamma}$ respectively. S represents the sum of a beta-decay a ${}^3{\rm He}(n,\ p){}^3{\rm H}$.

$$\frac{N_{\rm s}^{\rm pass}}{T_{\rm s}} = B^{\rm const} + B^{\rm rad} + B_{\rm s}^{\rm ext\gamma} \ , \tag{3.6}$$

$$\frac{N_{\rm f}^{\rm pass}}{T_{\rm f}} = B^{\rm const} + B^{\rm rad} + B_{\rm f}^{\rm ext\gamma} + +B^{\rm point} + B^{\rm int\gamma} + B^{\rm scat} + B^{\rm nitro} + B^{\rm oxy} + S \ , \tag{3.7}$$

$$\frac{N_{\rm s}^{\rm dump}}{T_{\rm s}} = B^{\rm const} + B_{\rm s}^{\rm ext\gamma} \ , \tag{3.8}$$

$$\frac{N_{\rm f}^{\rm dump}}{T_{\rm f}} = B^{\rm const} + B_{\rm f}^{\rm ext\gamma} \ . \tag{3.9}$$

Thus, the subtraction in the passing mode excludes $B^{\rm env}$ and $B^{\rm rad}$ from the signal events as

$$\frac{N_{\rm f}^{\rm pass}}{T_f} - \frac{N_{\rm s}^{\rm pass}}{T_{\rm s}} = (B_f^{\rm ext\gamma} - B_s^{\rm ext\gamma}) + B^{\rm point} + B^{\rm int\gamma} + B^{\rm scat} + B^{\rm nitro} + B^{\rm oxy} + S \ . \tag{3.10}$$

In order to exclude the $B^{\mathrm{ext}\gamma}$ term, the subtraction result in the dumping mode is also used as

$$\left(\frac{N_{\mathrm{f}}^{\mathrm{pass}}}{T_f} - \frac{N_{\mathrm{s}}^{\mathrm{pass}}}{T_{\mathrm{s}}}\right) - \frac{F_{\mathrm{pass}}}{F_{\mathrm{dump}}}\left(\frac{N_{\mathrm{f}}^{\mathrm{dump}}}{T_{\mathrm{f}}} - \frac{N_{\mathrm{s}}^{\mathrm{dump}}}{T_{\mathrm{s}}}\right) = B^{\mathrm{point}} + B^{\mathrm{int}\gamma} + B^{\mathrm{scat}} + B^{\mathrm{nitro}} + B^{\mathrm{oxy}} + S \ , \tag{3.11}$$

where F_{pass} and F_{dump} are the scaling parameters representing the total neutron flux in the passing and dumping mode, respectively. The total number of detected events in the flux monitor (see Section 2.2.6) is used as the scaling parameter.

3.6 Calibration

This section describes the calibration method of the energy and drift velocity in this experiment.

3.6.1 Energy calibration

The detected energy in the TPC is calibrated using the Fe X-ray events. There are two modes for Fe X-ray data, i.e. Fe(up) and Fe(down) (see Section 3.3.1). The distribution in the two modes is shown in Figure 2.11. By fitting the distribution with a Gaussian distribution, the ASUM value corresponding to $5.9\ \mathrm{keV}$ can be evaluated. The attenuation length can be determined using the Fe(up) and Fe(down) data ($\mathrm{ASUM_{up}}$ and $\mathrm{ASUM_{down}}$) as

$$\lambda = \frac{225\ \mathrm{mm} - 75\ \mathrm{mm}}{\log\left(\frac{\mathrm{ASUM_{up}}}{\mathrm{ASUM_{down}}}\right)} \ . \tag{3.12}$$

Based on the attenuation length, the estimated ASUM value at the center of TPC ($\mathrm{ASUM_{center}}$) can be calculated as

$$\begin{aligned} \mathrm{ASUM_{center}} &= \mathrm{ASUM_{up}} e^{-\frac{75\ \mathrm{mm}}{\lambda}} \ , &(3.13) \\ &= \sqrt{\mathrm{ASUM_{up}}\mathrm{ASUM_{down}}} \ . &(3.14) \end{aligned}$$

The $\mathrm{ASUM_{center}}$ is used as the energy calibration factor of anode wires. The calibration factor of APH is similarly determined. Regarding field wires, the factor is derived by multiplying measured calibration ratio (1/46.5) by the factor of anode wires.

It is known that the multiplication factor in the TPC decreases with time due to the outgassing. Figure 3.12 shows the long-term time variation of the $\mathrm{ASUM_{up}}$ and $\mathrm{ASUM_{down}}$ values of Gas 42. We can see the significant decrease of the values during the measurement (about 15% during the 1 week operation). The variation of the $\mathrm{ASUM_{up}}$ and ASUM_{down} are fitted with an exponential function. The data acquired in May 27 is not included in the fitting because it seems that the gas in the TPC was not diffused at that time. Based on the fitting results, the $\mathrm{ASUM_{center}}$ can also be derived as a function of the time, which is also shown in Figure 3.12.

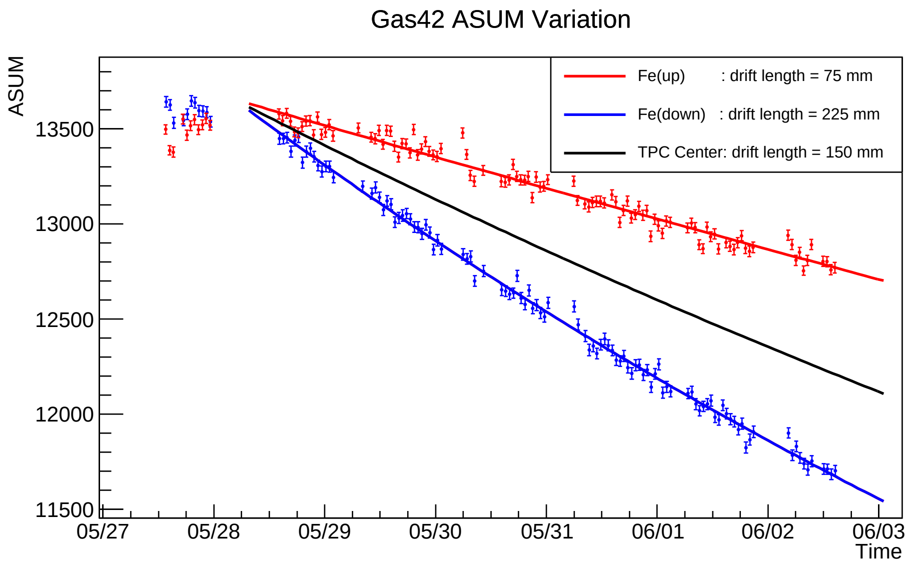

Figure 3.12: ASUM variation for Fe X-ray data during the measurement of Gas 42 [22].

3.6.2 Drift velocity calibration

The electrons produced by the ionization process drift towards the MWPC with the velocity of about 1 μs. The drift velocity is used to calculate RANGE parameter (defined in Section 3.1.2), which is used for the cut condition of beta-decay. Since the drift velocity fluctuates according to the gas condition, its calibration is required for every gas filling.

The velocity is evaluated using the ADTIME parameter (defined in Section 3.1.2), which represents the maximum difference of the drift time among all anode wires. Figure 3.13 shows the ADTIME (defined in Section 3.1) distribution of cosmic ray events for Gas 42. The peak at around 27 μs corresponds to the processes that cosmic ray muon passed vertically through the TPC. In order to quantitatively evaluate the ADTIME value of the peak, the histogram is fit by the following function

$$F(x;\ p_0,\ p_1,\ p_2,\ p_3,\ p_4) = p_0 \exp\left[p_1(x-p_2)\right] \mathrm{Erf}\left(\frac{x-p_3}{p_4}\right) \quad , \tag{3.15}$$

where $p_0 \sim p_4$ are the fitting parameters and $Erf(x)$ is the error function defined as follows

$$\mathrm{Erf}(x) = \frac{2}{\sqrt{\pi}} \int_0^x e^{-t^2} dt \quad . \tag{3.16}$$

In Eq. (3.15), p_3 is expected to roughly represent the ADTIME of the peak, which is evaluated to be 27.8 μs for Gas 42. It corresponds to the elapsed time that the electron at the bottom of the TPC drifts towards the MWPC (29.5 cm). Therefore the drift velocity can be calculated as

$$v_{drift} = \frac{29.5 \text{ cm}}{27.8\ \mu\text{s}} = 1.06 \text{ cm}/\mu\text{s} \quad . \tag{3.17}$$

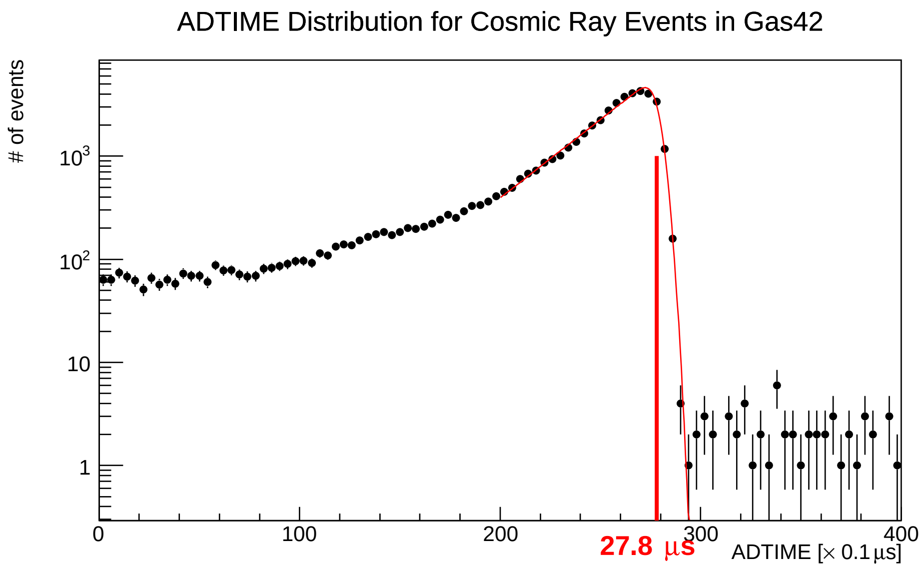

Figure 3.13: ADTIME distribution of cosmic ray events for Gas 42 composition. The maximum drift time is derived as $27.8\ \mu$s.

Table 3.9: Evaluated drift velocity for three types of gas. The uncertainties in the table only come from the fitting uncertainties.

gas number	total pressure [kPa]	electric field [V/cm]	drift velocity [cm/μs]
42	100	300	1.0603 ± 0.0004
47	50	240	1.628 ± 0.003
49	100	300	1.051 ± 0.002

Chapter 4

Simulation

In order to estimate the neutron lifetime using Eq. (1.29), it is essential to evaluate the efficiencies of both the beta-decay (ε_β) and the $^3\mathrm{He}(n,\ p)^3\mathrm{H}$ ($\varepsilon_{^3\mathrm{He}}$) processes. This is carried out using the Monte Carlo simulation which we developed in a way so as to reproduce the actual experimental conditions faithfully. Details of the simulation are described in this chapter. First, the general outline of the simulation process is briefly explained. Next, several physical processes implemented into the simulation are discussed in detail.

4.1 Flow of the simulation

Figure 4.1 shows the overall flow of the simulation for this experiment. First, various kinds of particle interactions in the detector are simulated by Geant4 simulation [23]. After that, the response of the detector, i.e. the waveforms of all wires, are simulated based on the results of the Geant4 simulation. The acquired waveforms are analysed by the same algorithm as the ones obtained in the experiment.

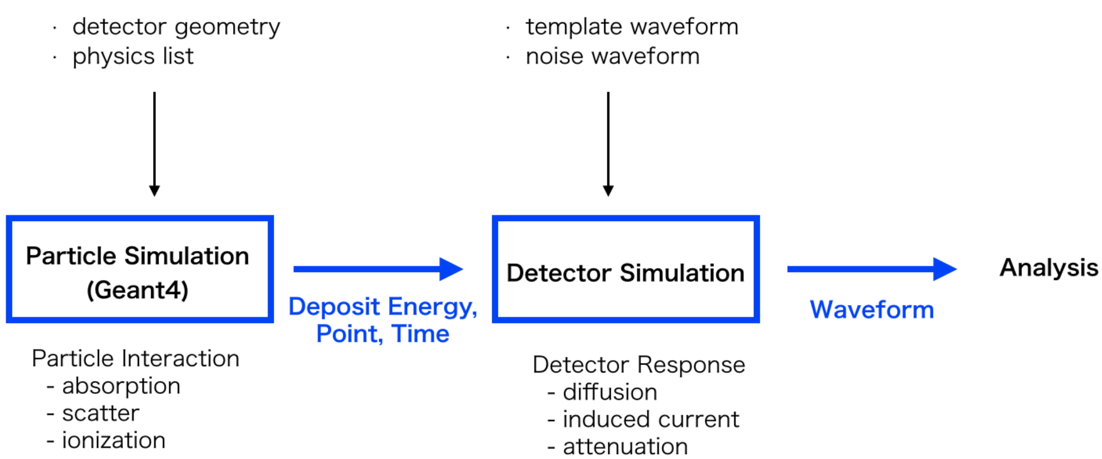

Figure 4.1: Overall simulation process.

4.1.1 Particle simulation

We use the Geant4 software in order to simulate various kinds of particle interactions in the TPC. Geant4 is a simulation toolkit for particle interactions, and it is widely used not only in particle physics but also in nuclear physics and medical science. We use the "FTFP BERT PEN" package, which is known for its high reproducibility especially for processes involving low-energy neutrons. Figure 4.2 shows the overview of the detector we constructed using Geant4.

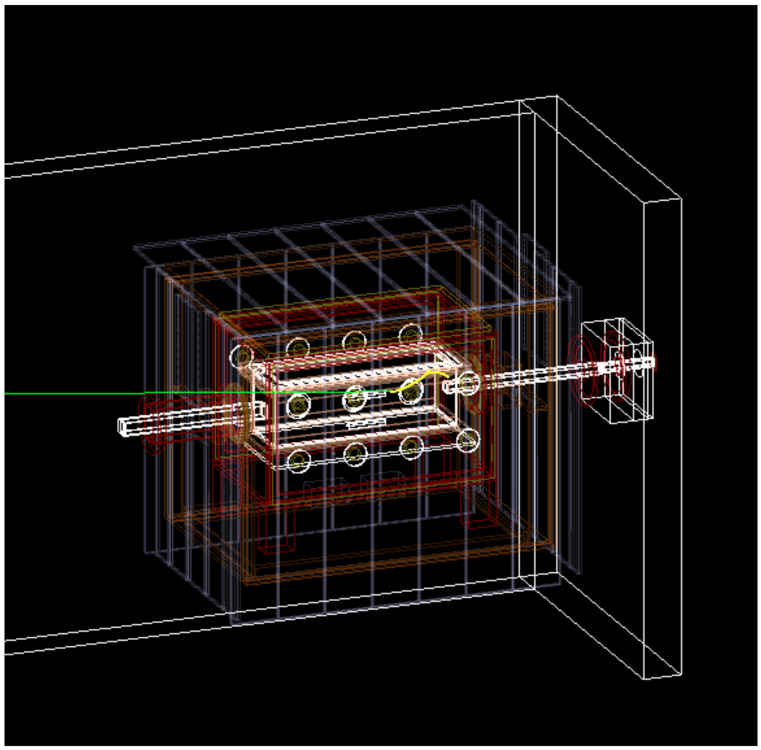

Figure 4.2: Detector and surrounding devices in Geant4 simulation.

The implementation of each process is briefly explained as follows.

- Beta-decay
  A stationary neutron is set at a point in the TPC in order to simulate the beta-decay process. The neutron decays and emits a proton, an electron, and an anti-neutrino isotropically. The coordinate of the point is randomly selected in order to reproduce the experimental condition; The z coordinate (beam axis) is selected based on the position of a neutron bunch whereas other coordinates are determined based on the distribution acquired by a two-dimensional position detector.

- $^3\mathrm{He}(n,\ p)^3\mathrm{H}$
  A $572\ \mathrm{keV}$ proton and a $191\ \mathrm{keV}$ triton are emitted to the opposite direction isotropically in the $^3\mathrm{He}(n,\ p)^3\mathrm{H}$ simulation. The candidate of the reaction point is completely same as that of beta-decay.

- Cosmic ray
  A positive or negative muon (μ^+, or μ^-) are emitted toward the TPC in the cosmic ray simulation. Its particle ratio in the simulation is $\mu^+/\mu^- = 1.3$, which is the observed particle ratio for 10 GeV to 1 TeV muons [1]. Both the angle distribution ($dN/d\Omega \sim \cos^2\theta$, where θ represents a zenith angle) and the energy distribution ($dN/dE \sim \exp[-(\log E(\mathrm{eV}) - 8.278)^2/(2 \times 1.491^2)]$) are adjusted in order to reproduce the real distribution.

- Fe X-ray
  There are two modes for Fe X-ray data as described in Section 3.3. Two types of mode with different Fe source position is implemented also in the simulation. The X-ray is emitted horizontally from the source position. Since the real ^{55}Fe produces several kinds of X-rays (5.9 keV for K_α and 6.5 keV for K_β), the energy is randomly selected in the simulation according to the actual probability [20].

- Scattering process
  The scattering process for a low-energy neutron is not implemented in the Geant4 physics model. Thus its differential cross section of the scattering is calculated using the semi-classical model proposed by N. Z. Alcock et al. [24]. Based on the calculated cross sections, the map of the interaction caused by scattered neutrons can be derived. In this way, the beta-decay and $^3\mathrm{He}(n,\ p)^3\mathrm{H}$ processes caused by scattered neutrons (B^{scat}) can be simulated.

4.1.2 Detector simulation

Based on the deposit energy and position simulated by Geant4, output waveforms of all wires are created in this detector simulation process. Figure 4.3 shows the processing flow in the detector simulation. First, the time distribution of electrons at every wire in the MWPC is produced, where various kinds of physical processes, such as diffusion, attenuation, and recombination, are taken into consideration. Next, the template waveforms are created using template waveforms. Finally, output waveforms with electrical noise and pedestal offset are created.

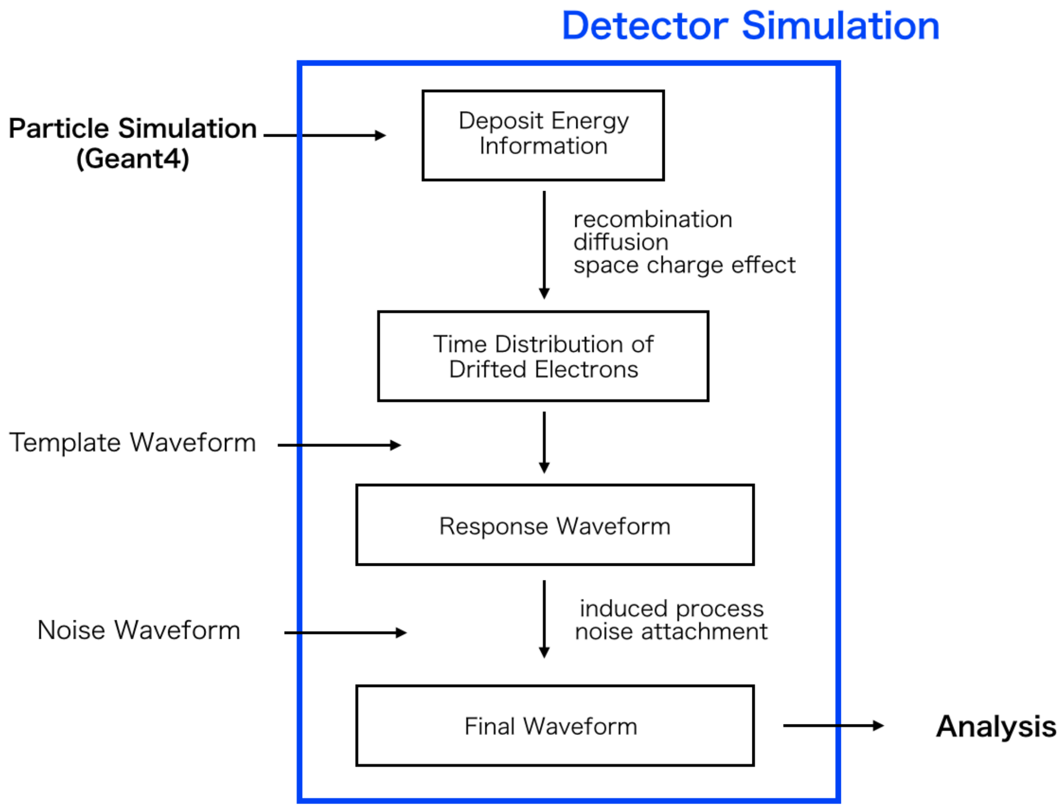

Figure 4.3: Overall process of detector simulation.

4.2 Trigger simulation

Since a trigger condition of DAQ determines the quality of acquired data, it is extremely important to reproduce the experimental trigger also in the simulation. In this experiment, the trigger demands that a pulse height of at least one anode wire exceeds the threshold level of a discriminator ($15\ \mathrm{mV}$ or $\sim 30\ \mathrm{ch}$). The threshold value can be determined by comparing the pulse height of both "hit event" (the event which exceeds the discriminator threshold) and "not-hit event" (the event which does not exceed the discriminator threshold). The hit judgment is performed based on the TDC data because the time that a pulse heigh exceeds the threshold is recorded in the TDC.

Figure 4.4 shows the pulse height distribution of an anode wire for cosmic rays. The red histogram represents the pulse height for not-hit events, and the black one represents the pulse height for hit events. The threshold level must exist at the border of the two histograms. An optimum value is decided as the value d which minimizes $F(d)$ parameter defined as follows

$$F(d) \equiv N_{\mathrm{nothit}}(\mathrm{ch} > d) + N_{\mathrm{hit}}(\mathrm{ch} < d) \ , \tag{4.1}$$

where $N_{\mathrm{nothit}}(\mathrm{ch} > d)$ is the number of not-hit events whose pulse height exceeds d ch, and $N_{\mathrm{hit}}(ch < d)$ is the number of hit events whose pulse height falls below d ch. The $F(d)$ represents the total number of misclassified events at a threshold of d ch.

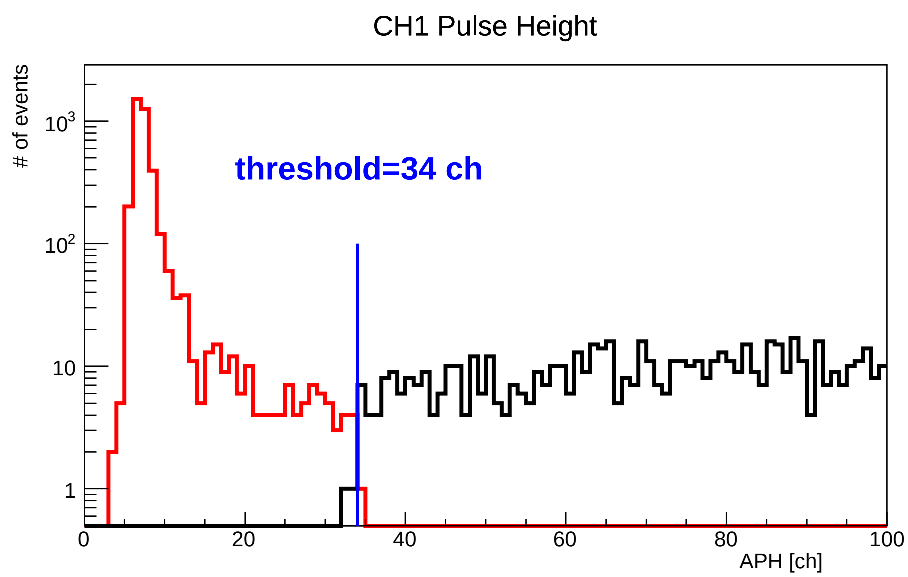

Figure 4.4: Pulse height distribution for cosmic rays. The black histogram represents the pulse height which exceeds the discriminator threshold, and the red histogram represents the pulse height which does not exceed the threshold.

The threshold level of each discriminator is evaluated for every cosmic rays data ($\sim$ 6000 events for 100 s). Figure 4.5 shows the threshold level distribution for 21 cosmic rays data. The average is adopted as the threshold level used in the simulation (listed in Table 4.1). It is required that the pulse height of at least one anode wire exceeds the threshold values for analysis condition in the simulation.

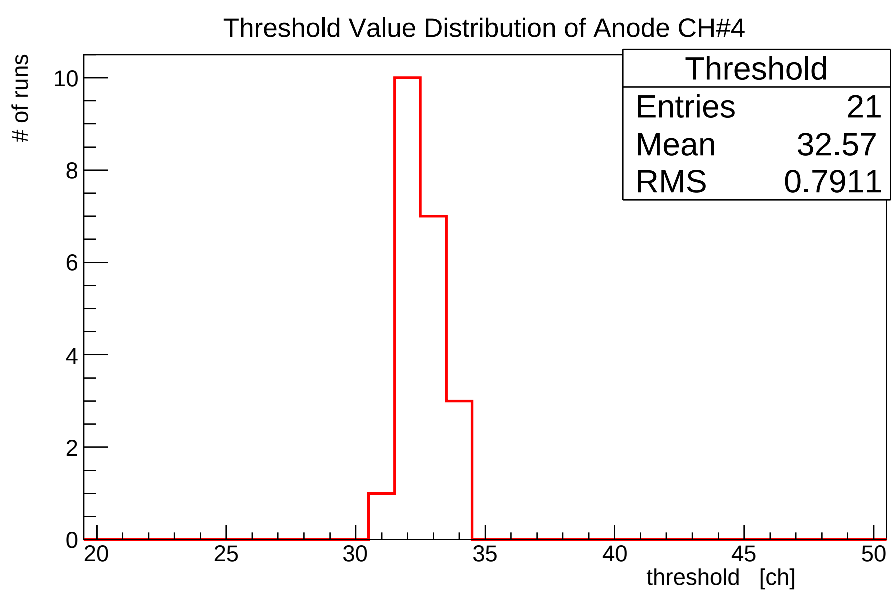

Figure 4.5: Evaluated threshold distribution for an anode wire.

Table 4.1: Threshold values evaluated for each anode wire.

anode #	mean / standard deviation [ch]		anode #	mean / standard deviation [ch]
0	29.9 / 0.6		12	31.5 / 1.1
1	32.5 / 0.9		13	32.1 / 0.9
2	32.8 / 0.8		14	35.7 / 1.2
3	33.1 / 0.9		15	33.7 / 1.2
4	32.6 / 0.8		16	37.6 / 0.9
5	35.1 / 0.9		17	37.8 / 0.7
6	33.6 / 0.9		18	36.4 / 1.0
7	29.7 / 0.9		19	35.3 / 1.0
8	35.6 / 0.7		20	38.5 / 0.8
9	34.7 / 0.9		21	38.2 / 0.9
10	36.6 / 0.8		22	41.4 / 0.6
11	34.9 / 0.9		23	40.8 / 0.7

4.3 Induced Current

A wire chamber uses an induced current caused by avalanche multiplication to detect drifting electrons. The induced current is mainly generated by the potential change caused by the movement of ions produced by the avalanche process. The ions generate induced current not only at the wire where avalanche multiplication occurs but also at neighboring wires. This process must be taken into consideration for the waveform simulation. In this subsection, the quantitative understanding of the process is discussed. The method to implement the effect into the simulation is described in Section 4.4.

In order to estimate the induced current, a multiplication process in the MWPC was fully simulated by the Monte Carlo simulation. First, three-dimensional electric field in the MWPC is calculated by FEM (Finite Element Method) using ANSYS 15.0 [25]. The MWPC structure is simplified as shown in Figure 4.6, and boundary conditions (listed in Table 4.2) are set in order to reproduce the experimental condition. The calculated electric potential is shown in Figure 4.7.

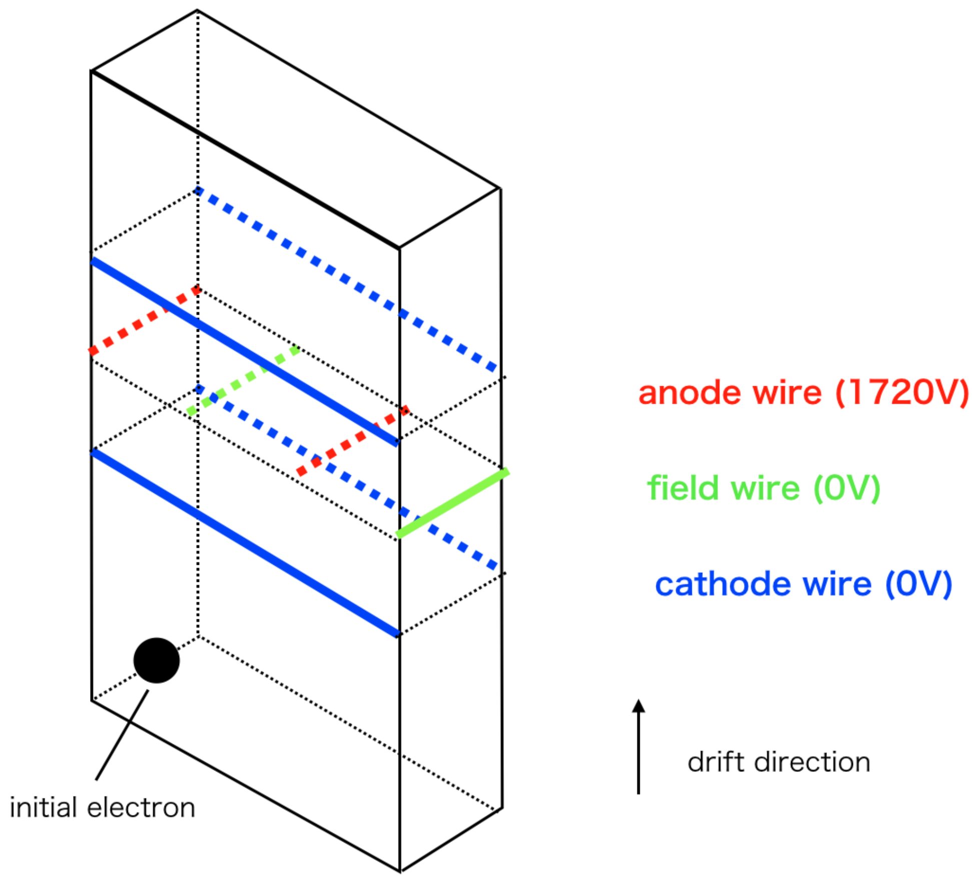

Figure 4.6: Simplified MWPC structure for calculating electric potential.

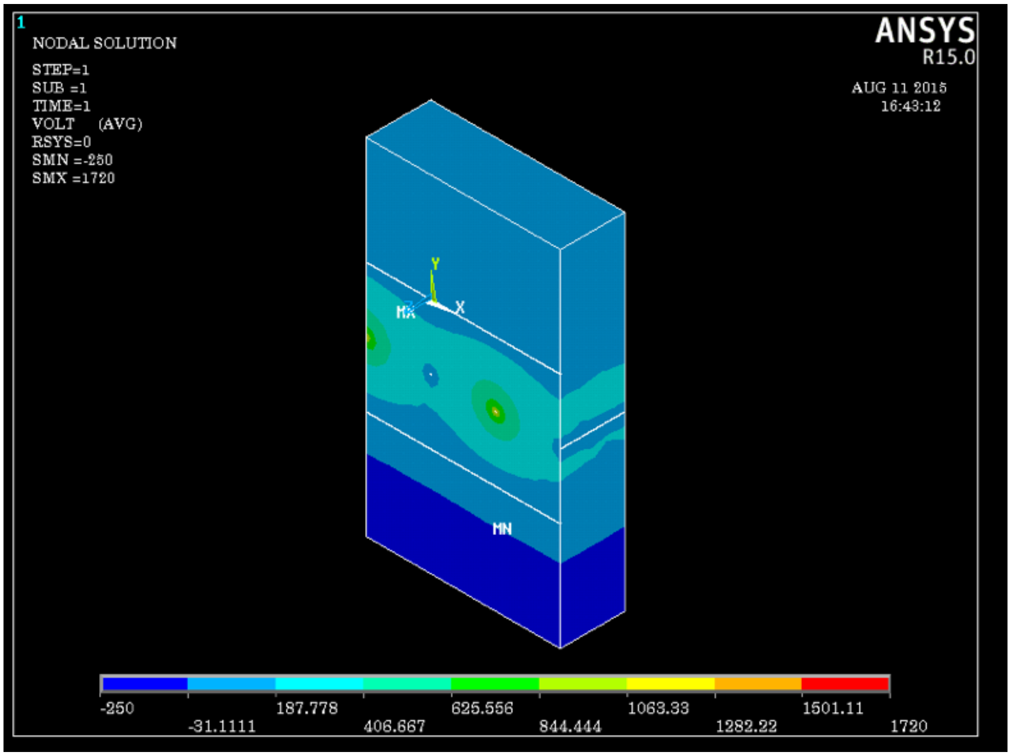

Figure 4.7: Calculated electric potential.

Table 4.2: Setup condition for calculating electric field in the MWPC.

part	number	condition
anode wire (ϕ20 μm)	1+0.5	+1720 V
field wire (ϕ50 μm)	1+0.5	+0 V
cathode wire (ϕ50 μm)	0.5$\times$ 4	+0 V
top board	1	+100 V
bottom board	1	$-$300 V
side board	4	mirror periodicity boundary condition

Next, an avalanche process in the MWPC is simulated using Garfield software [26]. Garfield is a simulation toolkit developed by CERN, and it is specialized for the avalanche simulation in a drift chamber. When the initial position of an electron is assigned, a series of an avalanche processes for the electron can be simulated based on the calculated electric field. The position of an initial electron is set at 15 mm right under an anode wire as displayed in Figure 4.6. The electron drifts upwards and it causes avalanche multiplication within O(100) μm from the anode wire.

In order to simulate the induced current at wires, the Shockley-Ramo theorem [27] was used. This theorem states that the induced current for an electrode (i) due to the movement of a charged particle (charge:q, velocity:$\vec{v}$) is expressed as

$$i = q\vec{v} \cdot \vec{E}_w \quad , \tag{4.2}$$

where $\vec{E}_w$, or weighted electric field, represents a dimensionless electric field for which 1 V is assigned to the electrode whose current we want to know and 0 V is assigned to the other electrodes. As an example, the weighted potential for a field wire calculated by ANSYS is shown in Figure 4.8. Note that the mirror periodicity for the side boards is maintained as a boundary condition. Weighted electric field for four kinds of wires are calculated by ANSYS.

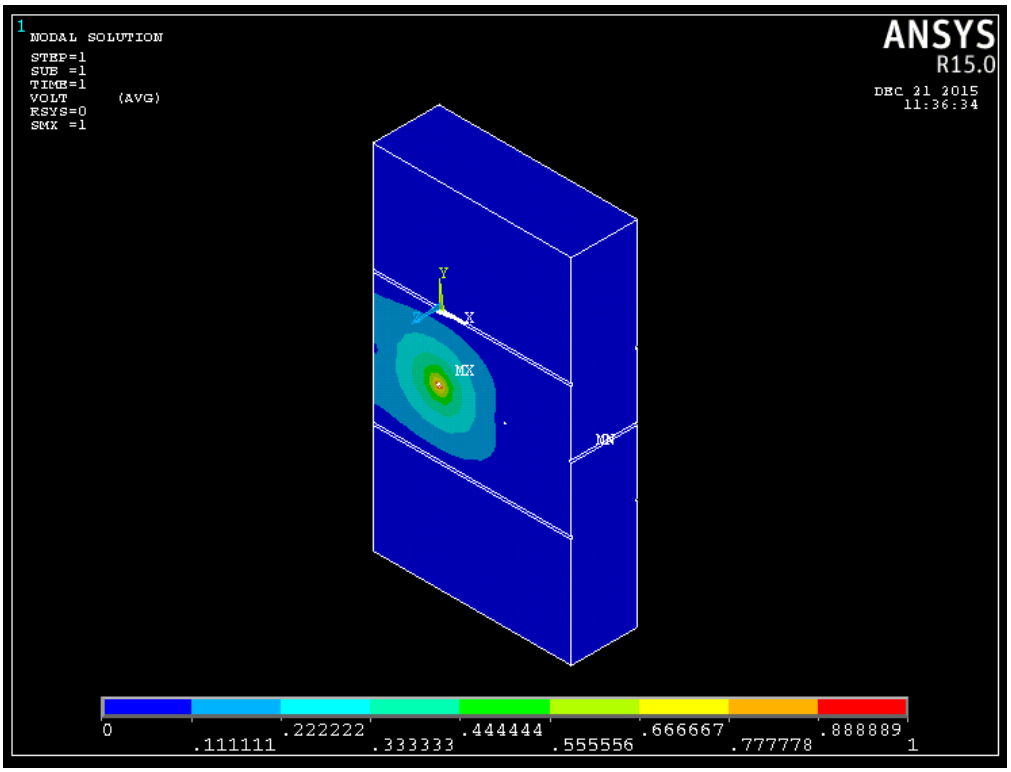

Figure 4.8: Weighted electric potential for a field wire.

Figure 4.9 shows a typical time distribution of induced current calculated using the Shockley-Ramo theorem. The red and blue line represent the current induced by ionization electrons and ions, respectively. In can be seen that the two have completely different time structure. The current from electrons flows instantaneously at the avalanche timing (240 ns), whereas the current from ions flows comparatively longer even after the avalanche timing. In the end both currents are added together to represent the total induced current of the wire. Figure 4.10 shows the total induced current of the two anode wires and two field wires in Figure 4.6. The wire names are defined in Figure 4.11. We can see the natural tendency that the closer the wire is to the anode wire, the larger the induced current is. Since only the current at avalanche wire has a reverse sign, it is inverted for convenience.

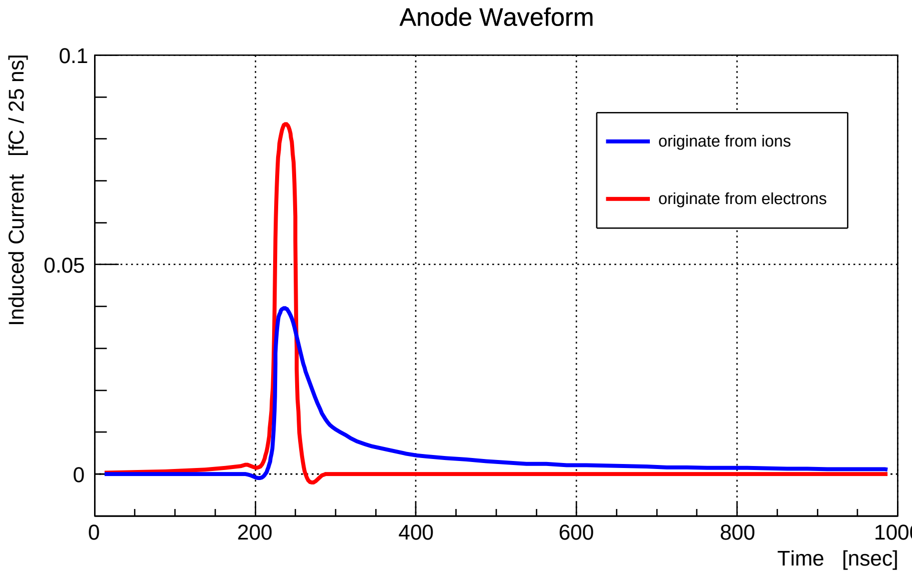

Figure 4.9: Simulated time distribution of current induced at an anode wire.

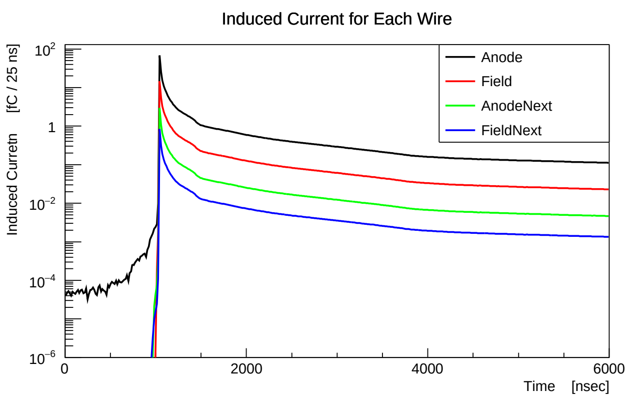

Figure 4.10: Simulated time distribution of Induced current at several wires.

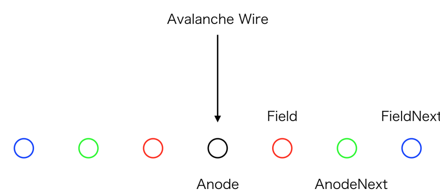

Figure 4.11: Wire name definition.

The values of simulated induced charge (integral of Figure 4.6) are listed in Table 4.3. Although the avalanche gain parameters are extremely different between processes, the ratios of induced charge to "Anode" wire are almost the same. This signifies that the induced charge ratio is independent on the multiplication factor. The average charge ratios to "Anode" wire are evaluated as -0.212, -0.0424, and -0.0122 for "Field" wire, "AnodeNext" wire, and "FieldNext" wire, respectively.

Table 4.3: Induced charge values and their ratios to the anode wire.

process	gain	Anode [fC]	Field [fC]	AnodeNext [fC]	FieldNext [fC]	Field/Anode	AnodeNext/Anode	FieldNext/Anode
0	6942	-0.0438	0.00930	0.00186	0.000536	-0.212	-0.0424	-0.0122
1	3851	-0.0244	0.00517	0.00103	0.000298	-0.212	-0.0424	-0.0122
2	7265	-0.0457	0.00973	0.00194	0.000560	-0.213	-0.0425	-0.0122
3	1713	-0.0108	0.00230	0.000460	0.000133	-0.212	-0.0424	-0.0122
4	660	-0.0042	0.000883	0.000177	0.0000510	-0.211	-0.0423	-0.0122
5	8321	-0.0524	0.0111	0.00222	0.000641	-0.212	-0.0425	-0.0122
6	4812	-0.0304	0.00644	0.00129	0.000371	-0.212	-0.0425	-0.0122
average						-0.212	-0.0424	-0.0122

4.4 Waveform in the simulation

In this section, details about procedure to create waveforms are discussed. Figure 4.12 shows the overall process to create the waveforms of each kind of wire in the detector simulation. The waveforms of high-gain wires (anode and high-gain cathode) are created based on Geant4 simulation result. The waveforms of field wires are created using the result of induced simulation. The parameters about the wires is used in the current analysis at all, hence the waveforms of low-gain cathode wires are not created in the simulation.

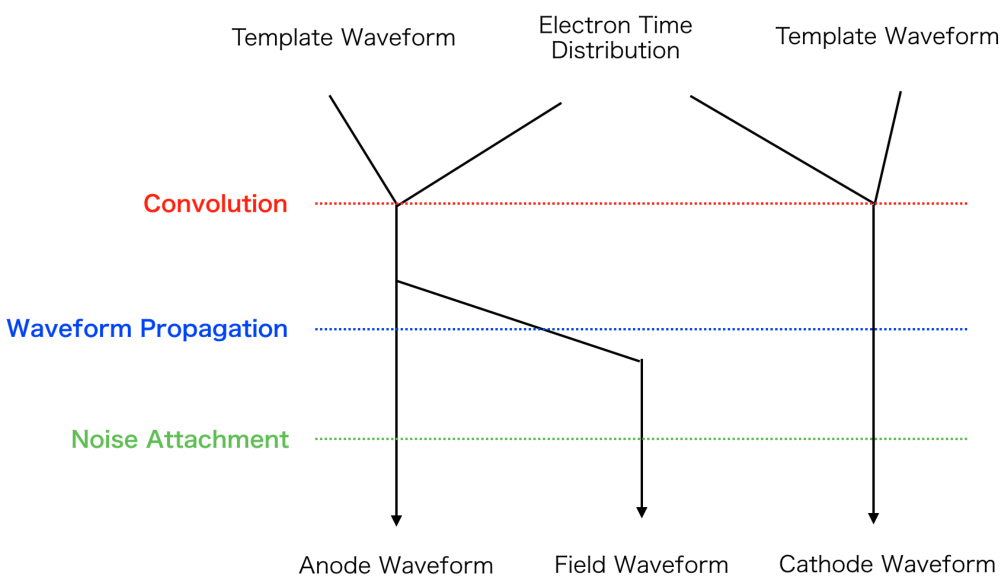

Figure 4.12: Procedure to make all kinds of waveforms in the detector simulation.

4.4.1 Convolution

For the high-gain wire, the waveform is created by convoluting the time distribution of drifting electrons and a template waveform. The time distribution of drifting electrons is simply calculated based on the ionization positions simulated by Geant4. The template waveform is a basic waveform reflecting the shaping time of the preamplifier, which is created by averaging the waveform of Fe X-ray events. When the template waveform and time distribution of electrons are expressed $T(t)$ and $N_e(t)$ respectively, the response waveform $R(t)$ can be calculated as

$$
\begin{aligned}
R(t) &= 0 && (1\ \mathrm{ch} \leq t < 299\ \mathrm{ch}),\\
R(t) &= G\int_0^{t-299} N_e(\tau)T(t-\tau)d\tau && (299\ \mathrm{ch} \leq t \leq 1000\ \mathrm{ch}),
\end{aligned}
$$

where $t = 299$ ch is the triggered timing (see Section 2.23), and G is a random number which have a Gaussian distribution. Its mean and standard deviation were determined so as to reproduce the Fe X-ray experimental distribution. Figure 4.14 shows the experimental data and optimized simulation distribution.

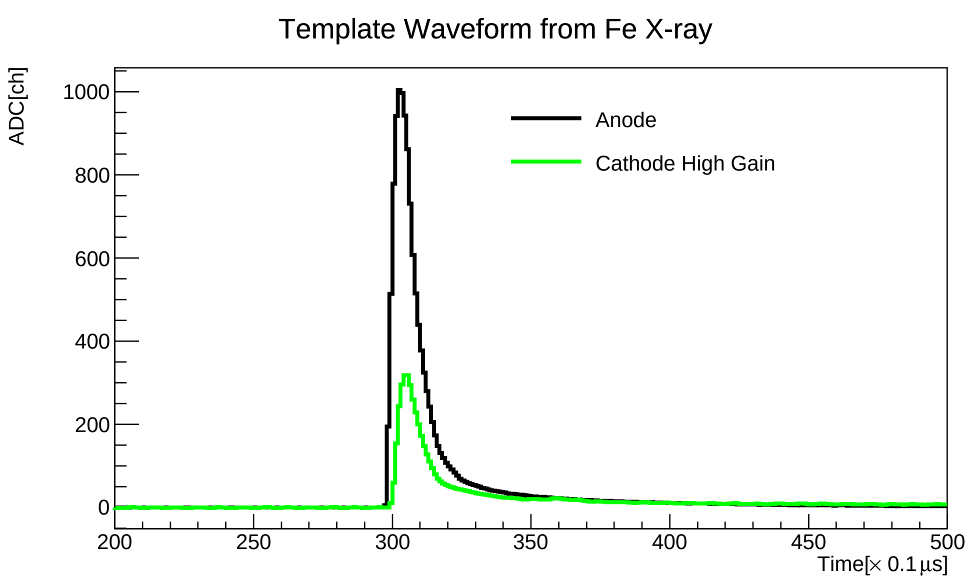

Figure 4.13: Created average waveform for high-gain wire from Fe X-ray data.

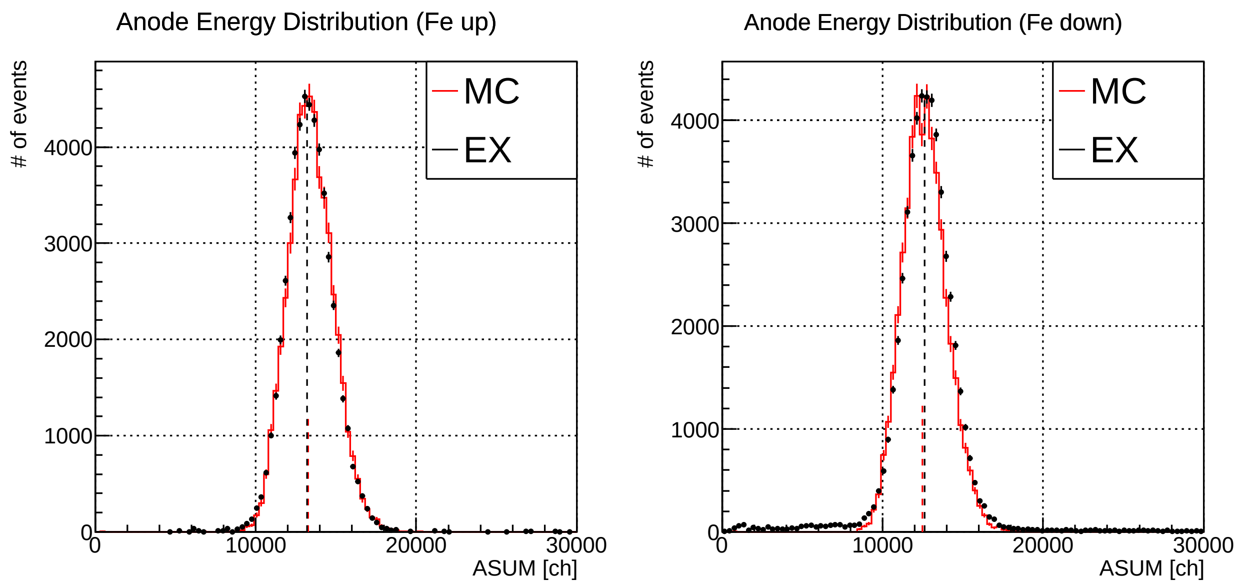

Figure 4.14: Fe X-ray energy comparison of experimental data and calibrated simulation.

4.4.2 Induced simulation

The ions generate induced current not only at the wire where avalanche multiplication occurs but also at neighboring wires. The induced effect for both anode and field wires is simulated as described in Section 4.3, which is $f_1 = 0.212$, $f_2 = 0.0424$, and $f_3 = 0.0122$. f_1 and f_2 represent the induced charge ratio of the nearest anode and field wires, respectively. f_3 is the charge ratio of the second nearest field wires. Therefore, the waveform of the i-th field wires $A_i^{\rm new}(t)$ and $F_i^{\rm new}(t)$ including the induced effect can be created based on the original waveform of anode wires ($A_i^{\rm old}(t)$) as

$$A_i^{\rm new}(t) = f_2(A_{i-1}^{\rm old}(t) + A_{i+1}^{\rm old}(t)) \ , \tag{4.3}$$

$$F_i^{\rm new}(t) = \frac{G_{\rm low}}{G_{\rm high}} \left[f_1(A_i^{\rm old}(t) + A_{i+1}^{\rm old}(t)) + f_3(A_{i-1}^{\rm old}(t) + A_{i+2}^{\rm old}(t)) \right] \ , \tag{4.4}$$

where $G_{\rm high} = 1.3\ {\rm V/pC}$ and $G_{\rm low} = 0.3\ {\rm V/pC}$ represent the measured gain parameters of the high-gain and low-gain preamplifiers, respectively (see Section 2.2.3).

4.4.3 Noise attachment

The voltage of real waveforms has a fluctuation caused by electric noise, and its standard deviation corresponds to about $2\ {\rm ch}$. However, the electric noise of the template waveform is attenuated because the high-frequency noise was reduced during the averaging process. Therefore, a random trigger data, whose trigger rate is set at $1\ {\rm cps}$ on average, is used for reproducing the experimental condition. About 500 waveforms are acquired for all wires, and one of them are selected randomly and attached to every waveform. The typical waveform of the random trigger data is shown in Figure 4.15.

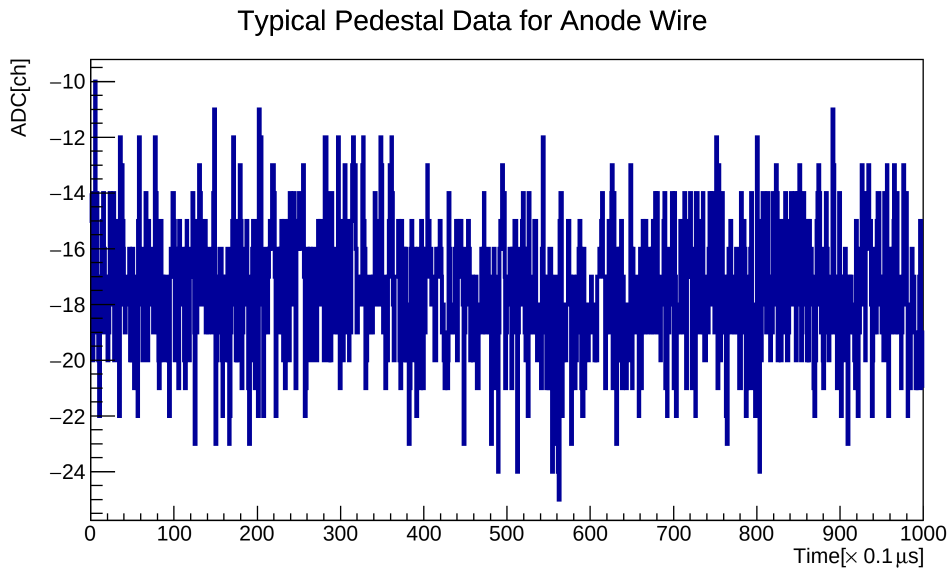

Figure 4.15: Typical waveform acquired in random trigger mode.

4.5 Diffusion

It is well known that a drifting electron diffuses vertically to the drifting direction. The diffusion process in a particular direction can be expressed as the following one-dimensional diffusion equation

$$\frac{\partial N}{\partial t} = D\frac{\partial^2 N}{\partial x^2} \quad , \tag{4.5}$$

where $N(x,t)$ represents the electron density as a function of position x and time t. If $N(x,0) = \delta(x)$ is imposed as an initial condition, the electron density is expressed as

$$N(x,t) = \frac{1}{\sqrt{4\pi Dt}} \exp\left(-\frac{x^2}{4Dt}\right) \quad . \tag{4.6}$$

We can see that the electron density has a Gaussian distribution, and its standard deviation corresponds to $\sqrt{2Dt}$. This means that the displacement by diffusion is in proportional to the square root of its drifting length. Its constant of proportionality, defined as k in this thesis, has a dimension of square root of length.

To evaluate the optimum value of k, a following parameter is defined as the sensitive index of diffusion

$$\mathrm{nearmax/main} = \frac{\mathrm{Max}\{\mathrm{AINT[maxch+1]},\ \mathrm{AINT[maxch-1]}\}}{\mathrm{AINT[maxch]}} \quad , \tag{4.7}$$

where maxch is the channel number whose AINT (defined in Section 3.1) value is the largest among all anode wires for the event. A larger value of $\mathrm{nearmax/main}$ means a larger charge sharing in anode wires. The number of large $\mathrm{nearmax/main}$ events increases when the displacement due to the diffusion increases. The simulated distribution of the parameter was compared with the experimental data in the Fe X-ray events.

Figures 4.16 shows the distribution of $\mathrm{nearmax/main}$ for experimental Fe(up) and Fe(down) data. The x-axis in Figure **??** represents the semilogarithmic distribution. The y-axis represents the event ratio to the total number of Fe events. We can see the significant increase of event ratio for Fe(down) even in the region of $0.1 \leq \mathrm{narmax/main} \leq 1$. This is because electrons produced from Fe(down) X-ray drift three times as long as the electrons from Fe(up) X-ray (see Section 3.3). The longer drift length means larger displacement by diffusion, which results in the increase of $\mathrm{nearmax/main}$.

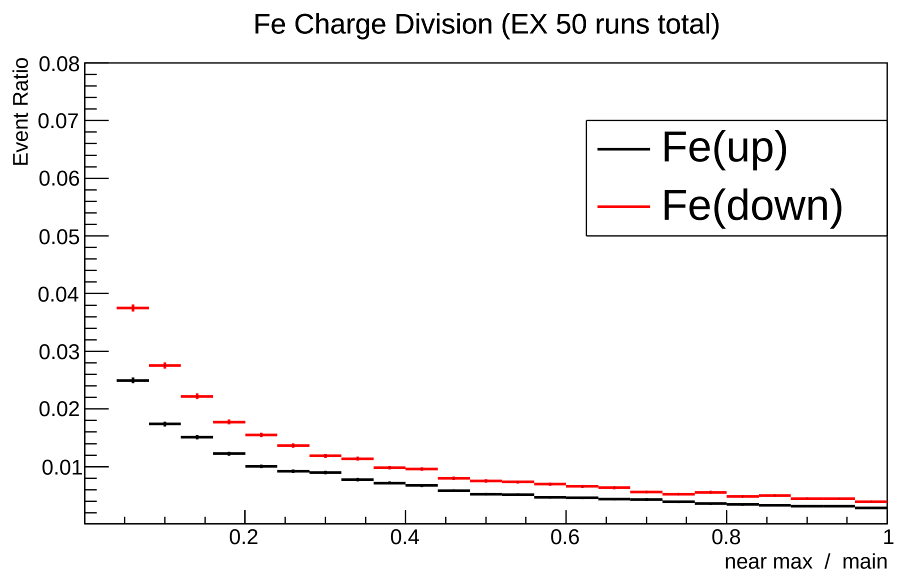

Figure 4.16: Distribution of $\mathrm{nearmax/main}$ for Fe(up) and Fe(down) experimental data.

Figures 4.17 and 4.18 shows the distribution of simulation with different k values. The integral value in the $0.1 \leq \mathrm{narmax/main} \leq 1$ region was used for the comparison. Figures 4.19 and 4.20 show the integral difference (simulation - experiment) in this region for both Fe(up) and Fe(down) data. The optimum k value can be determined as the one which gives no difference between the integral of the simulation and the experimental data, which is the value of the horizontal axis when the value of the vertical axis is zero. By fitting a straight line to the difference of the integral, the best value is evaluated as $k = 0.068 \pm 0.002\ \mathrm{mm}^{1/2}$ from Fe(up) and $k = 0.065 \pm 0.001\ \mathrm{mm}^{1/2}$ from Fe(down), respectively. The results are consistent with each other within their statistical uncertainties, and we finally adopted the average of the two values, i.e. $k = 0.066\ \mathrm{mm}^{1/2}$ as the input parameter for the diffuse simulation. The simulated distribution with this value is shown in Figure 4.21. Note that there is a significant difference in the pedestal region ($10^{-3} < \mathrm{nearmax/main} < 5 \times 10^{-2}$) because of the simulation problem, which is not expected to affect the result of this analysis.

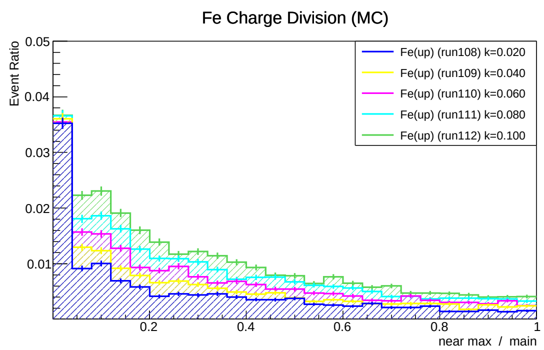

Figure 4.17: Simulated $\mathrm{nearmax/main}$ distribution for Fe(up).

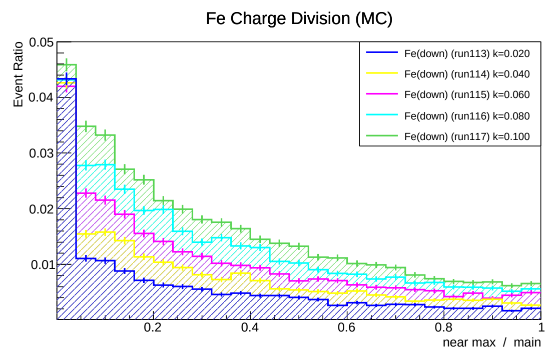

Figure 4.18: Simulated $\mathrm{nearmax/main}$ distribution for Fe(down).

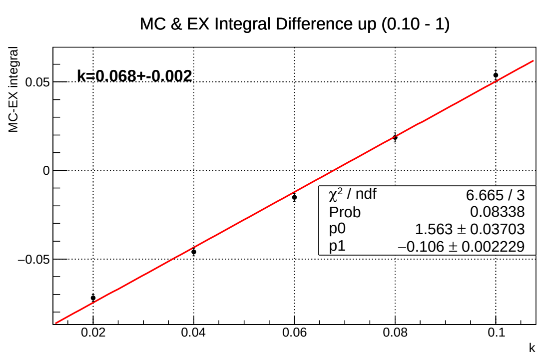

Figure 4.19: Integral difference (MC(up)-EX(up)) at $0.1 \leq \mathrm{nearmax/main} \leq 1$ region.

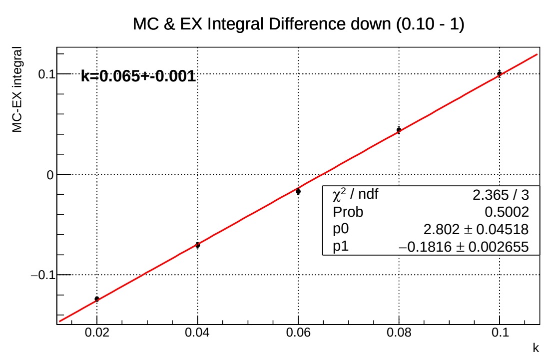

Figure 4.20: Integral difference (MC(down)-EX(down)) at $0.1 \leq \mathrm{nearmax/main} \leq 1$ region.

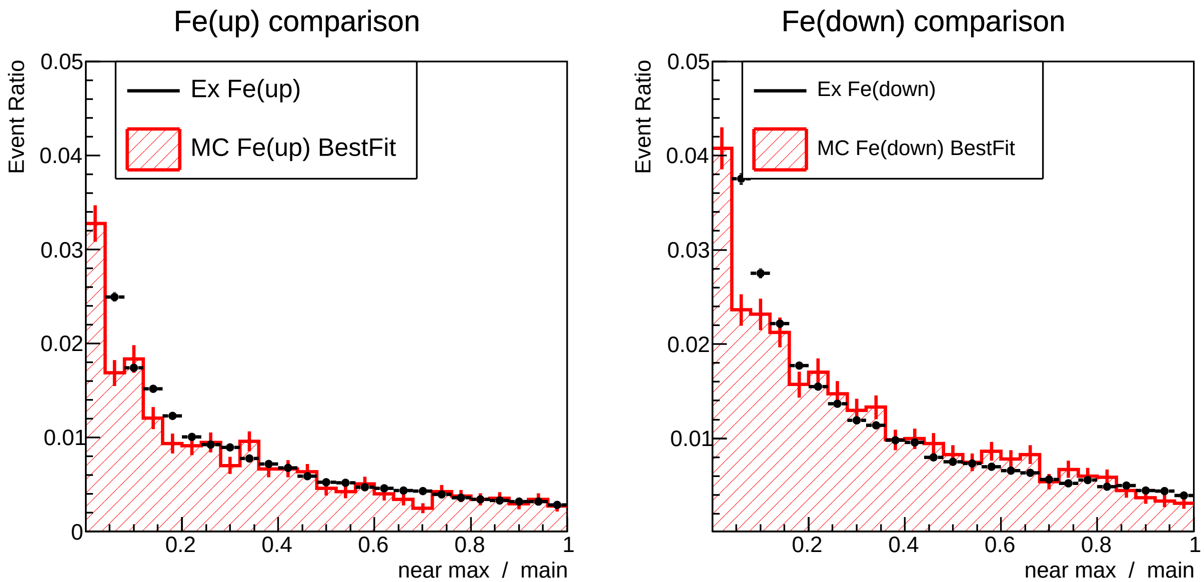

Figure 4.21: Comparison of experimental data and best-fit ($k = 0.066$) simulation; Fe(up) mode (left) and Fe(down) mode (right).

The transverse diffusion coefficients of an electron in the variety kinds of gases were calculated using Magboltz software [28]. Figure 4.22 shows the diffusion coefficients in the mixture of the $90\ \mathrm{kPa}\ \mathrm{He}$ and the $10\ \mathrm{kPa}\ \mathrm{CO_2}$ gases at $300\ \mathrm{K}$. The red lines in the figure show the real electric field in the TPC and the diffusion coefficient corresponding to the evaluated parameter ($k = 0.066\ \mathrm{mm}^{1/2}$). There is a good agreement between the intersection of the lines and the red points (transverse diffusion coefficients without the magnetic field), which demonstrates the validity of the method to evaluate the diffusion parameter.

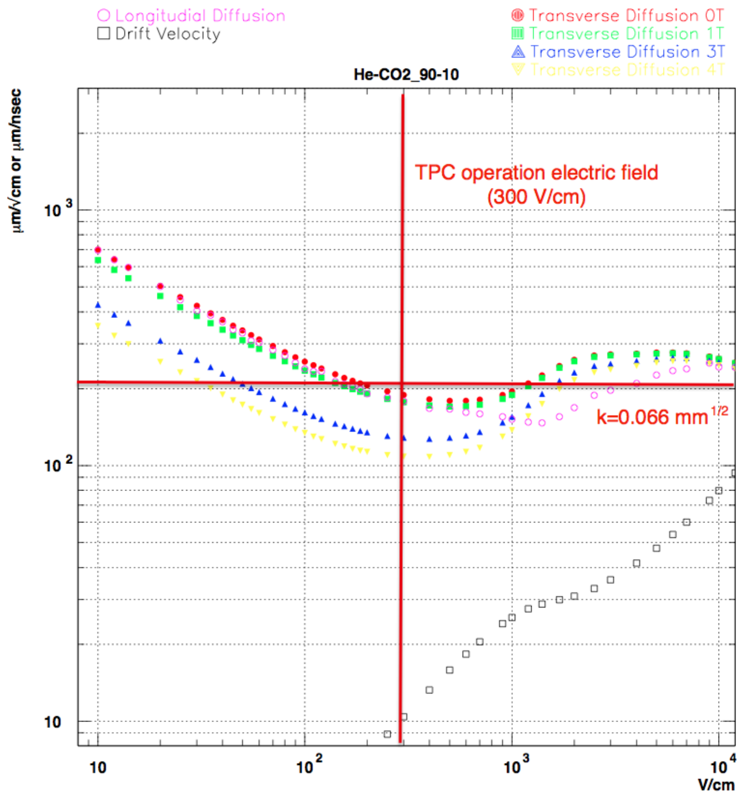

Figure 4.22: Transverse diffusion coefficients in the mixture of the $90\ \mathrm{kPa}$ He and the $10\ \mathrm{kPa}$ $\mathrm{CO_2}$ gases [28]. The red points represent the transverse diffusion coefficients without the magnetic field.

4.6 Comparison of simulated distribution and experimental distribution

The development of the Monte Carlo simulation allows the comparison of distribution of several parameters between the simulation and experimental data. Following figures (Figure 4.23 $\sim$ 4.26) compare the distribution of several parameters which is important for the analysis. Note that the experimental distribution contains not only the signal events (S_β and $S_{^3\mathrm{He}}$) but also several kinds of backgrounds, such as $B^{\mathrm{int}\gamma}$ and B^{scat}.

The discrepancy in the ASUM distribution (Figure 4.23) is assumed to come from the pulse deformation observed for a large deposit wire (see Figure 4.27). The deformation seems to increase the reconstructed deposit energy, i.e. ASUM, for the $^3\mathrm{He}(n,\ p)^3\mathrm{H}$ events. The significant difference in the FPH_MAX distribution (Figure 4.24) comes from the uncertainty of the space charge effect, which is discussed in Section 5.2.4. The reason of the structure difference in the ADTIME ~ 20 distribution (Figure 4.25) is not yet understood. The excess of the experimental data in the ADC distribution (Figure 4.26) is assumed to come from $B^{\mathrm{int}\gamma}$ and B^{scat}.

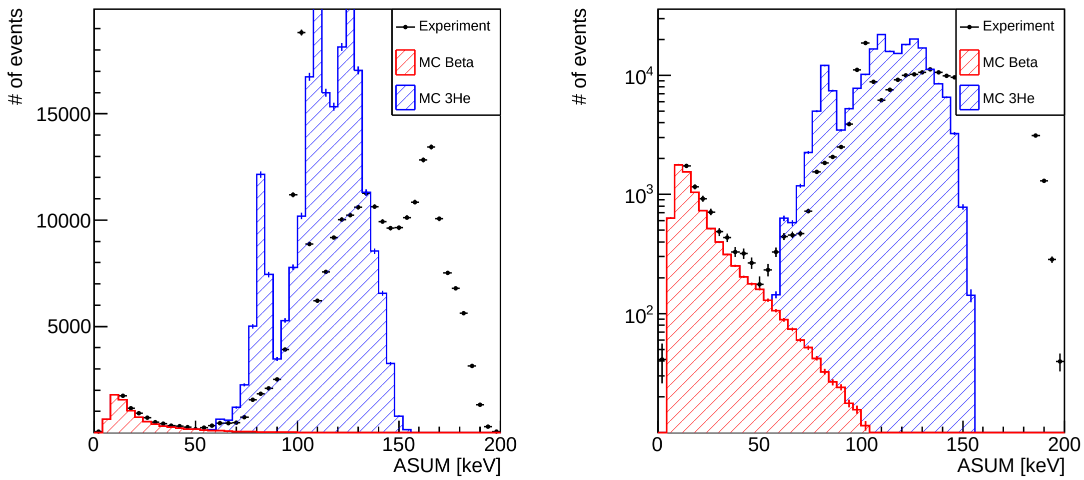

Figure 4.23: Comparison of the ASUM distribution between the simulation and the experimental data; linear scale (left) and semilogarithmic scale (right)

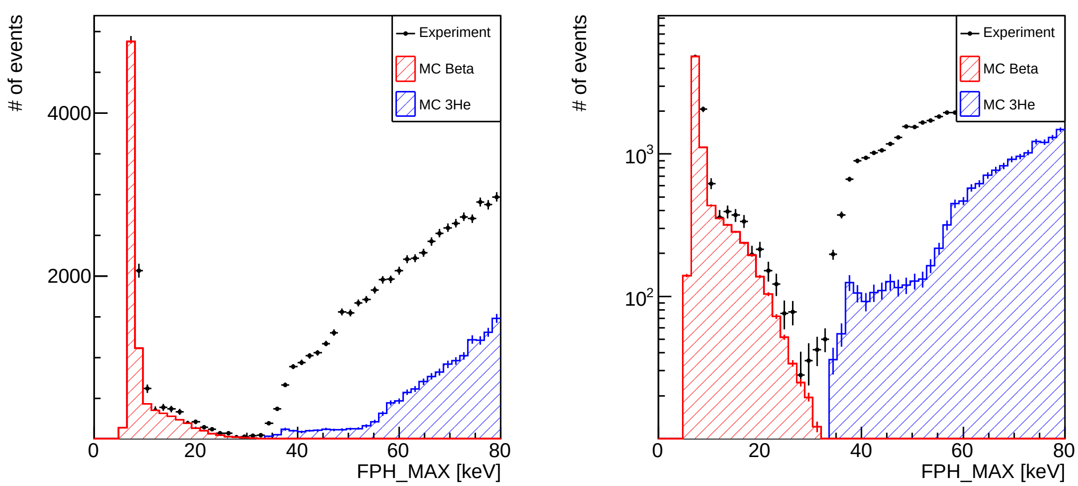

Figure 4.24: Comparison of the FPH_MAX distribution between the simulation and the experimental data; linear scale (left) and semilogarithmic scale (right).

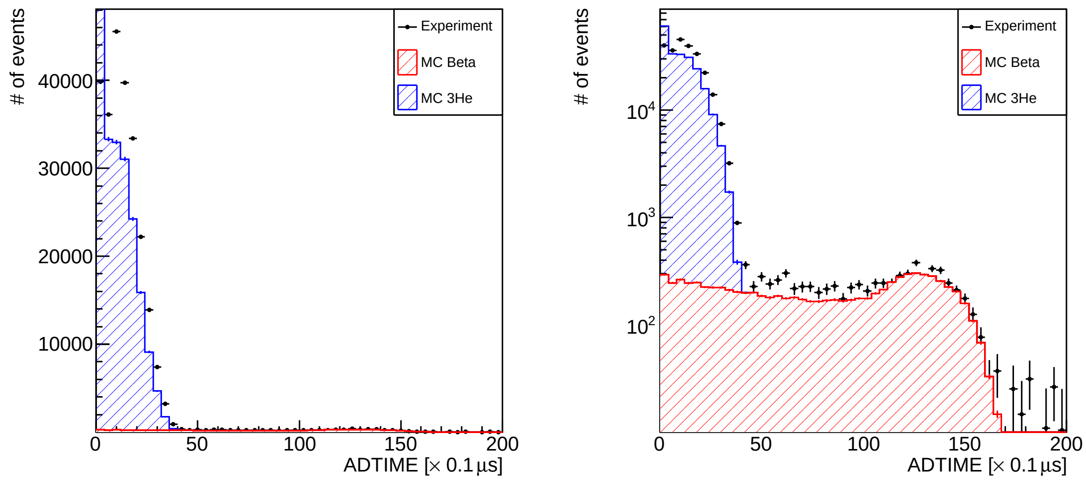

Figure 4.25: Comparison of the ADTIME distribution between the simulation and the experimental data; linear scale (left) and semilogarithmic scale (right).

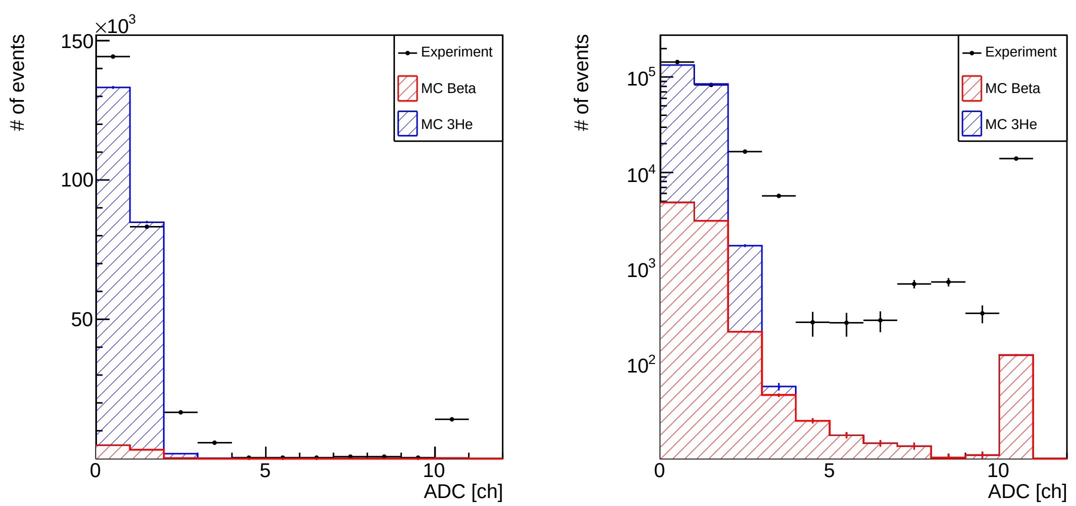

Figure 4.26: Comparison of the ADC distribution between the simulation and the experimental data; linear scale (left) and semilogarithmic scale (right)

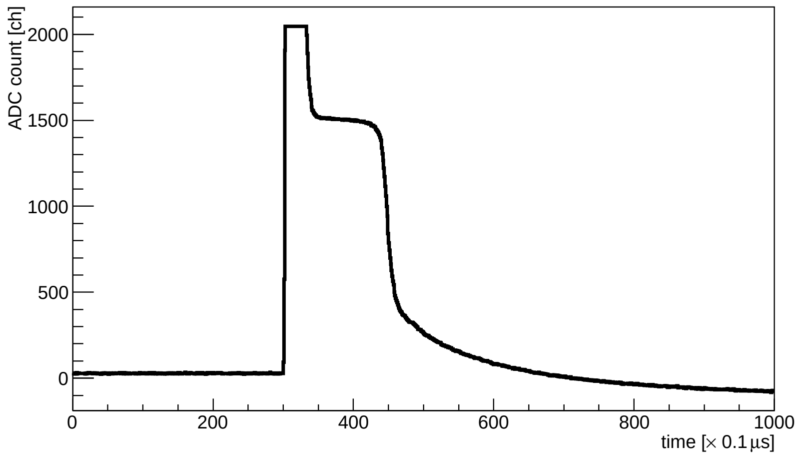

Figure 4.27: Pulse deformation for a large-deposit wire.

Chapter 5

Analysis

This chapter describes the analysis to evaluate the amount of correction and uncertainties for several topics.

5.1 Correction for a $^{17}\mathrm{O}(n,\ \alpha)^{14}\mathrm{C}$ process

As described in Section 3.5.1, a neutron causes a $^{17}\mathrm{O}(n,\ \alpha)^{14}\mathrm{C}$ process in the TPC, which can be background for $^{3}\mathrm{He}(n,\ p)^{3}\mathrm{H}$. Since the TPC does not have an energy resolution to distinguish the two kinds of events, the number of the background events needs to be subtracted from that of $^{3}\mathrm{He}(n,\ p)^{3}\mathrm{H}$ events. In this section, an evidence for the existence of $^{17}\mathrm{O}(n,\ \alpha)^{14}\mathrm{C}$ events and its correction amount are discussed.

5.1.1 Process

As the TPC contains $\mathrm{CO_2}$ gas inside, $^{17}\mathrm{O}$ atoms are expected to be in the TPC. It is known that a $^{17}\mathrm{O}$ atom causes the following interaction with a free neutron

$$n +^{17}\mathrm{O} \rightarrow \alpha +^{14}\mathrm{C} + 1818\ \mathrm{keV}\ \ . \tag{5.1}$$

Since this process is a two-body decay, the kinetic energy of each decayed nucleus is monochromatic, $1414\ \mathrm{keV}$ and $404\ \mathrm{keV}$ for α and $^{14}\mathrm{C}$, respectively. The cross section is $0.235 \pm 0.010\ \mathrm{barn}$ according to the Table of Isotope [20]. The time structure of the $^{17}\mathrm{O}(n,\ \alpha)^{14}\mathrm{C}$ events is the same as that of $^{3}\mathrm{He}(n,\ p)^{3}\mathrm{H}$ events.

5.1.2 Energy distribution

The TPC operates with comparatively high multiplication factor, namely, under the region called limited proportionality. It results in the bad energy resolution for the $^{3}\mathrm{He}(n,\ p)^{3}\mathrm{H}$ and $^{17}\mathrm{O}(n,\ \alpha)^{14}\mathrm{C}$ events, hence the two kinds of events cannot be separated in the distiributionof the total energy deposit, or ASUM (defined in Section 3.1) distribution. The ASUM distribution with the FiducialTimeCut (defined in Section 3.2) is shown in Figure 5.1, and no peaks originating from the

^{3}He$(n,\ p)^3$H and ^{17}O$(n,\ \alpha)^{14}$C events are observed. This prevents us from proving the evidence of the ^{17}O$(n,\ \alpha)^{14}$C events in the TPC. In order to resolve this problem, we acquired the data during which the applied voltage to anode wires was reduced from usual 1720 V to 1200 V. It reduces the multiplication factor in the TPC, hence the tow kinds of events can be separated in the ASUM distribution.

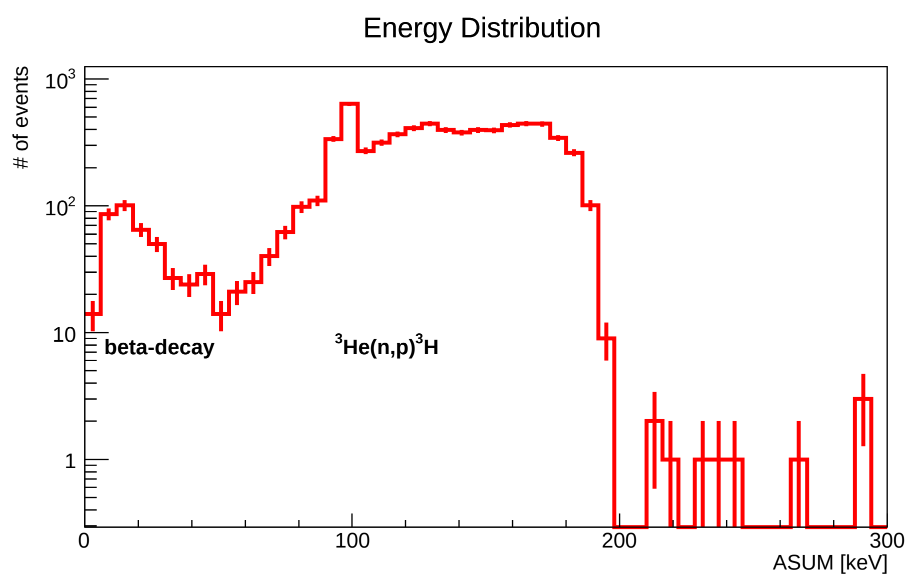

Figure 5.1: Typical deposit energy distribution in the TPC in normal-voltage mode.

Figure 5.2 shows the ASUM (defined in Section 3.1) after the FiducialTimeCut. Note that the beta-decay events does not appear in Figure 5.2 because most of the beta-decay events do not satisfy the DAQ trigger condition in the low-voltage mode. The low-energy peak is assumed to be a ^{3}He$(n,\ p)^3$H (Q value is 764 keV). On the other hand, there are completely different two kinds of events in the high-energy peak. Several events have double tracks, whereas others have a single track. Typical two-dimensional event displays for the two kinds of events are shown in Figures 5.3 and 5.4.

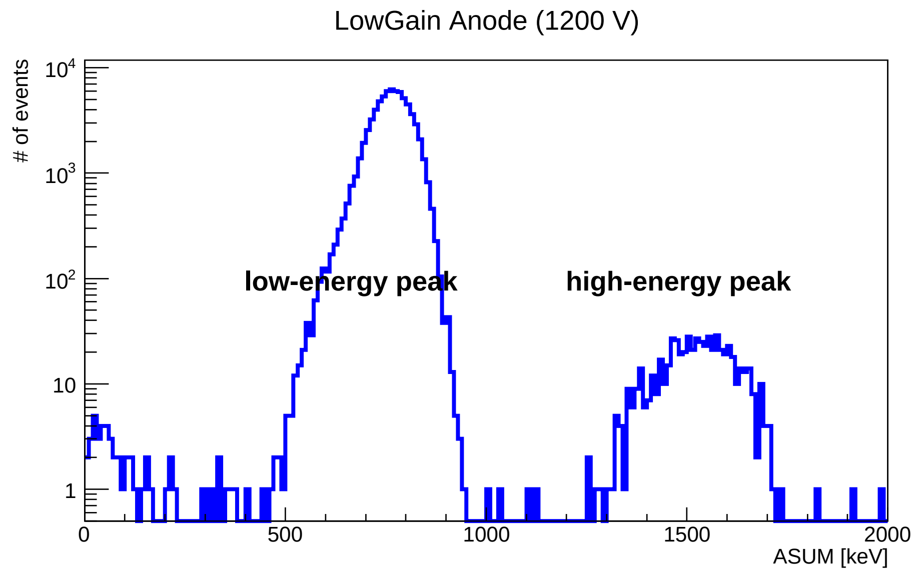

Figure 5.2: Typical deposit energy distribution in the TPC in low-voltage mode.

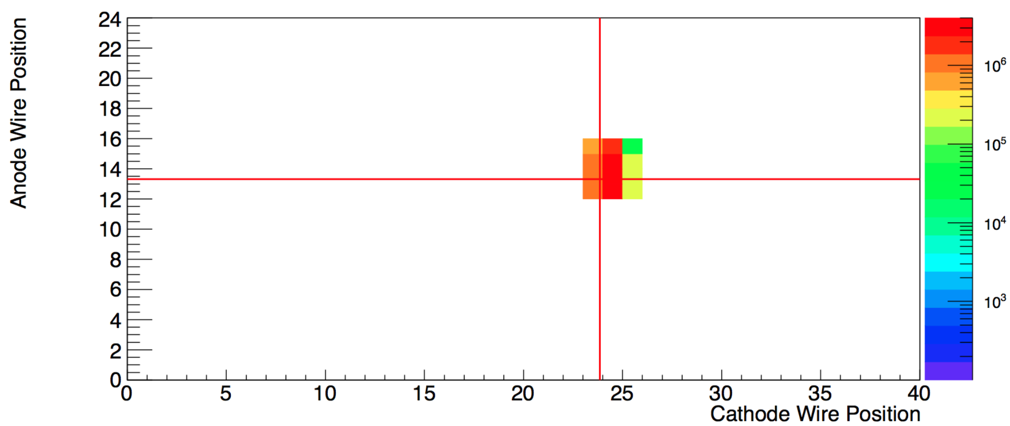

Figure 5.3: Event display for single-track event.

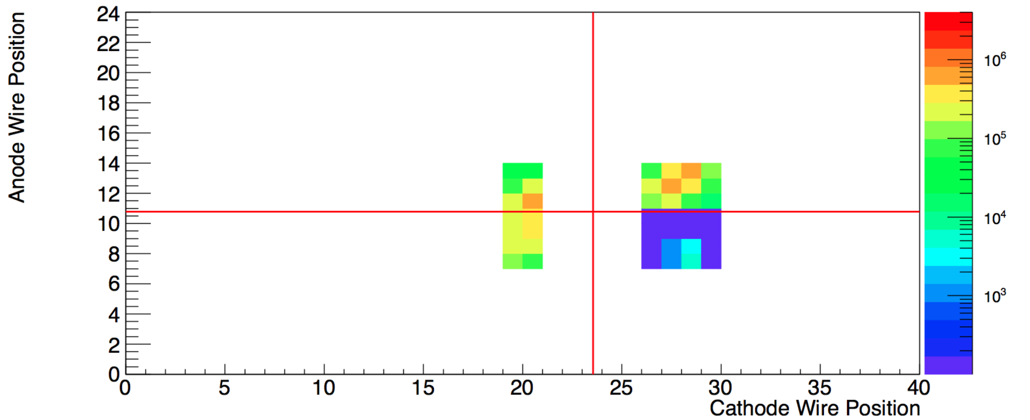

Figure 5.4: Event display for double-track event.

The double-tracks events (Figure 5.4) are assumed to be the pileup of $^3\mathrm{He}(n,\ p)^3\mathrm{H}$ events because the ASUM value is just twice as large as that of the low-energy peak. On the other hand, the single-track events are assumed to be the $^{17}\mathrm{O}(n,\ \alpha)^{14}\mathrm{C}$ (Q value is $1818\ \mathrm{keV}$) events, although the deposit energy seems to be lower than expected. The reason seems to be the reduction of the multiplication factor for $^{17}\mathrm{O}(n,\ \alpha)^{14}\mathrm{C}$ due to the space charge effect to be discussed in Section 5.2.3.

5.1.3 TOF structure

For the two kinds of events in the high-energy preak, the TOF (Time Of Flight) structure in the TPC is investigated. Figure 5.5 shows the TOF and z position correlation for the two kinds of events. The z position is represented by CHCE parameter (defined in Section 3.1). The clear time structure can be seen for two kinds of events. It is almost same as the structure of neutrons formed by the Spin Flip Chopper (see Figure 3.3), which signifies that both the two kinds of events are caused by neutrons, and it is consistent with our expectation. Several single-track events exist in the sideband time, which are expected to be caused by natural radiation.

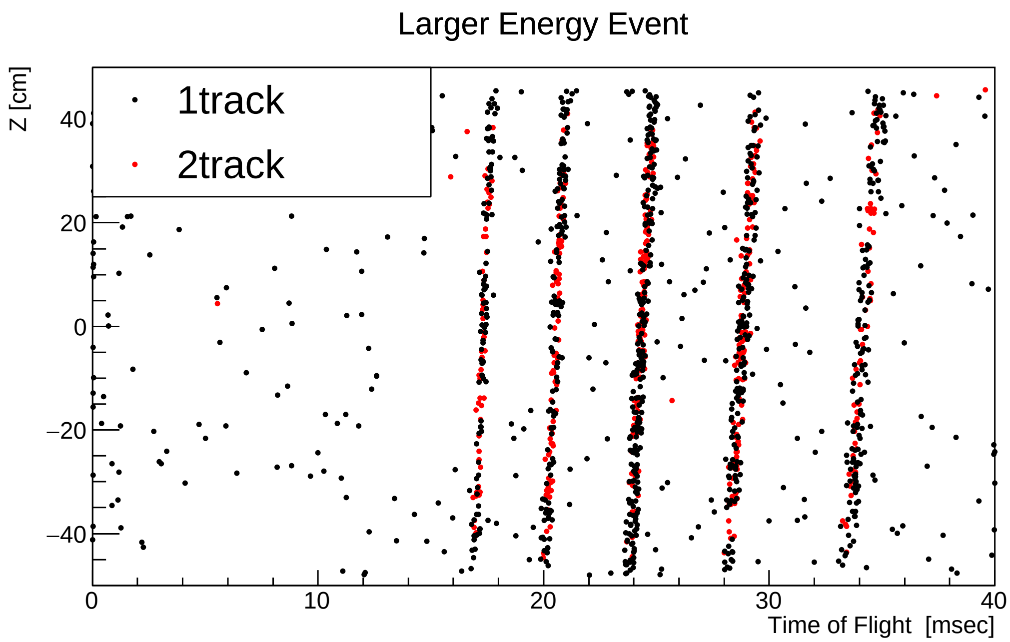

Figure 5.5: TOF and z position correlation for the high-energy events in Figure 5.2.

5.1.4 Event rate

The three kinds of events (low-energy events, single-track events in the high-energy peak, and double tracks events in the high-energy peak) are counted for three kinds of gas conditions, which are listed in Table 5.1. Note that the background events in the high-energy peak is counted in the sideband time. The number of background events is scaled to the time width of the fiducial time.

Gas#	^{3}He press.	CO_2 press.	Fiducial Time	low-energy peak	high-energy peak			
					sum	2 track	1 track	background
42	100.5 mPa	14.9 kPa	1946 s	74225	613	249	364	17.4
47	135.9 mPa	7.5 kPa	848 s	45991	317	211	106	4.7
49	7.72 mPa	15.1 kPa	225 s	618	54	0	54	2.0

Table 5.1: Number of detected events after the FiducialTimeCut in low-voltage mode for several gas conditions.

In order to verify the existence of $^{17}\mathrm{O}(n,\ \alpha)^{14}\mathrm{C}$ events, the number of detected events are compared with the expected numbers of the events. The expected number of double-track (pile-up) events can be derived based on the $^3\mathrm{He}(n,\ p)^3\mathrm{H}$ (low-energy peak) events. It is calculated for the

Gas 42 as

$$
\begin{aligned}
N^{\mathrm{expected}}_{\mathrm{double-track}}(\mathrm{Gas42}) &= \left(\frac{N_{^3\mathrm{He}}}{\mathrm{Fiducial\ Time}}\right)^2 \times \mathrm{Fiducial\ Time} \times \mathrm{WIDTH}\ , &(5.2)\\
&= \left(\frac{74225}{1946\ \mathrm{s}}\right)^2 \times 1946\ \mathrm{s} \times 10^{-4}\ \mathrm{s}\ , &(5.3)\\
&= 282, &(5.4)
\end{aligned}
$$

where WIDTH (=10^{-4} s) represents the DAQ time width for a trigger signal. The number of single-track ($^{17}\mathrm{O}(n,\ \alpha)^{14}\mathrm{C}$) events can be derived based on the number of $^3\mathrm{He}(n,\ p)^3\mathrm{H}$ (low-energy) events and the abundance of ^{17}O in the TPC. The "pressure" of ^{17}O atoms can be calculated assuming the natural abundance of oxygen, i.e. $0.038 \pm 0.001\%$ according to IUPAC technical report [29]. On the basis of this abundance, the "pressure" of ^{17}O atoms in Gas 42 is calculated as

$$
P_{^{17}\mathrm{O}} = P_{\mathrm{CO_2}} \times 0.00038 \times 2 = 15\ \mathrm{kPa} \times 0.00038 \times 2 = 11.5 \pm 0.3\ \mathrm{Pa}\ . \tag{5.5}
$$

Based on $P_{^{17}\mathrm{O}}$, the expected number of $^{17}\mathrm{O}(n,\ \alpha)^{14}\mathrm{C}$ events in the TPC can be determined as

$$
\begin{aligned}
N^{\mathrm{expected}}_{\mathrm{single-track}}(\mathrm{Gas42}) &= N_{^3\mathrm{He}} \times \frac{P_{^{17}\mathrm{O}} \times \sigma_{^{17}\mathrm{O}}}{P_{^3\mathrm{He}} \times \sigma_{^3\mathrm{He}}}\ , &(5.6)\\
&= 74225 \times \frac{11.5\ \mathrm{Pa} \times 0.235\ \mathrm{barn}}{0.1005\ \mathrm{Pa} \times 5333\ \mathrm{barn}}\ , &(5.7)\\
&= 362. &(5.8)
\end{aligned}
$$

The expectation and the counted numbers of events are compared in Table 5.2. The result shows that the numbers of detected events are well concordant with the expected numbers for three different gas conditions. No two-track events are observed in the Gas 49 data because the ^{3}He pressure of Gas 49 is very low. These results in Table 5.2 clearly signify the existence of both $^3\mathrm{He}(n,\ p)^3\mathrm{H}$ pile-up events and the $^{17}\mathrm{O}(n,\ \alpha)^{14}\mathrm{C}$ events in the TPC. The existence of the $^{17}\mathrm{O}(n,\ \alpha)^{14}\mathrm{C}$ events means the overestimation of the number of $^3\mathrm{He}(n,\ p)^3\mathrm{H}$ events, which requires the correction to the neutron lifetime. The correction amount $\delta_{^{17}\mathrm{O}}$ for Gas 42 is derived using the event ratio of $^3\mathrm{He}(n,\ p)^3\mathrm{H}$ and $^{17}\mathrm{O}(n,\ \alpha)^{14}\mathrm{C}$ as

$$
\begin{aligned}
\delta_{^{17}\mathrm{O}} &= -\frac{P_{^{17}\mathrm{O}} \times \sigma_{^{17}\mathrm{O}}}{P_{^3\mathrm{He}} \times \sigma_{^3\mathrm{He}}}\ , &(5.9)\\
&= -\frac{11.5\ \mathrm{Pa} \times 0.235\ \mathrm{barn}}{0.1005\ \mathrm{Pa} \times 5333\ \mathrm{barn}}\ , &(5.10)\\
&= -0.50 \pm 0.03\ \%. &(5.11)
\end{aligned}
$$

The uncertainty mainly comes from that of the cross section of a $^{17}\mathrm{O}(n,\ \alpha)^{14}\mathrm{C}$ process (0.235 ± 0.010 barn).

Gas#	low-energy peak	high-energy peak: 2 track		high-energy peak: 1 track	
	detected	expected	detected	expected	detected
42	74225	282	249	374	364
47	45991	249	211	85	106
49	618	0.170	0	40	54

Table 5.2: Number of events in low voltage mode for several gas conditions.

5.2 Separation of the signal events

In this experiment, the absolute numbers of both beta-decay and $^3\mathrm{He}(n,\ p)^3\mathrm{H}$ events are required in order to evaluate the neutron lifetime (see Section 1.4). Since both beta-decay and the $^3\mathrm{He}(n,\ p)^3\mathrm{H}$ are caused by a neutron, there is no difference in the time structure. In this section, the method and relevant uncertainties for the separation of the two kinds of events are discussed.

5.2.1 Method of separation

The $^3\mathrm{He}(n,\ p)^3\mathrm{H}$ and beta-decay events need to be separated based on how the energy loss processes are in the TPC because there is no difference in the time structure. An electron from beta-decay has the continuous energy distribution (Q value is $782\ \mathrm{keV}$), whereas the deposit energy for $^3\mathrm{He}(n,\ p)^3\mathrm{H}$ is monochromatic energy of $764\ \mathrm{keV}$. The ASUM parameter (defined in Section 3.1) was adopted so far for the separation parameter. Figure 5.6 shows the ASUM distribution for the two kinds of events. Although it seems like we can make a cut at around $50\ \mathrm{keV}$, the two kinds of events cannot be separated completely. One reason is that the pulse height of the $^3\mathrm{He}(n,\ p)^3\mathrm{H}$ event exceeds the DAQ dynamic range ($\sim 2\ \mathrm{V}$) in anode wires, which reduces the ASUM value. Such an excess of the pulse height is not observed in the field wire because it is connected to the low-gain preamplifiers. Therefore, the energy resolution, i.e. separation capability, is expected to improve in the field wire.

In addition, the quantitative index of the energy loss process is also useful for the separation because it is completely different between the beta-decay and $^3\mathrm{He}(n,\ p)^3\mathrm{H}$ events. Whereas the ions produced from $^3\mathrm{He}(n,\ p)^3\mathrm{H}$ lose their energy locally, the electron produced from beta-decay loses little energy during its flight and have long range in the TPC. Therefore, a parameter describing how localized the deposit energy is in the TPC should be a useful parameter. The maximum pulse height among all wires is a good choice for this purpose.

Based on the above considerations, the FPH_MAX parameter (defined in Section 3.1) is proposed as the separation parameter of the beta-decay and the $^3\mathrm{He}(n,\ p)^3\mathrm{H}$ events. Figure 5.7 shows the FPH_MAX distribution for neutron events. It can be seen that the separation capability of the two kinds of events improves in the FPH_MAX distribution. Therefore, the correction and uncertainty relevant to the separation are expected to decrease in comparison with those using the ASUM.

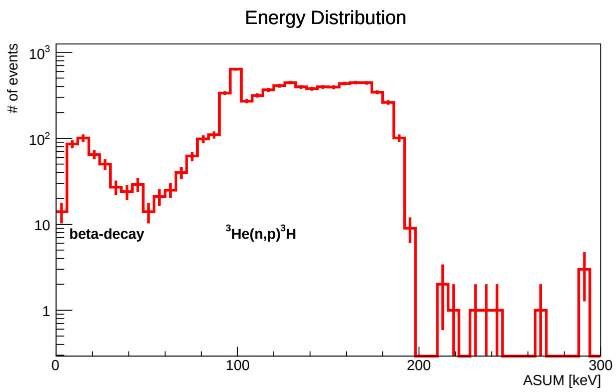

Figure 5.6: ASUM distribution for neutron events.

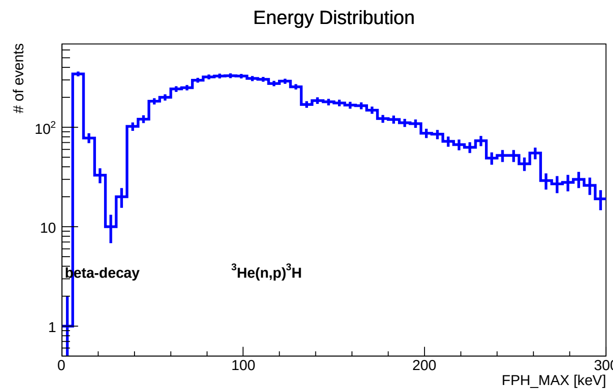

Figure 5.7: FPH_MAX distribution for neutron events.

Although we can see a cut position at approximately $30\ \mathrm{keV}$ in Figure 5.7, the two kinds of events are still not completely separated. The efficiencies of both events at a certain cut position is estimated using the Monte Carlo simulation (see Section 4) to reproduce the FPH_MAX distribution of both $^3\mathrm{He}(n,\ p)^3\mathrm{H}$ and the beta-decay events.

5.2.2 Scattered event

Several atoms in the TPC gas cause scattering and absorbing processes for a neutron. Their cross sections and probabilities are listed in Tables 5.3 [12] and 5.4, respectively. Note that the scattering processes do not take an interference of the molecular structure into account.

Table 5.3: Cross section for several atoms used in the TPC [7, 29].

atom	natural abundance	scattering cross section [barn]	absorption cross section for a 2200 $\mathrm{m/s}$ neutron [barn]
^{3}He	0.000134(3)	6	5333(7)
^{4}He	99.999866(3)	1.34	0
^{12}C	98.93(8)	5.559	0.00353(7)
^{13}C	1.07(8)	4.84	0.00137(4)
^{16}O	99.757(16)	4.232	0.000190(19)
^{17}O	0.038(1)	4.2	0.235(10)
^{18}O	0.205(14)	4.29	0.00016(1)

Table 5.4: Cross sections for the TPC gas composition.

molecular	pressure[kPa]	scattering probability	absorption probability for a 2200 $\mathrm{m/s}$ neutron
^{3}He	100 mPa	1.4×10^{-8}	1.3×10^{-5}
^{4}He	85 kPa	2.7×10^{-3}	0
CO_2	15 kPa	5.0×10^{-3}	1.4×10^{-6}

A scattered neutron causes the $^3\mathrm{He}(n,\ p)^3\mathrm{H}$ event near the TPC wall at a certain probability, and only a part of total deposit energy is detected in the TPC. Such an event can have the lower energy than usual, hence it might be one of the candidates of the leakage events for beta-decay. To estimate the scattering processes, the $^3\mathrm{He}(n,\ p)^3\mathrm{H}$ distribution caused by scattered neutrons is simulated as described in Section 4.1.1.

Figure 5.8 shows the $^3\mathrm{He}(n,\ p)^3\mathrm{H}$ distribution for on-axis (caused by a non-scattered neutron) event and off-axis (caused by a scattered neutron) event. A FCE parameter (defined in Section 3.1) represents the reaction point of the $^3\mathrm{He}(n,\ p)^3\mathrm{H}$ event. It is possible to estimate the ratio of on-axis and off-axis $^3\mathrm{He}(n,\ p)^3\mathrm{H}$ events by comparing simulated FCE distribution with the experimental data as shown in Figure 5.9. Figure 5.9 shows the $^3\mathrm{He}(n,\ p)^3\mathrm{H}$ FCE distribution of both experimental data and adjusted simulation. The adjustment signifies that the ratio of on-axis $^3\mathrm{He}(n,\ p)^3\mathrm{H}$ to off-axis $^3\mathrm{He}(n,\ p)^3\mathrm{H}$ is 363.

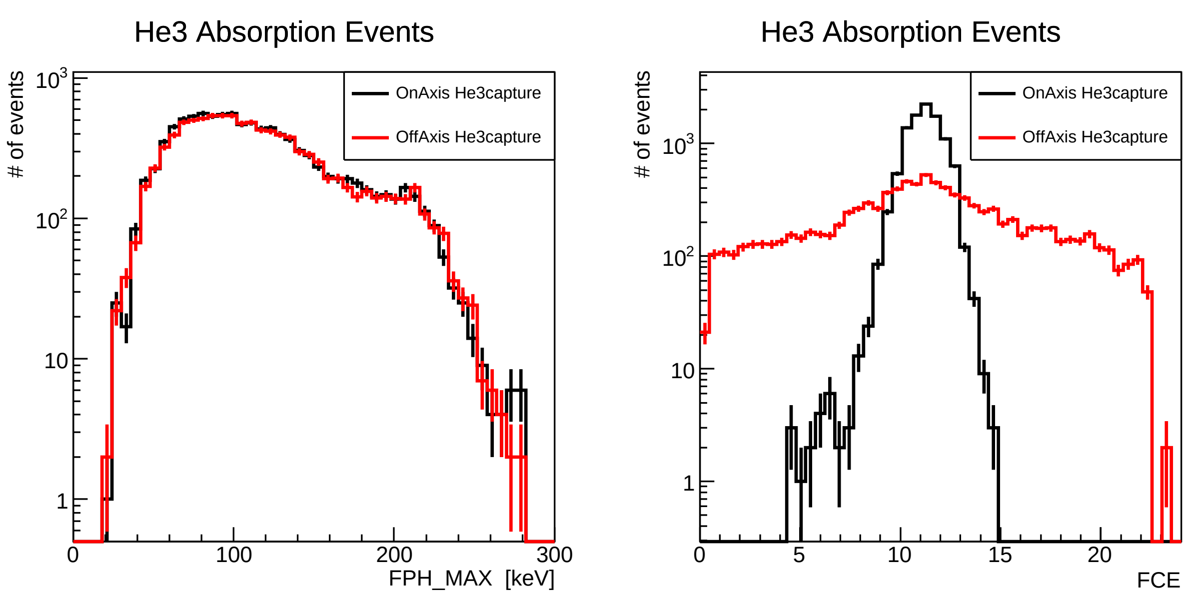

Figure 5.8: Comparison of the on-axis and off-axis $^3\mathrm{He}(n,\ p)^3\mathrm{H}$ distribution in the Monte Carlo simulation.

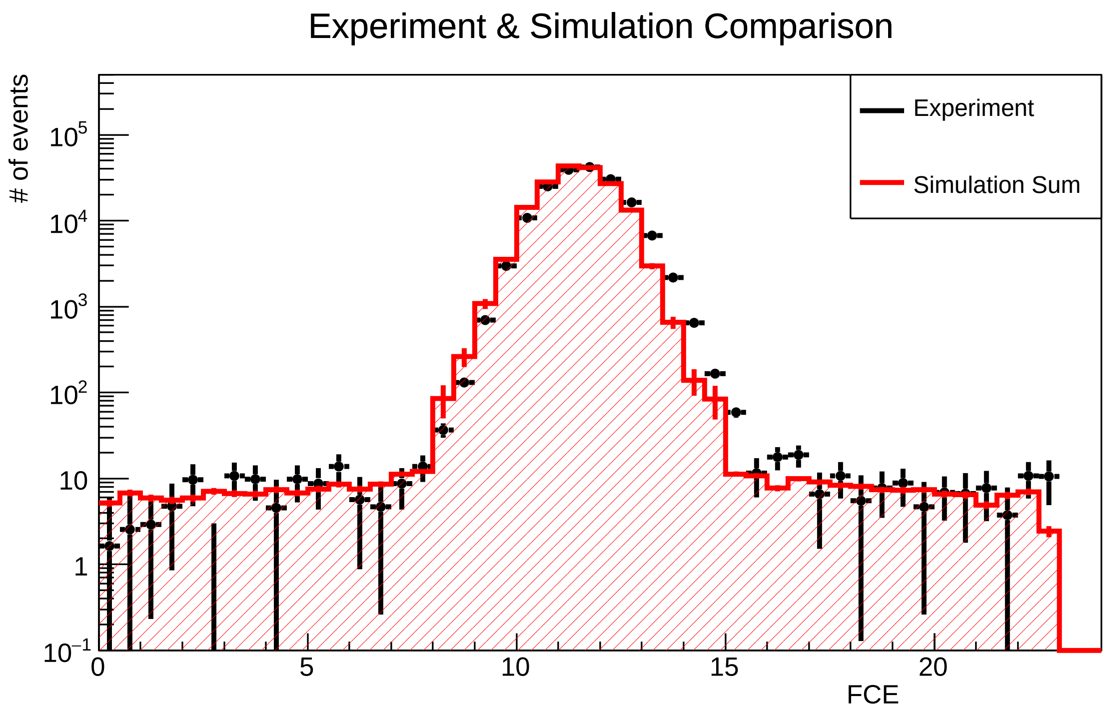

Figure 5.9: Comparison of the simulated and experimental FCE distribution.

5.2.3 Space charge effect

It is well known that an avalanche multiplication factor in a gas chamber decreases when there is a localized large energy deposit. This is because a lot of ions produced by avalanche multiplication reduce the electric field near an anode wire. The phenomenon is called a space charge effect. In this experiment, the multiplication factor is comparatively high (the region of limited proportionality) because a low-energy electron from beta-decay needs to be detected in the TPC. For the $^3\mathrm{He}(n,\ p)^3\mathrm{H}$ process, the density of electrons from the ionization is high enough to reduce the multiplication factor.

A quantitative estimation of the space charge effect is previously investigated [30]. Here, a saturation factor s, which represents how the multiplication factor decreases at an anode wire, is estimated by comparing the reconstructed energy of an α-ray from an ^{241}Am source with the corresponding simulation results. The parameter is formulated as

$$s = \frac{\log(1 + f(\phi)\Delta E G_0)}{f(\phi)\Delta E G_0} \ , \tag{5.12}$$

where ΔE is the energy deposit at the wire, G_0 is the multiplication factor without space charge effect, and $f(\phi)$ is a factor determining the scale of the space charge effect. The parameter ϕ ($0^\circ < \phi < 90^\circ$) represents the angle between a particle track and a perpendicular line with respect to an anode wire in a two-dimensional plane as shown in Figure 5.10. The range for s is 0 to 1, and a lower value of s represents high saturation (large reduction in multiplication factor) for the event. From Figure 5.11, we can see the good agreement between the measured saturation factors for an α ray and the predicted values. Furthermore, $f(\phi)$ value was measured at several angles using collimated α-rays from a $^{241}\mathrm{Am}$ source.

$$f((0 \pm 2)^\circ) = (1.39 \pm 0.06) \times 10^{-3}\ \mathrm{MeV}^{-1}\ , \tag{5.13}$$
$$f((42 \pm 4)^\circ) = (4.5 \pm 0.3) \times 10^{-4}\ \mathrm{MeV}^{-1}\ , \tag{5.14}$$
$$f((83 \pm 2)^\circ) = (3.9 \pm 0.8) \times 10^{-5}\ \mathrm{MeV}^{-1}\ . \tag{5.15}$$

Since the electron density decreases with the increase of angle (ϕ), the parameter $f(\phi)$ is a monotone decreasing function for ϕ.

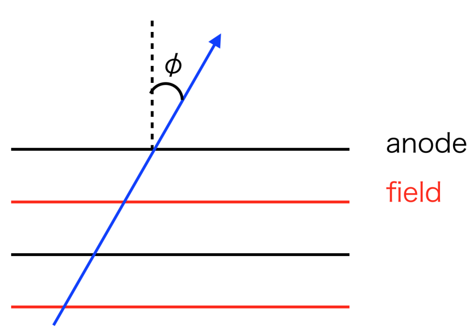

Figure 5.10: Geometrical relationship between a track path and anode wires.

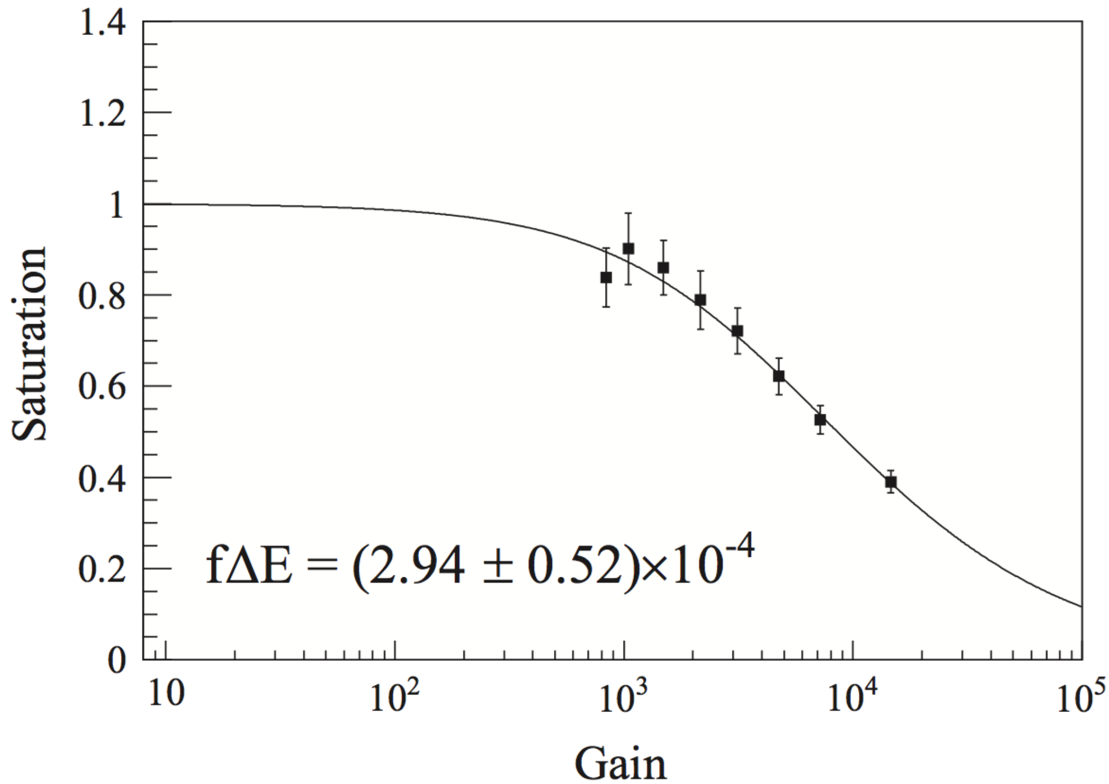

Figure 5.11: Gain reduction factor for an α ray [16, 30]. The curve represents the value predicted by the model, while the points represent the measured values.

In the theory, the dependence of track direction is expressed as the parameter $f(\phi)$ term. On the other hand, it is natural that the saturation parameter must be a function of deposit density per wire length, not a function of a track direction. According to this assumption, the modeling of Eq. (5.12) is extended as

$$s = \frac{\log\left(1 + f'\dfrac{d(\Delta E)}{dl}G_0\right)}{f'\dfrac{d(\Delta E)}{dl}G_0} \quad , \tag{5.16}$$

where $\frac{d\Delta E}{dl}$ is the deposit energy density per wire length, and f' is a newly defined scale factor. As the angle information is already contained in the $\frac{d\Delta E}{dl}$ term, f' has no angle dependence. From Eq. (5.12) and (5.16), f' must satisfy the following condition

$$f'\frac{d(\Delta E)}{dl} = f(\phi)\Delta E \quad . \tag{5.17}$$

The scale factor f' can be determined using the result of previous research ($f(42^\circ) = 4.5 \times 10^{-4}\ \mathrm{MeV}^{-1}$) as

$$f' \times \frac{\Delta E}{12\ \mathrm{mm}} = f(42^\circ) \times \Delta E = 4.5 \times 10^{-4}\ \mathrm{MeV}^{-1} \times \Delta E \quad , \tag{5.18}$$

$$f' = 5.4 \times 10^{-3}\ \mathrm{mm/MeV} \quad , \tag{5.19}$$

where $12\ \mathrm{mm}$ is the anode wire interval.

To implement the gain reduction into the simulation, the saturation factor s is calculated based on Eq. (5.16) for each area enclosed by the anode and cathode wires. Figure 5.12 shows an enclosed area, and it has $12\ \mathrm{mm} \times 6\ \mathrm{mm}$ area in the MWPC region. The number of collected electrons is reduced by a factor of s for each area. If there is an ionization process as shown in Figure 5.13, the calculated distribution of the saturation factor is present in Figure 5.14. We can see that $s \sim 0.5$ at several areas, which means the multiplication factor declines to approximately half of the original at the areas.

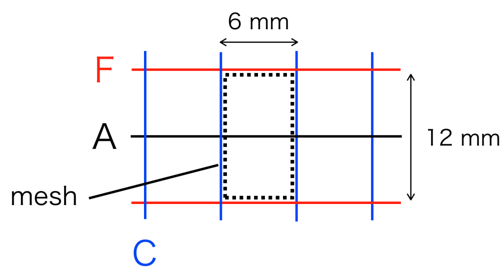

Figure 5.12: Defined rectangles to calculate the saturation factor.

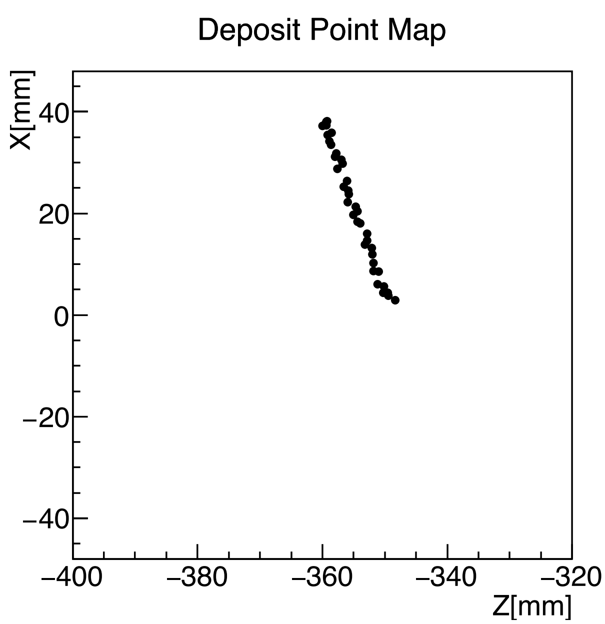

Figure 5.13: Two-dimensional distribution of ionization point in the simulation.

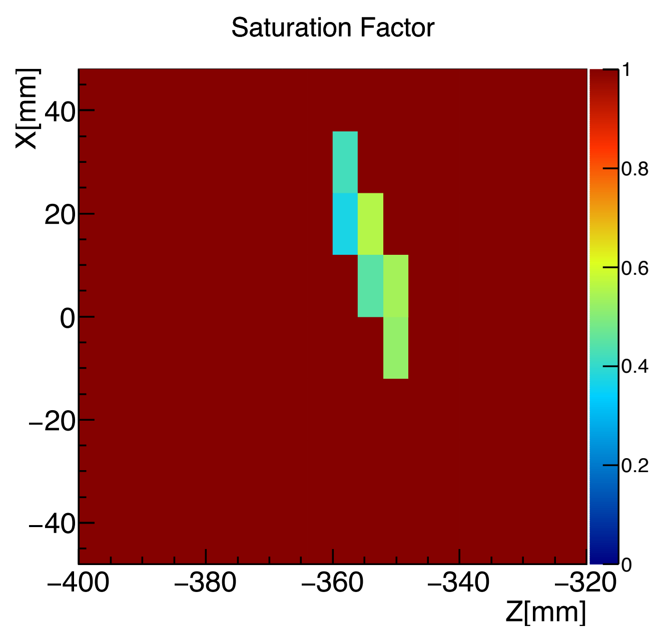

Figure 5.14: Distribution of saturation values based on the ionization point (Figure 5.13).

Figure 5.15 compares the FPH_MAX distribution between the experimental data and the simulation. The space charge effect has not been implemented into the simulation in the left graph. The simulation of the right distribution considers the gain reduction due to the space charge effect. The space charge effect has a direct influence especially for the $^3\mathrm{He}(n,\ p)^3\mathrm{H}$ distribution, and we can see the implementation reproduces the experimental distribution better than before.

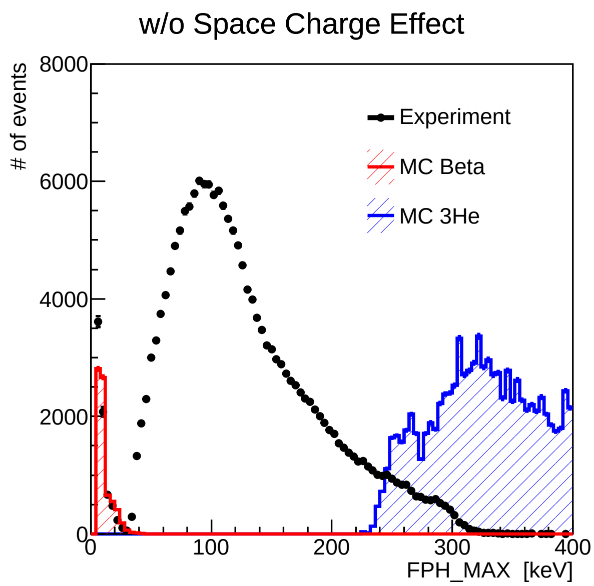

Figure 5.15: Comparison in FPH_MAX distribution. The left graph shows the simulated distribution without the space charge effect, whereas the right graph shows the simulated distribution considering the space charge effect.

5.2.4 Adjustment for parameters of space charge simulation

The gain reduction due to the space charge effect is implemented as described above section. However, there is still a significant difference in the $^3\mathrm{He}(n,\ p)^3\mathrm{H}$ distribution as shown in the right distribution of Figure 5.15. Since the distribution of the beta-decay events are well reproduced, the discrepancy in the $^3\mathrm{He}(n,\ p)^3\mathrm{H}$ distribution is expected to come from the uncertainty of space charge parameter. The modeling of the space charge effect in Eq. (5.16) is substantially a function of one variable ($f`\frac{d(\Delta E)}{dl}G_0$). Thus the space charge parameter f' is the only adjustable parameter in the modeling. The optimum value is determined to minimize χ^2 value from $36\ \mathrm{keV}$ to $300\ \mathrm{keV}$ region. The χ^2 parameter is defined as

$$\chi^2 = \sum_{E=36\ \mathrm{keV}}^{300\ \mathrm{keV}} \frac{[N_{EX}(E) - N_{MC}(E)]^2}{\sigma_{EX}(E)^2 + \sigma_{MC}(E)^2}\ , \tag{5.20}$$

where $N_{EX}(E)$ and $N_{MC}(E)$ are the numbers of events whose FPH_MAX values are E in the experimental and simulated distribution, respectively. $\sigma(E)$ represents the standard deviation of the number of events.

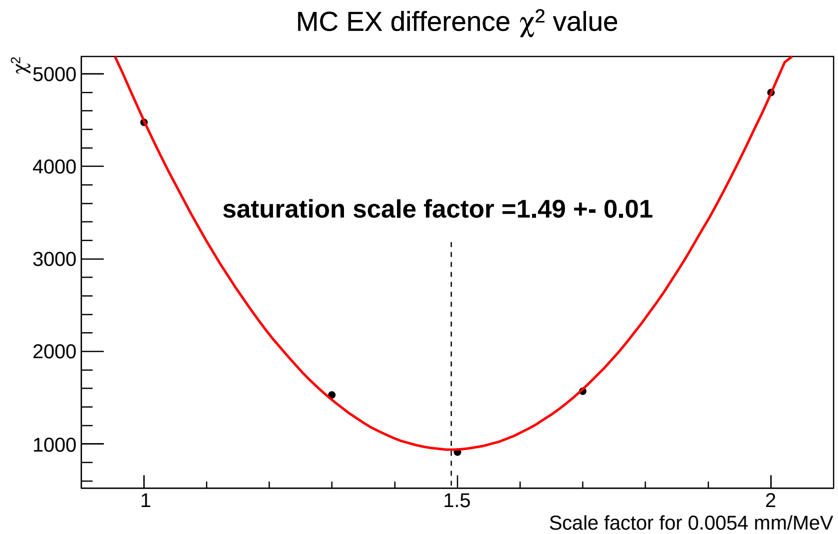

Figure 5.16: χ^2 value for several scaling parameter for f' in Eq. (5.16).

Figure 5.16 shows the χ^2 value as a function of the scale factor for $f' = 0.0054\ \mathrm{mm/MeV}$. The optimum factor was decided as 1.49 (corresponding to $f' = 0.0080\ \mathrm{mm/MeV}$). Figure 5.17 compares the FPH_MAX distribution before adjustment (left) and after adjustment (right). The low-energy threshold of the $^3\mathrm{He}(n,\ p)^3\mathrm{H}$ distribution changes from $33\ \mathrm{keV}$ to $25\ \mathrm{keV}$ due to the adjustment. This means that the low-energy threshold has an uncertainty of $8\ \mathrm{keV}$ because of the incomplete implementation of the space charge effect. The separation position is determined as $25\ \mathrm{keV}$ so as not to be affected by this uncertainty.

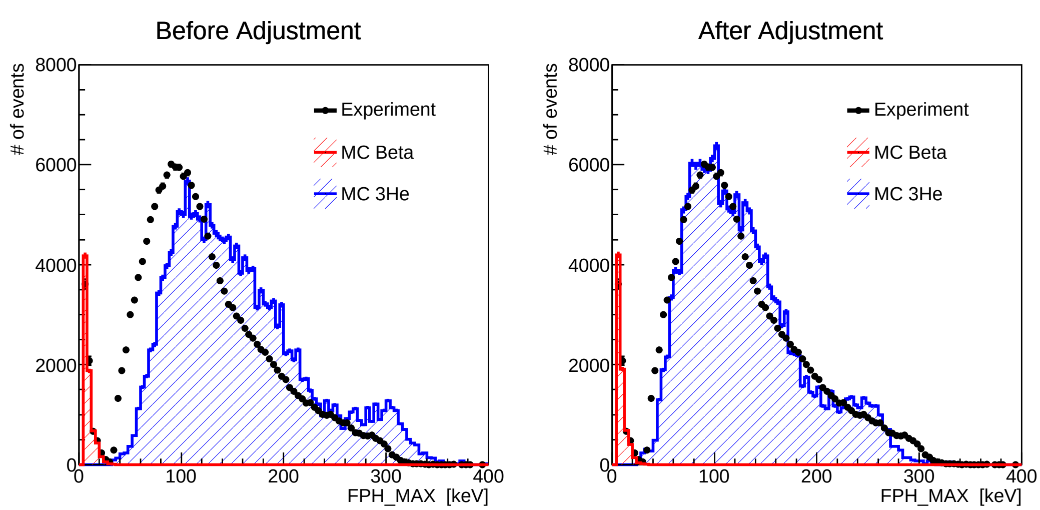

Figure 5.17: FPH_MAX distribution for experiment (black) and simulation (blue and red).

5.2.5 Conclusion

The separation of the beta-decay and the $^3\mathrm{He}(n,\ p)^3\mathrm{H}$ events is carried out in the FPH_MAX distribution. The amount of correction and uncertainties relevant to the separation are evaluated using the Monte Carlo simulation as listed in Table 5.5. The final uncertainties derive from the differences due to the adjustment.

1) Signal loss ratio of beta-decay

Several beta-decay events have higher FPH_MAX values than the cut position of $25\ \mathrm{keV}$. The number of these events correspond to the loss of beta-decay due to the separation. The loss ratio is estimated using the simulation distribution as

$$\text{signal loss ratio} = \frac{\text{the number of events of FPH\_MAX} > 25\ \text{keV}}{\text{the total number of events}}\ , \tag{5.21}$$

$$= \frac{84}{9553}\ , \tag{5.22}$$

$$= 0.0088 \pm 0.0010\ . \tag{5.23}$$

2) leakage to $^3\mathrm{He}(n,\ p)^3\mathrm{H}$

The number of the beta-decay events whose FPH_MAX values higher than $25\ \mathrm{keV}$ results in the overestimation of the $^3\mathrm{He}(n,\ p)^3\mathrm{H}$ events. The correction amount to the total number of $^3\mathrm{He}(n,\ p)^3\mathrm{H}$ events due to these events can be evaluated as

$$\text{leakage} = 0.0088 \times \frac{N_\beta}{N_{^3\mathrm{He}}}\ , \tag{5.24}$$

$$= 0.0088 \times \frac{1}{\tau_n \sigma v \rho}\ , \tag{5.25}$$

$$= 0.0088 \times \frac{1}{880\ \mathrm{s} \times 5333\ \mathrm{barn} \times 2200\ \mathrm{m/s}} \times \frac{8.3 \times 300\ \mathrm{m}^3}{0.1 \times 6.0 \times 10^{23}}\ , \tag{5.26}$$

$$= 0.0088 \times \frac{1}{24}\ , \tag{5.27}$$

$$= (3.6 \pm 0.4) \times 10^4\ . \tag{5.28}$$

3) Signal loss ratio of $^3\mathrm{He}(n,\ p)^3\mathrm{H}$

Since the cut position of $25\ \mathrm{keV}$ is determined so that no $^3\mathrm{He}(n,\ p)^3\mathrm{H}$ events exist below the cut position. The upper limit of the signal loss ratio is calculated based on the total number of events (15884) as

$$\text{signal loss (90\%C.L.)} < -\frac{\log(1-0.90)}{15884}\ , \tag{5.29}$$

$$= 1.4 \times 10^{-4}\ . \tag{5.30}$$

4) leakage to beta-decay

The correction amount to the total number of beta-decay events can be evaluated with the same way as $^3\mathrm{He}(n,\ p)^3\mathrm{H}$

$$\text{leakage (90\%C.L.)} \leq 1.4 \times 10^{-4} \times \frac{N_{^3\mathrm{He}}}{N_\beta} , \quad (5.31)$$

$$= 3.4 \times 10^{-3} . \quad (5.32)$$

Table 5.5: Efficiency of beta-decay and $^3\mathrm{He}(n,\ p)^3\mathrm{H}$ with respect to the energy cut of FPH_MAX=25 keV. The uncertainties originate from the statistical uncertainties derived from the simulation. The values of the upper limit correspond to 90% confidence levels.

	beta-decay		$^3\mathrm{He}(n,\ p)^3\mathrm{H}$	
	1) signal loss	2) leakage to $^3\mathrm{He}(n,\ p)^3\mathrm{H}$	3) signal loss	4) leakage to beta-decay
before adjustment	$(1.1 \pm 0.1)\%$	$(0.046 \pm 0.004)\%$	$\leq 0.014\%$	$\leq 0.34\%$
after adjjustment	$(0.88 \pm 0.10)\%$	$(0.036 \pm 0.004)\%$	$\leq 0.014\%$	$\leq 0.34\%$
result	$(0.88 \pm 0.22)\%$	$(0.036 \pm 0.010)\%$	$\leq 0.014\%$	$\leq 0.34\%$

Chapter 6

Summary and Discussion

The neutron lifetime (τ_n) is an essential parameter in the weak interaction. It affects the predicted abundance of light elements in the early universe. Moreover, τ_n is used for deriving the $V_{\rm ud}$ element in the CKM matrix. There are mainly two kinds of methods to determine the world average of the τ_n value. One is a proton counting method, and the other is a neutron counting method. However, there exists a significant discrepancy between the two measured results of τ_n. The discrepancy directly fluctuates the predicted abundance in the early universe, and hinders an unitarity test of the CKM matrix.

To resolve the problem of this discrepancy, we conduct an experiment to measure τ_n using a completely new method. Our ultimate purpose is to measure τ_n to $1\ \mathrm{s}$ precision and resolve the current ambiguity pertaining τ_n. The experiment uses pulsed neutron beams at Material and Life-science Facilitiys(MLF) at Japan Proton Accelerator Research Complex (J-PARC). We developed a Time Projection Chamber and a Spin Flip Chopper for this experiment. There is a small amount of ${}^3\mathrm{He}$ gas in the TPC, which captures a neutron and causes ${}^3\mathrm{He}(n,\ p){}^3\mathrm{H}$. The neutron lifetime can be derived by counting the numbers of the beta-decay and ${}^3\mathrm{He}(n,\ p){}^3\mathrm{H}$ events in the TPC.

This thesis focuses on the estimation of systematic uncertainties for the first set of data acquired in 2014. In this thesis, we proved the existence of ${}^{17}\mathrm{O}(n,\ \alpha){}^{14}\mathrm{C}$ background in the TPC. This requires the $-0.50 \pm 0.03\%$ correction of τ_n. In addition, the waveforms of anode wires and field wires can be created in the simulation with the quantitative understanding of the induced current. This enabled the usage of the field wires in order to separate the beta-decay and ${}^3\mathrm{He}(n,\ p){}^3\mathrm{H}$ events, which has a better separation capability than the anode wires. As a result, the correction amount and its uncertainty are reduced to within 1% on τ_n.

Table 6.1 lists the currently estimated uncertainties and correction amounts. We expect our first result to have an uncertainty of O(1)%. In order to improve the measurement precision, following two items must be considered.

- ${}^3\mathrm{He}$ density measurement
  The ${}^3\mathrm{He}$ density in the TPC directly affects τ_n as shown in Eq. (1.29). However, its measurement uncertainty is 5% at present. The measurement precision is limited by the uncertainty of the ${}^3\mathrm{He}$ abundance ratio of the calibration gas. This calls for a method for measuring the ${}^3\mathrm{He}$ abundance ratio of the calibration gas precisely. For example, the ratio of ${}^3\mathrm{He}$ and ${}^4\mathrm{He}$ can be derived within 0.5% precision in principle using the gas system at the beamline. This

method measures the gas pressure in high-pressure condition in advance, and extrapolates the pressure assuming the Boyle-Charle's law. The validity of the procedure is currently under consideration. On the other hand, the idea to use ^{14}N instead of $^{3}\mathrm{He}$ is also taken into consideration. Since a ^{14}N nucleus has a comparatively small absorption probability for a neutron, the large abundance ratio of ^{14}N is allowed in the TPC, which is expected to resolve the problem relating to the density measurement.

- Statistics
  We acquired the first data yielding a statistical uncertainty of 2% on τ_n during the few days of measurement. Although the beam intensity at J-PARC will increase from current $500\ \mathrm{kW}$ to $1\ \mathrm{MW}$ within a few years, it is estimated that about 1200 hours are required to achieve our goal (0.1% statistical uncertainty on τ_n). This comes from the problem that the total neutron flux is currently limited by the apertures of the TPC and the SFC. Therefore, the development of the TPC and the SFC with large apertures is needed to increase the neutron flux at the detector. It is estimated that the measurement period to achieve 0.1% statistical uncertainty will decrease to about 40 days after the development.

Table 6.1: Current amount of correction and uncertainties for τ_n.

parameter		uncertainty [%]	correction [%]
N_β	statistics	1.9	—
	^{3}He leakage	<0.34 (90%C.L.)	0
	$B^{\mathrm{int}\gamma}$ and B^{scat}	being evaluated	being evaluated
	efficiency	0.25 (preliminary)	-5.2 (preliminary)
	pileup	<0.3	0
$N_{^3\mathrm{He}}$	B^{nitro}	0.23	-1.45
	B^{oxy}	0.03	-0.50
	B^{scat}	0.03	-0.28
N_β and $N_{^3\mathrm{He}}$	SFC contrast	<0.5	<0.5
	γ ray absorption in LiF plate	0.28 (preliminary)	-0.43 (preliminary)
ρ	pressure	5 (preliminary)	—
	chamber expansion (temperature)	<1	<1
	chamber deformation (pressure)	0.3	0.3
	temperature distribution	O(0.1)	O(0.1)
σ	$^3\mathrm{He}(n,\ p)^3\mathrm{H}$ cross section	0.13	—

We will acquire more data with the increase of the MLF operation power this year. In addition, improvement mainly for the above two items is conducted at the same time. We are going to improve the precision of τ_n to 0.1% in the future, which is expected to resolve the current discrepancy of τ_n.

Appendix A

Mass Spectrometer

The ^{3}He pressure in the TPC can be derived using the Boyle-Charle's law as mentioned in Section 2.2.9. On the other hand, we also directly measure the ^{3}He to ^{4}He ratio for enclosed gas in the TPC to cross-check the result. A Mass Spectrometer (modified-VG5400), developed by H. Sumino [31], is used to measure the isotope ratio of the noble gases. Figure A.1 shows a photo of the spectrometer. There are two detectors for the ^{3}He and ^{4}He measurement, so the ratio can be measured simultaneously at a constant magnetic field. However, only its relative ratio can be measured in the spectrometer. Therefore, we use HESJ (HElium Standard of Japan) gas for the standard of helium isotope measurement. Its ^{3}He to ^{4}He ratio is well studied [32], and we can derive the absolute ^{3}He to ^{4}He ratio using the result for HESJ gas.

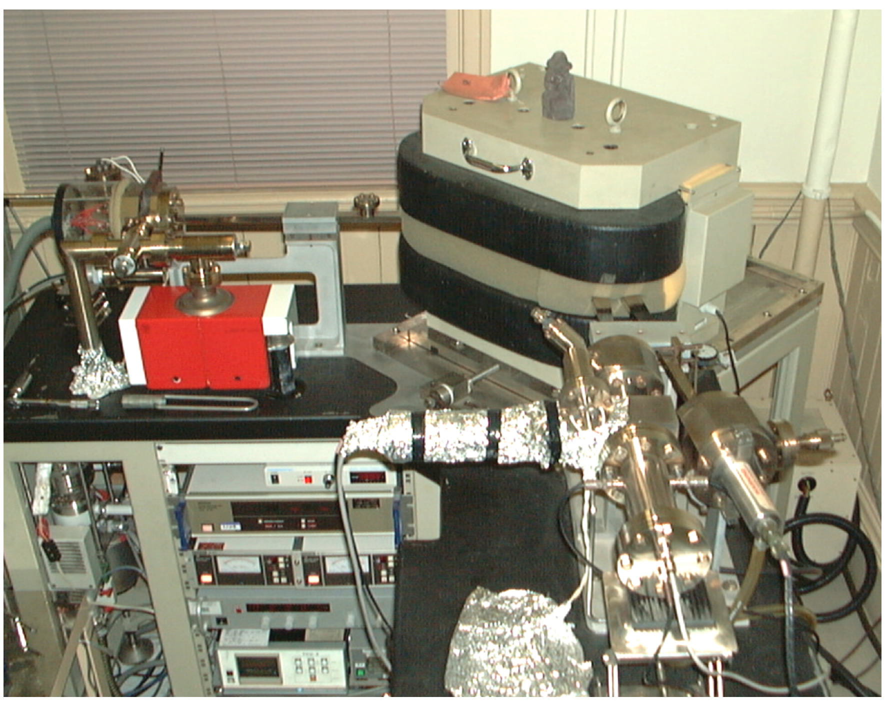

Figure A.1: Photo of the mass spectrometer [31].

Acknowledgments

First of all, I would like to express my greatest appreciation to my supervising advisor Prof. Satoru Yamashita. He gave me the precious opportunity to take part in such an interesting experiment at J-PARC. I always received the accurate and essential advice from him when I was at a standstill in my research. In addition, he actively gave me many chances to participate in various kinds of research societies, which greatly heightened my interest in physics. It was a wonderful and fruitful experience for me to be able to do the research as his student during my master course.

I am grateful to the members of the experiment in this thesis and Neutron Optics and Physics (NOP) group. They gave me lots of beneficial advice for my analysis, measurements, and presentations, which supported and encouraged me so much. In particular, Dr. Kenji Mishima devoted a considerable amount of his time to guide me in my research. His extensive knowledge and experience always taught me the fun to seek truths in physics and science. I will always keep the lessons from him in my mind when I continue my research in the future.

I also would like to thank all the members of Yamashita laboratory. Their earnest and energetic altitudes toward research are good stimuli for me, and they all gave me gread advice for my research. I especially had the immense support from both Mr. Takahito Yamada and Ms. Sei Ieki, who are collaborators of the neutron experiment. They patiently taught me everything about experiment in detail, although I had little knowledge at first. I could not have made progress in my research without their kind and continuous support.

I also enjoy my student life with all the ICEPP students. In particular, I had so much fun having conducted experiments with Mr. Kento Kasuya since we were undergraduate students.

I am also specially grateful to Dr. Jacqueline Yan for her considerable support to finish my thesis. She dedicated her invaluable holidays to proofread all the sentences in this thesis. She also provided useful advice and counsel to my presentations many times.

Finally, the deepest appreciation goes to my parents, Masaaki and Reiko, for supporting me all my life.

Bibliography

[1] K.A. Olive et al. (Particle Data Group). Review of particle physics. *Chin. Phys. C*, Vol. 38, No. 9, p. 80, 2014.

[2] J. Dunkley, E. Komatsu, M. R. Nolta, D. N. Spergel, D. Larson, G. Hinshaw, L. Page, C. L. Bennett, B. Gold, N. Jarosik, J. L. Weiland, M. Halpern, R. S. Hill, A. Kogut, M. Limon, S. S. Meyer, G. S. Tucker, E. Wollack, and E. L. Wright. Five-year wilkinson microwave anisotropy probe observations: Likelihoods and parameters from the wmap data. *The Astrophysical Journal Supplement Series*, Vol. 180, No. 2, p. 306, 2009.

[3] M. Pospelov and J. Pradler. Big bang nucleosynthesis as a probe of new physics. *Ann. Rev. Nucl. Part. Sci.*, Vol. 60, pp. 539–568, 2010.

[4] J.C. Hardy and I.S. Towner. The current evaluation of vud. In *12th Conference on the Intersections of Particle and Nuclear Physics (CIPANP 2015) Vail, Colorado, USA,*, 2015.

[5] J. C. Hardy and I. S. Towner. Superallowed $0^+ \to 0^+$ nuclear β decays: 2014 critical survey, with precise results for V_{ud} and ckm unitarity. *Phys. Rev. C*, Vol. 91, p. 025501, Feb 2015.

[6] J. S. Nico, M. S. Dewey, D. M. Gilliam, F. E. Wietfeldt, W. M. Snow X. Fei, G. L. Greene, J. Pauwels, R. Eykens, A. Lamberty, J. Van Gestel, and R. D. Scott. Measurement of the neutron lifetime by counting trapped protons in a cold neutron beam. *Phys. Rev. C*, Vol. 71, p. 055502, 2005.

[7] A.T. Yue, M.S. Dewey, Gilliam, G.L. Greene, A.B. Laptev, J.S. Nico, W.M. Snow, and F.E. Wietfeldt. Improved determination of the neutron lifetime. *Phys.Rev.Lett.*, Vol. 111, p. 222501, 2013.

[8] A. Serebrov, V. Varlamov, A. Kharitonov, A. Fomin, Yu. Pokotilovski, P. Geltenbort, J. Butterworth, I. Krasnoschekova, M. Lasakov, R. Tal'daev, A. Vassiljev, and O. Zherebtsov. Measurement of the neutron lifetime using a gravitational trap and a low-temperature fomblin coating. *Phys.Lett.*, Vol. B605, pp. 72–78, 2005.

[9] R. Kossakowski, P. Grivot, P. Liaud, K. Schreckenbach, and G. Azuelos. Neutron lifetime measurement with a helium-filled time projection chamber. *Nuclear Physics A*, Vol. 503, No. 2, pp. 473 – 500, 1989.

[10] H. Otono. *New detector system for the precise neutron lifetime measurement using pulsed cold neutron beams*. PhD thesis, The Univ. of Tokyo, December 2011.

[11] C. D. Keith, Z. Chowdhuri, D. R. Rich, W. M. Snow, J. D. Bowman, S. L. Penttilä, D. A. Smith, M. B. Leuschner, V. R. Pomeroy, G. L. Jones, and E. I. Sharapov. Neutron cross sections for 3he at epithermal energies. *PHYSICAL REVIEW C*, Vol. 69, p. 034005, 2004.

[12] Neutron scattering lengths and cross sections. `http://www.ncnr.nist.gov/resources/n-lengths/` seen at Dec. 5, 2015.

[13] J-parc official website.

[14] K. Mishima. J-parc 中性子基礎物理ビームライン（bl05/nop）. *Neutron network news (Hamon)*, Vol. 25, No. 2, pp. 156–160, 2015.

[15] T. Ebisawa, T. Kawai, S. Tasaki, M. Hino, and D. Yamazaki. 中性子スピン光学. Kyushu Univ. Press, 2003.

[16] H. Otono, Y. Arimoto, N. Higashi, Y. Igarashi, Y. Iwashita, T. Ino, R. Katayama, R. Kitahara, M. Kitaguchi, H Matsumura, K. Mishima, H. Oide, N. Nagakura, R. Sakakibara, T. Shima, H. Shimizu, T. Sugino, N. Sumi, H. Sumino, K. Taketani, G. Tanaka, M. Tanaka, K. Tauchi, T. Tomita, A. Toyoda, T. Yamada, S. Yamashita, H. Yokoyama, and T. Yoshioka. Development of time projection chamber for precise neutron lifetime measurement using pulsed cold neutron beams. *Nuclear Instruments and Methods in Physics Research Section A: Accelerators, Spectrometers, Detectors and Associated Equipment*, Vol. 799, pp. 187–195, 2015.

[17] Xcom: Photon cross sections database.

[18] T. Ino, H. Otono, K. Mishima, and T. Yamada. Precision neutron flux measurement with a neutron beam monitor. *Journal of Physics: Conference Series*, Vol. 528, No. 1, p. 012039, 2014.

[19] Y. Igarashi, H. Fujii, T. Higuchi, M. Ikeno, E. Inoue, T. Murakami, Y. Nagasaka, M. Nakao, K. Nakayoshi, M. Saitoh, S. Shimazaki, Soh Y. Suzuki, M. Tanaka, K. Tauchi, T. Uchida, and Y. Yasu. A common data acquisition system for high-intensity beam experiments. *Nuclear Science, IEEE Transactions*, Vol. 52, No. 6, 2 2005.

[20] Richard B. Firestone and Virginia S. Shirley. *Table of Isotopes*. Wiley-Interscience, 1.0 edition, March 1996.

[21] R. Sakakibara. 中性子寿命測定実験の入射フラックス測定の安定性とその系統誤差の評価. Master's thesis, Nagoya Univ., 1 2015.

[22] G. Tanaka. J-parc における中性子寿命精密測定実験 -2014 年度取得データの解析-. Master's thesis, Kyushu Univ., 2015.

[23] Geant4 simulation official website. https://geant4.web.cern.ch/geant4/.

[24] N. Z. Alcock and D. G. Hurst. Neutron diffraction by gases. *Phys. Rev.*, Vol. 75, pp. 1609–1610, May 1949.

[25] Ansys official website. https://www.ansys.jp/index.html.

[26] Garfield official website. http://garfield.web.cern.ch/garfield.

[27] W. Shockley. Currents to conductors induced by a moving point charge. *Journal of Applied Physics*, Vol. 9, p. 635, 1938.

[28] A. Ishikawa. Gas properties for tpc. http://www-hep.phys.saga-u.ac.jp/ILC-TPC/gas/.

[29] M. Berglund and Michael E. Wieser. Isotopic compositions of the elements 2009. Technical report, IUPAC, 2011.

[30] H. Oide, H. Otono, and S. Yamashita. ワイヤーチェンバーを用いた電離損失エネルギー測定における空間電荷効果の取り扱いについて. In *The Autumn Meeting of the Physical Society of Japan*, 2011.

[31] H. Sumino, K. Nagao, and K. Notsuji. Highly sensitive and precise measurement of helium isotopes using a mass spectrometer with double collector system. *Journal of the Mass Spectrometry Society of Japan*, Vol. 49, No. 2, pp. 61–68, 2001.

[32] H. Sumino. History and current status of noble gas mass spectrometry to develop new ideas based on study of the past. *Journal of the Mass Spectrometry Society of Japan*, Vol. 63, No. 1, pp. 1–30, 2015.